Australian National University

Silicon Ingot Characterization using Photoconductance Lifetime Techniques

Mohsen Goodarzi

March 2019

A thesis submitted for the degree of

Doctor of Philosophy at

The Australian National University

Declaration

I certify that this thesis does not incorporate without acknowledgement any material previously submitted for a degree or diploma in any university, and that, to the best of my knowledge, it does not contain any material previously published or written by another person except where due reference is made in the text. The work in this thesis is my own, except for the contributions made by others as described in the Acknowledgements.

Mohsen Goodarzi
March 2019

To my parents, *Zahra* and *Karam*,

for their unconditional love and support.

Acknowledgments

First and foremost, I would like to express my deepest gratitude to Prof Daniel Macdonald, my primary supervisor, for his continuous support and guidance, as well as always making himself available despite his countless other commitments. I cannot imagine finishing this work without his encouragement, passion, and insight. As his mentee, there have been countless invaluable experiences in the last four years which will remain with me for the rest of my professional and personal life. I would also like to thank my co-supervisor Dr Ronald Sinton for sharing his wisdom and his unique knowledge from more than three decades in the PV industry. He too has always made himself available even during some of his busiest periods, including taking the time to talk face to face at different international conferences. In addition to his outstanding support during my PhD research, his exceptional and impressive scientific approach as a leader in the silicon characterisation industry has been an inspiration for me.

I would also like to thank Prof Andres Cuevas, and Dr Fiacre Rougieux (now at UNSW) for their incredible support, as members of my supervisory panel, particularly during the development of the simulation tool and PECVD training, respectively. I am also grateful to our collaborators from UNSW/BTimaging including Prof Thorsten Trupke, Dr Bernhard Mitchell (now at WAVELABS Solar Metrology System) and Daniel Chung for sharing their knowledge about characterisation with PL imaging techniques as well as their supportive collaboration.

I should also express my gratitude to my colleagues in Dan's research group for creating such a pleasant and productive work environment for PhD students. I want to thank Dr Pheng Phang for his continuous assistance and support during my PhD particularly in the lab for the sample preparation and surface passivation (chapter 4). I would like to thank Dr Hieu Nguyen for the great discussions about crystal defects and impurities, and Dr AnYao Liu for constructive conversations

about iron gettering during the surface passivation as well as calculating [Fe_i] after SiN deposition (chapter 4). I need to also express my gratitude to Dr Hang Sio for sharing his experience in developing simulation tools as well as recombination in grain boundaries, and, to my other group members, Dr Peiting Zheng, Ms Jessica Wu and Mr Rabin Basnet, for their contributions during my PhD. I also thank Dr Azul Mayon and Ingrid Haedrich for their help to measure the transmission spectrum and the surface reflection used in chapter 5 and chapter 6.

I wish to express my gratitude to our great people in the solar PV lab for their incredible work in training, equipment maintenance and maintaining safety in the lab. I am very grateful to Chris Samundsett for his time in conducting process training with me. I would like to thank Nina de Caritat, and Maureen Brauers for keeping the lab running safely, and for the lab training. I am also deeply appreciative of the great efforts in technical support from James Cotsell, Mark Saunders and Bruce Condon.

I would also like to express my gratitude to my master's degree supervisor, Associate Prof Brian Usher from whom I learned critical thinking and who encouraged me to pursue a career in research and academia.

I want to thank Mohammad and Molood (my brother and sister) for their endless support and help as well as their efforts in taking up many of my family duties in my absence.

Finally, I thank the management staff, particularly Prof Peter Kanowski, the master of house, and my fellow residents at Graduate House for creating such a wonderful living environment for me during my PhD.

Abstract

The main objective of this thesis is to evaluate the accuracy of minority carrier lifetime measurements in crystalline silicon ingots and blocks. Photoconductance lifetime measurement as a non-destructive contactless method has several advantages which make the method a well-established characterisation technique for silicon wafers. It is a fast and simple method to use for a broad range of carrier lifetimes as well as a broad range of injection levels. Despite the advantages of early-stage material characterizations, the application of photoconductance lifetime measurement methods to silicon ingots and blocks is not yet as widespread.

Immediate feedback about specific impurities and crystal defects in the ingots and blocks can result in the optimization of the crystal growth process. It also helps to make more reliable decisions for cropping ingots and blocks prior to wafering. In the PV industry, in particular, it may also be possible to sort the wafers at the start of processing and tune the cell process for different quality wafers coming from the different sections of the block. This detailed information can potentially be used during the manufacturing processes to achieve higher efficiency as well as higher yield.

The first phase of the project is devoted to modelling and simulation of photoconductance lifetime measurements in both quasi-steady state and transient modes on semi-infinite thick (the sample thickness is significantly longer than the carrier diffusion length) crystalline silicon samples. Such a model is required to study the impact of different parameters such as doping concentration, various impurities as well as high surface recombination velocity (SRV) of an as-cut crystalline silicon ingot or block on lifetime measurements. The simulation tool accepts several input parameters such as different concentrations of various acceptor/donor doping as well as material impurities to simulate lifetime measurements at different injection levels.

Then the simulation tool is used to evaluate the accuracy of interstitial iron concentration measurements in boron-doped silicon blocks and ingots. The simulation results demonstrated that the error in the extracted interstitial iron concentration is generally less than 20% for typical iron contamination densities in the central regions of multicrystalline ingots ($[Fe_i] < 10^{11}$ cm^{-3}). The measurements on a p-type multicrystalline silicon block showed that the quasi-steady state photoconductance measurements of dissolved iron concentrations at the ingot level are subject to only a small error and, after correction, the results were in good agreement with $[Fe_i]$ measurements on wafers from an adjacent block as a comparison benchmark. Similar results were obtained when dissolved iron was measured on a block and again on the wafers of the same block after wafering. The dissolved iron concentration measured by the quasi-steady state photoconductance (QSSPC) on the blocks were in good agreement with the results from the photoluminescence intensity ratio imaging technique.

It is shown that reducing the impact of high surface recombination velocity is the key to increase reported transient lifetime towards the actual bulk lifetime. The simulations showed how the impact of high SRV is reduced as time elapses after the light source was terminated in the absence of photogeneration in the sample. The simulation results demonstrated that higher light source intensities to generate higher initial injection levels improves the measurement results, performed at a given injection level, which was confirmed by the experimental results.

The simulation results also proposed an improvement in transient lifetime measurements with deeper photogeneration via filters with longer cut-off wavelengths due to the lower carrier diffusion to the surface. The measurement results confirmed approximately 10% increase after replacing the standard RG1000 filter with a gradual cut-off wavelength at 1000 nm in comparison with the EO1100 filter with the sharp cut-off at 1100 nm.

The deeper photo-generation profiles of the filters with longer cut-off wavelengths reduced the impact of surface recombination in the QSSPC method as well. Such a reduction leads to less reliance on the transfer function to estimate the bulk lifetimes in comparison with the standard filter. However, there is a corresponding increase in the uncertainty of determination of the cumulative photogeneration due to the reference cell EQE in the longer-range wavelengths. Moreover, there is a significant dependency on selecting the proper value for optical constant due to carrier generation beyond the coil sensitivity depth. Such consequences counteract the benefits of reduced surface recombination impact and make the EO1100 filter an unsuitable option for QSS measurements.

The comparison between the results from the QSSPC method and transient photoconductance decay method, revealed a reasonable agreement between the results using the EO1050 filter, reducing the discrepancy to around 15%. The use of the EO1050 filter is a suitable choice to reduce the uncertainty of the estimated bulk lifetime in the QSS mode, due to a decreased reliance on the transfer function, while still allowing sufficiently accurate estimation of the optical constant.

Table of Contents

Chapter 1: Introduction

The Photovoltaics (PV) industry has experienced dramatic global growth due to the ~70% installation cost reduction from 2010 to 2017 [1]. By 2017, the cumulative installed capacity of PV modules grew from 139 to 415 GW over a period of four years, with the global installation of 95 GW capacity in 2017 alone [2, 3]. With about 37% of total added power generating capacity in 2017, solar alone saw more new capacity deployed than fossil fuels and nuclear energy combined; adding nearly twice as much capacity as its renewables peer, wind power [4, 5].

Being the second most abundant element in the Earth crust after oxygen, silicon is a reliable non-toxic source for further growth in the PV industry. Furthermore, many studies have been performed on the material properties of silicon as the microelectronic industry is also based on crystalline silicon. However, high-quality microelectronic grade silicon is too expensive to produce PV solar cells if it is to be a competitive option in the electricity market. Crystalline silicon wafer-based solar cells accounted for around 95% of PV production market share in 2017 with 61% production from multicrystalline silicon and the rest from monocrystalline [2].

1.1 Motivation

The absorption of photons with energies higher than the silicon band gap ($E_{ph} > 1.14$ eV) within the silicon material generates electron-hole pairs. These pairs last, on average, a finite time called the carrier lifetime. During the continuous electron-hole pair generation, as in a solar cell, the value of the lifetime determines the stable population of electrons and holes. This population determines the voltage produced by the solar cell which should desirably be as high as possible [6]. Another equally important material property related to the lifetime is the diffusion length which is defined as the average distance that carriers can travel before they recombine. The diffusion length should,

ideally, be longer than the wafer thickness or the longest generation depth to ensure the carriers can reach and be collected by contacts to generate a high short-circuit current. Hence, the carrier lifetime characterisation is of the greatest importance because of its direct impact on both the voltage and the current of the solar cell [6]. The minority-carrier lifetime data of silicon wafers are valuable for monitoring process steps as well as high-efficiency solar cell fabrication control and optimization [7].

The lifetime of a sample is not a constant single value over the entire processes from the silicon crystal growth to the fabrication of the final cell. In contrast, the lifetime can be significantly altered during the fabrication process due to possible contamination, thermal degradation, illumination or annealing at certain temperatures. Measurement conditions such as injection level and temperature can also impact the lifetime of a sample.

The main objective of this thesis is to evaluate the accuracy of minority carrier lifetime measurements in crystalline silicon ingots and blocks. Quasi-steady state photoconductance (QSSPC) lifetime measurements was introduced by Sinton and Cuevas [7] as a non-destructive contactless method for minority carrier lifetime characterization in semiconductor materials. Along with transient photoconductance decay (PCD), the QSSPC has been extensively employed in silicon PV research and industry for over two decades to characterise the minority carrier lifetime of crystalline silicon at the wafer level. Photoconductance lifetime measurement has several advantages which makes the method a well-established characterisation technique for silicon wafers [8]. The method can be potentially used for a broad range of minority carrier lifetimes from a few microseconds to tens of milliseconds as well as a broad range of injection levels. It is also fast and simple to use in both research labs and the industrial environment.

Despite these advantages as well as the attractive benefits of early-stage material characterizations, the application of photoconductance lifetime measurement methods to silicon ingots and blocks is not yet as widespread [9]. This application can provide more immediate feedback on crystal growth quality through knowledge about specific impurities and crystal defects in the ingots and blocks. Consequently, more reliable decisions can be made for cropping ingots and blocks for wafering purposes [10]. It may also be possible to sort the wafers at the start of processing and tune the cell process for different quality wafers coming from the different sections of the block [11]. This detailed information can potentially be used during the manufacturing processes to achieve higher efficiency as well as higher yield.

Recently, some studies of characterization at the ingot level have been performed and gained interest from both crystal growers and solar cell manufacturers [12-14]. However, a comprehensive study of photoconductance lifetime characterization has not been performed yet to evaluate the performances and the accuracy of the method at ingot levels.

This study is devoted to modelling and simulation of photoconductance lifetime measurements in both quasi-steady state and transient modes on semi-infinite thick crystalline silicon samples. The term semi-infinite is used for samples in which the sample thickness is significantly longer than the carrier diffusion length or generation depth. Such a model is required to investigate the impact of different parameters such as doping concentration and various impurities on the measured lifetime on a crystalline silicon ingot or block.

In addition to the mentioned factors which exist at both the wafer and the ingot level, the as-cut surface of ingots or blocks introduces a high surface recombination velocity (SRV). Such a surface introduces a large deviation between the measured carrier lifetime and the actual carrier lifetime in the bulk (which is related to the final cell efficiency) due to the domination of recombination in

the surface. Hence, it is important to carefully investigate the impact of the high SRV and, consequently, reduce the deviation between the measured lifetime and actual bulk lifetime[15].

Characterisation of doping concentrations and impurities provides immediate feedback on crystal growth results allowing the growth process to be optimized for the best results. More importantly for the PV industry, along with the presence of crystal structural defects in multicrystalline silicon, metal impurities are the main efficiency-limiting defects in c-Si solar cells [3, 16, 17]. As an example, iron (Fe), due to its high solubility and fast diffusivity, is one of the most common and detrimental impurities in p-type silicon particularly in multicrystalline wafers [16, 18, 19].

A relatively large concentration of iron can be introduced into silicon, in the forms of both interstitial and precipitated atoms, during the crystal growth, and also by high-temperature cell fabrication steps in the absence of stringent contamination control [3]. Because of the more harmful impact of the dissolved form [3, 20], an accurate determination of interstitial iron concentrations at the ingot level will be extremely useful prior to wafering. This can be achieved by accurate lifetime measurements and employing the method introduced by Zoth and Bergholz [21] and later modified for c-Si by Macdonald et al [22].

1.2 Thesis outline

Chapter 2 starts with a detailed explanation of different recombination mechanisms and their contribution to carrier lifetime in the bulk of semiconductor materials. The physics of surface recombination velocity and its impact on the measured (effective) lifetime, in contrast to the actual bulk lifetime, is then described. The later part of the chapter will briefly explain the techniques that are commonly used for material characterisation in PV research and development as well as

industry. The advantages of photoconductance characterisation methods are described in the final section of the chapter.

Chapter 3 gives a description of minority carrier lifetime measurements in crystalline silicon by quasi-steady state photoconductance and transient photoconductance decay. It includes the model that is used to describe the QSSPC measurements at the wafer level and, subsequently, extends it to semi-infinite thick samples. The proposed model by Bowden and Sinton [11] is used to overcome the challenges of significantly larger sample thickness than carrier diffusion length. The specifications of a BCT-400 boule tester from Sinton Instruments Inc is incorporated in the simulation tool during the calculation of the excess carrier density profile, as this system is used in this thesis for all measurements. The simulated initial QSS conditions are then used to model transient photoconductance measurements in thick samples to develop a comprehensive simulation tool for evaluation of measurement results on silicon ingots and blocks.

Chapter 4 employs the developed simulation tool to evaluate the accuracy of interstitial iron concentration measurements in boron-doped silicon blocks and ingots. The tool accepts several input parameters such as different concentrations of various doping as well as material impurities to simulate lifetime measurements at different injection levels. The Zoth and Bergholz [21] method is used in this chapter to determine dissolved iron concentrations from the differences between the simulated lifetime before and after dissociation of iron-boron pairs. Several lifetime measurement simulations are performed for different input Fe_i concentrations and calculated concentrations are compared with input variables to evaluate the accuracy of the Fe_i concentration measurements. In the experimental section, the interstitial iron determination results at different heights of a p-type multicrystalline silicon block from the middle of an ingot are compared with the results of wafers at corresponding heights from an adjacent block. In a separate work, dissolved iron concentrations

on a p-type multicrystalline silicon block are extracted with QSSPC as well as the photoluminescence intensity ratio (PLIR) imaging technique. Then, the block was wafered, and the [Fe_i] results from wafers are compared with the results of corresponding heights on the block.

Chapter 5 investigates the impact of high surface recombination velocities on transient lifetime measurements on semi-infinite thick silicon samples at a typical injection level of 10^{15} cm^{-3}. Here, the advantage of sample thickness is used to push photogeneration deeper in the bulk via using filters with longer cut-off wavelengths. This allows the peak of the excess carrier density profile to move further from the surface and significantly reduces the carrier diffusion to the unpassivated surface. The simulation results demonstrate an improvement in calculated transient lifetime results when the carriers are generated deeper in the bulk. The simulation results are compared with and confirmed by transient lifetime measurements performed on a p-type Cz silicon block at the end of the chapter.

Chapter 6 studies QSSPC lifetime measurements with filters with various cut-off wavelengths on thick c-Si blocks at a typical injection level of 10^{15} cm^{-3} in photoconductance lifetime measurements. The results show that there are some practical constraints when the QSSPC lifetime measurements are performed. One is from the reference cell which is commonly used to determine the cumulative photogeneration during the lifetime measurements in the QSSPC mode. Due to the External Quantum Efficiency (EQE) of the reference cell, there is a discrepancy between the photogeneration determined by the cell and the actual generation profile in samples. Therefore, an optical constant is calculated for each filter according to the reference cell EQE and the filter transmission profile to account for the difference between the photons absorbed by the reference cell and those absorbed by the sample. The RF coil which is used to sense changes in the sample conductance under illumination imposes the second constraint because of its depth sensitivity

profile. Hence, there will be an increasing uncertainty in the optical constant value, and change in the sensed conductance, for deeper photogeneration profiles. Simulations in this chapter demonstrate that pushing the excess carrier profile peaks deeper in the bulk up to certain limits improves the accuracy of QSSPC carrier lifetime estimates. In the experimental section of this chapter, transient lifetime measurement results with each filter are used as benchmarks to evaluate their performances in the QSS mode. Measurement results confirmed lower discrepancy between the transient and the QSS modes when the carrier profile peak is distant from the surface.

Chapter 7 concludes the findings in this thesis and the objectives which are met during the research. It also proposes some future endeavours that can be explored to investigate the consistency of the lifetime measurement results across different injection levels and possibly with results from the PLIR method. There are also possibilities of the determination of surface recombination velocity ranges by combination of measurements with short-pass and long-pass filters.

Chapter 2: Carrier lifetime and lifetime measurement techniques

2.1 Introduction

The chapter starts with an explanation of carrier generation and recombination mechanisms as well as the concept of carrier lifetime. Then various recombination mechanisms within semiconductor materials are explained along with their contributions to the lifetime of excess carriers. Then, the most common lifetime measurement techniques, which are currently used in silicon PV research and industry, are briefly introduced, followed by an explanation of the advantages of quasi-steady state photoconductance and transient photoconductance decay lifetime measurements techniques.

2.2 Generation, recombination and lifetime

The photovoltaic function is the conversion of an absorbed photon to an electron-hole pair under illumination. The absorption of photons with energies greater than or equal to the material bandgap, $E_{ph} \geq E_g$, generates electron-hole pairs by exciting electrons from the valence band (VB) to the conductance band (CB), leaving unoccupied holes in the valence band. In operating solar cells, the excess electron-hole pairs are collected by the metal contacts and flow to an external circuit to generate electric current. However, this excitement of the electrons to the conductance band is not a stable state, and the electrons may relax back into the available lower energy states (holes) in the valence band, releasing their excess energy through a process called recombination. The mechanisms are illustrated in figure 2-1.

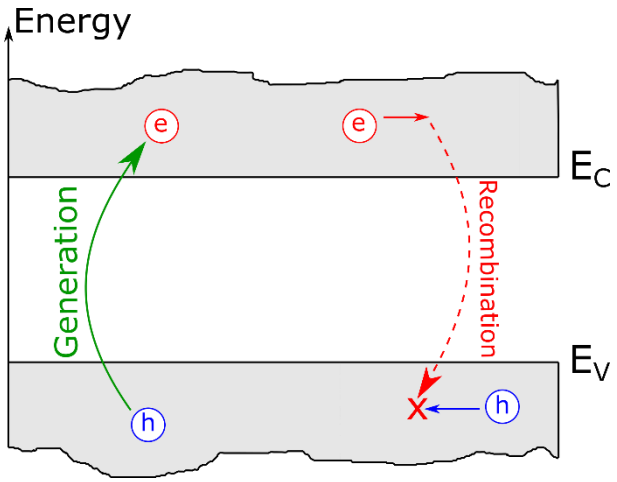

Figure 2-1: Electron-hole pair generation when an electron from the valence band is excited by an incident photon with $E_{ph} \geq E_g$ to the conduction band, leaving a vacant hole in the valence band. Electron-hole pair recombination when an excited electron relaxes back to a vacant hole in the valence band.

The 'minority carrier lifetime' of a semiconductor, symbolised by τ, is defined as the average time after electron-hole pair generation that a minority carrier stays in an excited state in the conduction/valance (electron/hole) band before recombining back to a lower energy state in the valence/conduction band.

For p-type silicon, the carrier lifetime is calculated from:

$$\tau_n = \frac{\Delta n}{U} \qquad 2\text{-}1$$

where Δn (cm^{-3}) is the excess minority electron carrier concentration, and U ($\mathrm{cm}^{-3}\mathrm{s}^{-1}$) is the recombination rate.

One of the most critical performance indicators of a solar cell is measured by the proportion of the generated excess carriers which are collected by metal contacts and fed to the external circuit before they recombine. Hence, the minority carrier lifetime is one of the most crucial parameters indicative of a material's electrical properties, as a higher lifetime will increase the probability of the carriers being collected by the cell contacts.

Recombination is the result of various mechanisms usually co-occurring within materials. These recombination mechanisms are generally categorised as intrinsic and extrinsic recombination. Intrinsic recombination always occurs even in the absence of any crystal defects or material impurities in an ideal material. However, extrinsic recombination only occurs in the presence of crystal defects or impurities in materials, which introduce energy states within the bandgap of materials. The excess energy of an excited electron can be released through emitting a photon during radiative recombination or can be transferred to a third carrier in a nonradiative Auger recombination process or released through emission of phonons.

2.2.1 Radiative recombination

Radiative band to band recombination occurs when the excess energy of an excited electron is released as a photon when the electron relaxes back to an empty energy state (hole) in the valence band. Each emitted photon's energy equals approximately to the bandgap of material. Hence, this is the inverse process to photogeneration in a solar cell, and the net recombination rate, U_{rad} depends on both the electron and hole concentrations which can be represented as [23]:

$$U_{rad} = B_{rad}(np - n_i^2) \qquad 2\text{-}2$$

where B_{rad} is the radiative recombination coefficient, n and p are the electron and hole concentrations respectively, and n_i is the intrinsic carrier concentration. In the case of non-equilibrium conditions in doped semiconductor materials, equation 2-2 can be expressed as:

$$U_{rad} = B_{rad}(n_0 + p_0 + \Delta n)\Delta n \approx B_{rad}(N_{A\,or\,D} + \Delta n)\Delta n \qquad 2\text{-}3$$

where $N_{A\,or\,D}$ is the doping concentration (acceptors/donors) and Δn is the excess carrier density. The probability of this type of recombination significantly reduces in indirect bandgap materials

due to the need for a phonon (a third particle) to complete the process. Hence, the radiative recombination coefficient, B_{rad}, for GaAs as a direct bandgap material, reduces from 3×10^{-10} to $3 \times 10^{-14}\text{cm}^{-3}\text{s}^{-1}$ [24] for Si which is an indirect bandgap semiconductor material.

Substituting equation 2-3 in equation 2-1 defines carrier lifetime due to radiative recombination:

$$\tau_{rad} = \frac{1}{B_{rad}(N_{A\ or\ D} + \Delta n)} \qquad 2\text{-}4$$

As mentioned above, the radiative mechanism is the dominant recombination in direct bandgap semiconductors like GaAs which is mostly used in optoelectronic devices such as Light Emitting Diode (LED) or laser sources. Various characterisation methods rely on radiative recombination to quantitatively investigate the optoelectrical properties of materials. The photoluminescence imaging technique is one the main methods in this category which will be explained in the second part of this chapter and is used as an independent technique for comparison in some of the studies in this thesis.

2.2.2 Auger recombination

Auger recombination is a nonradiative band-to-band transition in which an electron recombines with a hole and transfers its excess energy to either a conduction band electron or a valence band hole, which is highly excited into its respective band [25]. The third carrier will, consequently, release its excess energy as phonons to the crystal, in a process called thermalization. Whether the third carrier is an electron of the conduction band or a hole of the valence band, the Auger recombination rate, U_{Auger}, is either proportional to n^2p for the electron-electron-hole process (eeh-process) or to np^2 for electron-hole-hole (ehh-process) [26, 27]. Therefore, the net recombination in nonequilibrium conditions can be expressed as:

$$U_{Auger} = C_n(n^2p - n_0^2p_0) + C_p(np^2 - n_0p_0^2) \quad 2\text{-}5$$

where C_n and C_p are the Auger coefficients of the eeh- process and the ehh-process, respectively [23]. The Auger recombination lifetime, τ_{Auger}, can be calculated from 2-5 for the limiting cases of low- and high-level injection as below:

$$\tau_{Auger}^{LLI,n} = \frac{1}{C_n N_D^2} \quad \textit{for n-type} \quad , \quad \tau_{Auger}^{LLI,p} = \frac{1}{C_p N_A^2} \quad \text{for p-type} \quad 2\text{-}6$$

$$\tau_{Auger}^{HLI} = \frac{1}{(C_n + C_p)\Delta n^2} = \frac{1}{C_a \Delta n^2} \quad \text{for n-type and p-type} \quad 2\text{-}7$$

where $C_a = C_n + C_p$ is called the ambipolar Auger coefficient [28]. Dziewior and Schmidt [29, 30] determined the Auger coefficients, which are frequently used in the literature, for both n-type and p-type silicon when N_D, $N_A > 5 \times 10^{18}$ cm^{-3}, and are $C_n = 2.8 \times 10^{-31}$ cm^{-6}s^{-1} and $C_p = 9.9 \times 10^{-32}$ cm^{-6}s^{-1}. However, Sinton and Swanson measured C_a in the range of $10^{15} < \Delta n < 2 \times 10^{17}$ cm^{-3} to be 1.66×10^{-30} cm^{-6}s^{-1} which is about four times more than the sum of C_n and C_p [31].

Equations 2.5 - 2.7 are simplified equations expressing the Auger recombination mechanism. Theoretically, Auger recombination has much more complex calculations parameters such as Coulomb interactions between charge carriers [32, 33] and phonon involvement [34, 35] should also be considered as they affect the Auger recombination rate. Hence, to avoid the difficulty of theoretical determination of the Auger recombination parameters, an empirical parameterisation based on experimental lifetime measurements is often used to determine the Auger recombination rate, such as values from Kerr and Cuevas [36] and Richter *et al.* [30], which are used in this work.

Radiative recombination and Auger recombination are intrinsic recombination mechanisms due to intrinsic physical processes in the material which makes their presence unavoidable [37]. As shown in figure 2-2, radiative recombination is not a crucial factor in determining carrier lifetime in indirect semiconductor materials such as silicon. In contrast, Auger recombination often has a significant contribution to the final effective lifetime in silicon, particularly at high injection levels and in the heavily doped regions of solar cells [38].

Recombination through defects known as Shockley-Read-Hall (SRH) recombination is the dominant recombination mechanism at lower injection levels, particularly for mc-Si with relatively high impurities or defect levels. This extrinsic recombination is explained in detail in the following two sections.

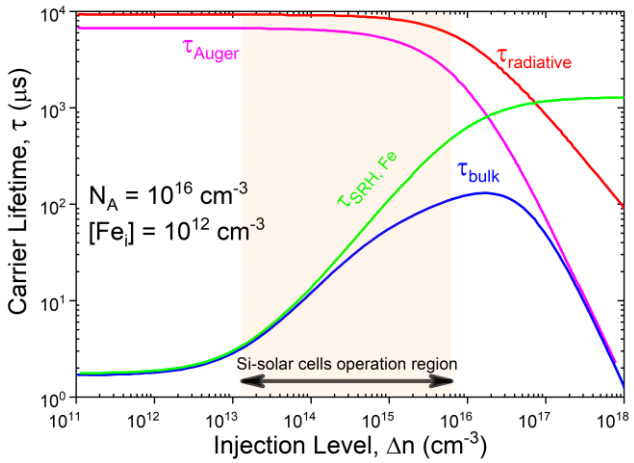

Figure 2-2: Various recombination mechanism contributions to the minority carrier bulk lifetime in crystalline silicon material as a function of injection level, Δn. Silicon solar cell injection level operation range is highlighted. Shockley-Read-Hall (SRH), τ_{SRH}, is the most influential recombination across the region followed by Auger recombination above $\Delta n = 10^{15}$ cm^{-3}. Radiative recombination, $\tau_{radiative}$, does not enforce significant limits on the bulk lifetime, τ_{bulk}.

2.2.3 Defect recombination in the bulk

The presence of defects within a semiconductor introduces discrete energy levels within the bandgap due to either impurities or crystallographic imperfections. These defects energy levels can be occupied either by an electron or a hole which may then interact with the conduction (CB) and the valence band (VB). An occupied defect energy level can either emit its electron into the CB (1) or capture a hole from the VB (3), while an unoccupied defect level can either capture an electron from the CB (2) or emit its hole into the VB (4). These four processes are illustrated in figure 2-3 where the direction of the solid and dashed arrows indicates the conventional direction of the electron and hole transition, respectively [23].

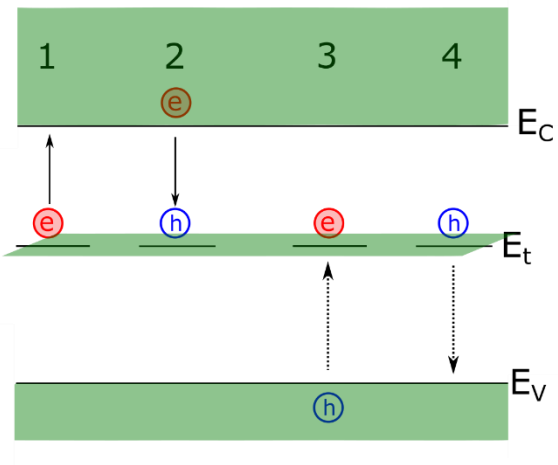

Figure 2-3: Energy band diagram showing the four possible interaction mechanisms of free carriers with a defect level in the band gap: electron emission (1), electron capture (2), hole capture (3) and hole emission (4). The direction of the solid and dashed arrows indicates the direction of the electron and hole transition, respectively [23].

The defect levels can be the sources of three types of two-step processes, which result from the mentioned four interactions as follows [23]:

Generation centre: two possible combinations can make a defect level play a role as a generation centre. When the defect level in a two-step emission process successively emits an

electron in the CB (1) and a hole in the VB (4), or if a two-step excitation process causes an electron from the VB firstly excited into the defect level (4) and then excited in the CB (1). Each of these two processes leads to the generation of an electron-hole pair.

Recombination centre: two possible combinations can make a defect level play a role as a recombination centre. When in a two-step capture process, a free electron from the CB (2) and a free hole from the VB (3) are successively captured by the defect level and annihilate each other. Alternatively, if in a two-step relaxation process, a free hole from the VB first relaxes to the defect level (3) and then relaxes to the CB (2), where it finally annihilates a hole.

Trap centre: The trapping process, which is neither recombination nor generation, occurs with those two-step processes when a carrier is captured at the defect centre and subsequently released back to the band from which it came, i.e., with the combinations (2) + (1) or (3) + (4). Thus, the defect centre interacts with only either the CB or VB.

The generation through a defect centre only becomes notable at a very low carrier concentration such as in a deeply depleted space charge region [39]. Hence, it does not impact the carrier lifetime measurements in this work, and only recombination and trapping process will be considered for further discussion in lifetime measurements.

One of the very effective two-step recombination processes through the defect levels occurs when a free electron in the conduction band relaxes into the valence band through recombining with a hole via an initial transition into the defect level (2+3) [40]. The excess energy is dissipated during the transition as phonons or in some cases as photons. The defect densities, their properties and the concentration of the electrons and the holes all impact the recombination rate. The Shockley-Read-Hall (SRH) statistics [41, 42] can model the net recombination rate for a single defect level as:

$$U_{SRH} = \frac{v_{th} N_T (np - n_i^2)}{(n + n_1)\sigma_p{}^{-1} + (p + p_1)\sigma_n{}^{-1}} = \frac{np - n_i^2}{\tau_{p0}(n + n_1) + \tau_{n0}(p + p_1)} \quad 2\text{-}8$$

where σ_n and σ_p are the capture cross sections of electrons and holes, υ_{th} is the thermal velocity of the charge carriers, and N_T symbolises the density of the defect. τ_{n0} and τ_{p0} are the capture time constants of electrons and holes respectively and are defined as:

$$\tau_{p0} = \frac{1}{N_T \sigma_p v_{th}} \quad , \quad \tau_{n0} = \frac{1}{N_T \sigma_n v_{th}} \quad 2\text{-}9$$

n_1 and p_1 are called SRH densities and are the electron and hole equilibrium densities when the Fermi level coincides with the defect energy level (E_t), and are calculated from:

$$n_1 = N_C \exp\left(\frac{E_t - E_C}{kT}\right), \quad p_1 = N_V \exp\left(\frac{E_C - E_g - E_t}{kT}\right) \quad 2\text{-}10$$

where N_C and N_V are the effective densities of states in the CB and VB, respectively, and E_C and E_g the energies of the CB edge and bandgap.

Replacing the non-equilibrium densities by $n = n_0 + \Delta n$ and $p = p_0 + \Delta p$ with negligible carrier trapping assumption ($\Delta n = \Delta p$), the SRH lifetime can be expressed as:

$$\tau_{SRH} = \frac{\tau_{p0}(n_0 + n_1 + \Delta n) + \tau_{n0}(p_0 + p_1 + \Delta p)}{n_0 + p_0 + \Delta n} \quad 2\text{-}11$$

2.2.4 Defect recombination at interfaces

An abrupt discontinuity in the crystal structure occurs at the surface of a silicon bulk (substrate) [23, 40], at the interfaces with other materials, or of grain boundaries in the case of multicrystalline silicon. The structure disruption results in many partially bonded silicon atoms which, therefore,

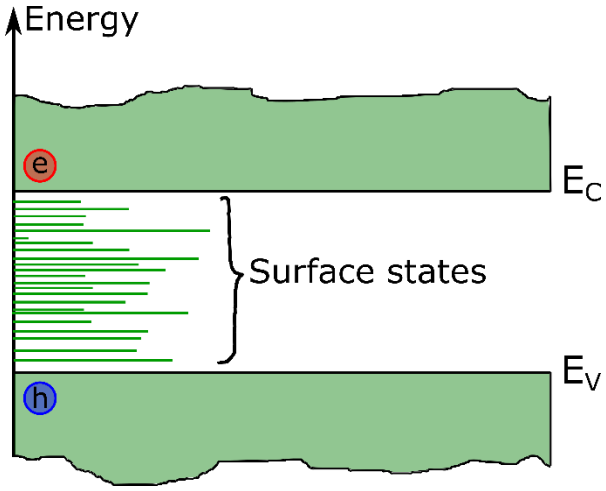

Figure 2-4: Surface or defect states continuously distributed within the bandgap at the interface of a semiconductor, providing a semi-infinite pool of energy states in the bandgap for electron-hole pair to recombine immediately.

form significant densities of recombination-active defect levels. Hence, the bandgap near the silicon interface contains an almost continuous disruption by defect energy states in [43] shown in figure 2-4. Therefore, surface recombination can be assumed as a special case of SRH recombination, although unlike bulk SRH defect levels, interface states do not occupy a single energy level within the bandgap [23]. Hence, the recombination rate at the surface can be calculated by SRH statistics model while replacing N_t with $D_{it}(E_t)$ and integrating over the entire bandgap [23]:

$$U_{surf} = (n_s p_s - n_i^2) \times \int_{E_V}^{E_c} \frac{v_{th} D_{it}(E_t) dE_t}{[n_s + n_1(E_t)]\sigma_p^{-1}(E_t) + [p_s + p_1(E_t)]\sigma_n^{-1}(E_t)} \qquad 2\text{-}12$$

where $D_{it}(E_t)$ is the interface trap density at a given energy level, $\sigma_n(E_t)$ and $\sigma_p(E_t)$ are the electron and hole capture cross sections for each defect level, n_s and p_s are electron and hole concentrations at the surface.

Unlike bulk recombination rates which are defined per unit volume, the surface recombination rate is determined per unit area.

The Surface Recombination Velocity is defined as:

$$SRV = \frac{\Delta n_s}{U_{surf}} \qquad 2\text{-}13$$

This represents the integration of all surface defect parameters in equation 2-12 as a single effective parameter, providing a quantified value for direct comparison of different surface passivation schemes as well as assessing their qualities [23].

The large number of energy-dependent variables in equation 2-12 makes the SRV not only dependent of the surface conditions, but, also the injection level and bulk lifetime dependence as has been discussed in detail by Aberle [44].

The impact of surface recombination is significantly reduced by surface passivation during the cell manufacturing process. Therefore, separating the bulk and surface lifetimes enables the characterization to focus on persistent defect in the bulk for defects engineering purposes to increase final cell efficiency.

2.2.5 The Effective lifetime τ_{eff}

As shown in equation 2-1, the recombination rate and excess carrier density are needed to determine the carrier lifetime in silicon. The total effective recombination rate is the rate of total recombination which occur concurrently in the bulk and the surface of a material:

$$U_{effective} = U_{bulk} + U_{surf} \qquad 2\text{-}14$$

$$\frac{1}{\tau_{effective}} = \frac{1}{\tau_{bulk}} + \frac{1}{\tau_{surface}}$$

As discussed before, surface passivation techniques significantly passivate the recombination centres at the interfaces. Thus, recombination mechanisms in the bulk often remain the crucial part of excess carrier lifetime determination in silicon material characterization. The bulk recombination is composed of radiative, Auger and SRH recombination which form the material bulk lifetime:

$$U_{bulk} = U_{rad} + U_{Auger} + U_{SRH-bulk}$$

$$\frac{1}{\tau_{bulk}} = \frac{1}{\tau_{rad}} + \frac{1}{\tau_{Auger}} + \frac{1}{\tau_{SRH-bulk}} \qquad \text{2-15}$$

so, the final effective lifetime is calculated as:

$$\frac{1}{\tau_{eff}} = \frac{1}{\tau_{rad}} + \frac{1}{\tau_{Auger}} + \frac{1}{\tau_{SRH-bulk}} + \frac{1}{\tau_{surface}} \qquad \text{2-16}$$

The effective lifetime can be measured with several lifetime measurement techniques of which the more dominant ones in silicon photovoltaic research are discussed in the following sections. As illustrated in figure 2-2, different recombination mechanisms show a distinctive injection dependence which causes significant variations in their contribution to the effective lifetime at different injection levels. While SRH recombination often has the dominant impact on the effective lifetime at low injection levels, Auger recombination is the mechanism which usually limits the effective lifetime at high injection levels. As mentioned earlier, radiative recombination generally

has negligible impact in comparison with other recombination mechanisms in indirect semiconductor materials like silicon.

2.3 Characterisation techniques

A key purpose of silicon optoelectrical characterisation is to identify the deep levels of recombination-active defects in the bandgap as well as identify trapping centre states, as they significantly change carrier dynamics. As a direct measure of the charge-recombination activity, excess carrier lifetime measurement is a fundamental part of characterisation due to its direct impact on device performance. The excess carrier lifetime of silicon materials and devices can be determined by several techniques in the PV industry. Various optoelectronic properties can be utilised to perform lifetime measurements, of which the most common ones are photoluminescence, photoconductance, and photovoltaic response. In this section, the most common techniques which are dominantly used in silicon PV research and development, as well as quality monitoring in industry, will be briefly described.

2.3.1 Surface Photo-Voltage SPV

Surface Photo-Voltage (SPV) is a well-established contactless method based on the linear dependence of the surface photovoltage on the excess carrier density at low signal levels. Depending on the photon energy and the intensity of the light source, the surface photovoltage can be used for characterisation of surface properties and bulk parameters [45, 46]. SPV uses the minority carrier diffusion length to measure the excess carrier lifetime as well as nanostructure characterisation of quantum dots and nanowires [45, 47, 48].

As mentioned in detail in section 2.2.4, the termination of the bulk crystal structure of a semiconductor at surfaces (free or internal surfaces) forms surface-localized electronic states

within the semiconductor bandgap (figure 2-4) and/or a double layer of charge, known as a surface dipole layer [49]. As illustrated in figure 2-5, these surface-localised electronic states initiate a charge transfer process between bulk and surface resulting in the formation of a non-neutral region named the surface space charge region (SCR) [50].

The absorption of light with photon energy higher than the bandgap of the sample generates electron-hole pairs via band-to-band transitions in the semiconductor. The excess carriers in the bulk diffuse towards the surface to be redistributed by the electric field within the surface SCR and, thus, changes the surface potential drop. Kronik and Shapira [45] showed that the measured photovoltage value, ΔV_s, is proportional to the surface electric potential under illumination.

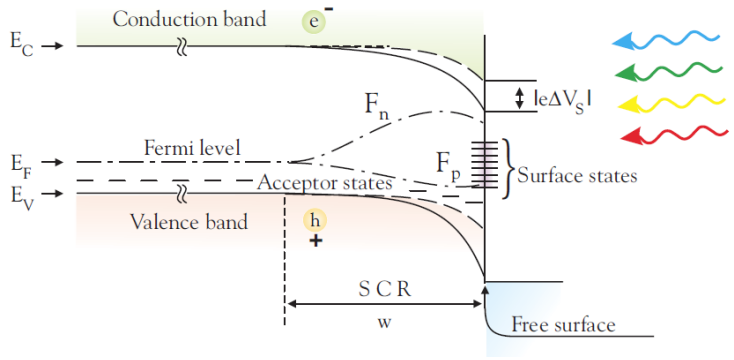

Figure 2-5: P-type semiconductor surface under illumination. F_n is the electron quasi-Fermi-level. F_p is the hole quasi-Fermi-level. ΔV_s is the surface potential drop (PV signal) (figure from [50]).

A typical SPV setup is shown in figure 2-6, the light is chopped, and its frequency used as a reference signal for a lock-in amplifier to overcome the noise inherent in the low signal level. The measured PV signal is defined:

$$U = C_{SPV} \cdot \left[\frac{qI\alpha L}{1+\alpha L}\right] \qquad 2\text{-}17$$

Where C_{SPV} is the method coefficient (constant value), q is the elementary charge, I is the light intensity, α is the absorption coefficient, and L is the diffusion length.

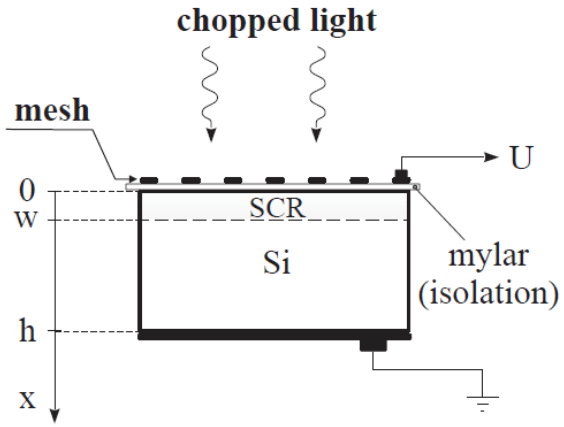

Figure 2-6: A photovoltage is generated by chopped light. This photovoltage is then induced from the semiconductor surface at the mesh or another conductive and transparent electrode (figure from [50]).

Constant SPV approach is a method to perform the measurement which maintains a constant PV signal level at various wavelengths by varying the light intensity, then:

$$I(\lambda) = C_{SPV}.[\alpha^{-1}(\lambda) + L] \qquad 2\text{-}18$$

which then allows the diffusion length, L, to be found by extrapolation of plotting the light intensity, $I(\lambda)$, as a function of $\alpha^{-1}(\lambda)$ as illustrated in figure 2-7.

Non-constant SPV approaches can characterise other properties of materials in which the SPV signal can be interpreted according to the wavelengths and the intensity of the light source. Different scenarios are explained below for the case of p-type materials, but the inverse signs apply to n-type materials.

In the case of the light source with photon energy equal to the material bandgap, the increase of the light intensity significantly increases the SPV signal due to a linear increase in electron-hole

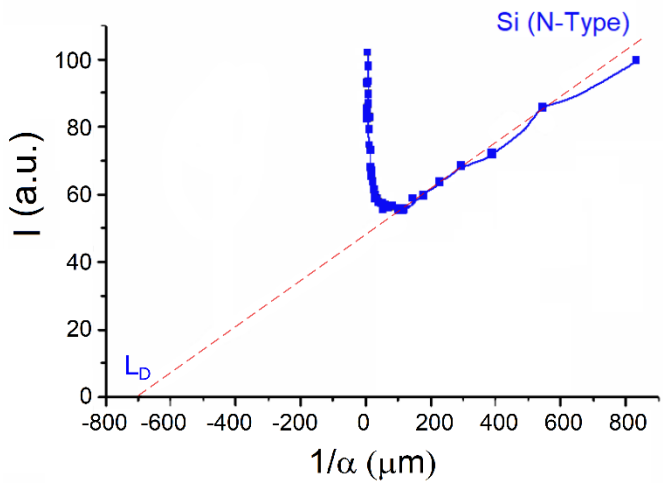

Figure 2-7: The extraction of the minority carrier diffusion length by "constant SPV" method (figure from [50]).

pairs generation. Such a feature of the SPV technique is utilised for bandgap characterisation of several semiconductor materials [51-53].

Increasing the light intensity when photon energies are larger than the material bandgap causes the SPV signal value to be saturated which enables the SPV signal spectrum in this range to be analysed for phase segregation investigations [45, 46].

When the light source of photon energies with lower than the material bandgap is used, two different cases can happen. If the illumination promotes the excitation from the defect energy levels in the middle of bandgap to the conduction band, the surface band bending (ΔV_s in figure 2-5) reduces and decreases the SPV signal. On the other hand, an increase in SPV signal suggests more surface band bending due to the promotion of the optical transitions from the defect energy states to the valence band. Therefore, SPV spectroscopy is a suitable method for defect characterisation in semiconductor materials.

2.3.2 Beam Induced Current (BIC) methods

The characterisation methods based on beam-injection via Scanning Electron/Optical Microscopy (SE/OM) [54], tools have been popular in PV research for many years. The techniques are frequently used for both fundamental physics questions and industrial purposes. The physics of both methods are very similar, except the excess carrier generation rate distribution is different because of the difference in the focused beam used to generate excess carriers in the two methods [55]. The Light (Optical) Beam Induced Current LBIC technique (OBIC) applies a laser source for carrier generation, while the Electron Beam Induced Current (EBIC) techniques excites the carriers with a focused electron beam.

The generated excess carriers diffuse throughout the quasi-neutral region of the device and a fraction of them reaches to the p-n junction [55]. The electric field inside the depletion region separates electron-hole pairs and sweeps them out of the depletion region, thereby generating a current [56]. A metallised p-n junction or a Schottky ohmic contact creates electrodes to collect the current from the sample which, then, will be amplified to a measured signal in these methods [57]. A map can be obtained via scanning the sample surface with the beam while simultaneously measuring the induced current profile *I (y)*, where *y* is the beam position at the sample surface [49]. The collected current from the sample surface is:

$$I = qD \iint_{x=0}^{W} \frac{\partial \Delta n}{\partial x}\, dy\, dz \qquad 2\text{-}19$$

where q is the electron charge, D is diffusion coefficient, Δn is the minority carrier concentration, and x is the sample depth along the beam axis (perpendicular to the sample surface). The created

map is a function of the collected current magnitude which, itself, depends on the strength of defects as recombination centres as well as the beam distance from defects.

Since both methods have similar principles, this section will briefly explain the LBIC as it more frequently used for PV applications due to its extra features such as measuring the sample surface reflectance as well as identifying spatial inhomogeneity due to grain boundaries or other crystal defects in materials [58]. Moreover, maps with higher contrast are obtained by applying lasers with longer wavelengths in the LBIC technique [59], while the higher energy electron beam in EBIC may damage the sample surface.

LBIC is also capable of measuring minority carrier lifetimes indirectly through diffusion length measurements on solar cells. Induced currents generated by applying various wavelength lasers are collected at different penetration depths. The relative collected currents reflect the Internal Quantum Efficiency (IQE) which are calculated at each wavelength. The effective diffusion length can be then determined by extrapolation of the inverse of IQE plotted as a function of the inverse absorption coefficient at different wavelengths, as illustrated in figure 2-8.

As can be seen, more accurate results can be obtained with more measurements at various wavelengths. The minority carrier lifetime is then calculated from:

$$\tau_{eff} = \frac{\left(L_{eff}\right)^2}{D} \qquad 2\text{-}20$$

A disadvantage of LBIC mapping is that it is time-consuming, where for example a map with a resolution of 100 μm from a 156 mm× 156 mm silicon sample can take several hours to be completed [58]. In addition, despite being a non-destructive characterisation method, BIC methods are less convenient due to their need for junction formation and metal contacts collect to the beam induced current.

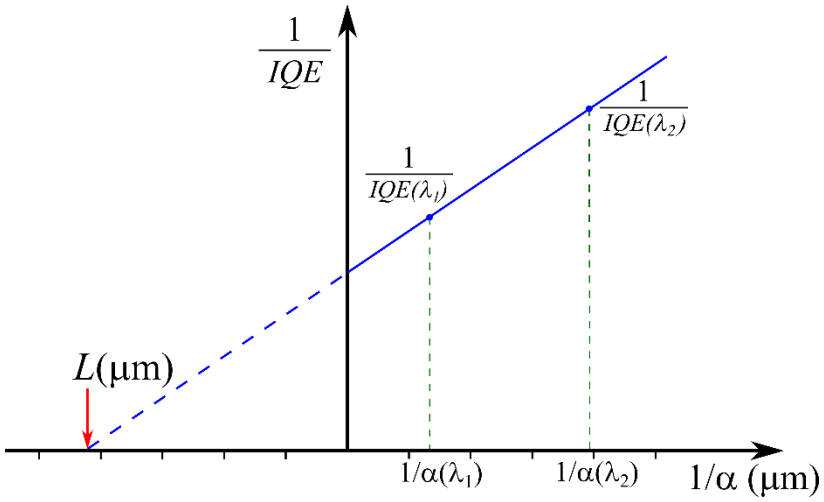

Figure 2-8: Carrier diffusion length, *L*, can be determined from extrapolation of the inverse of internal quantum efficiency plotted as a function of the inverse absorption coefficient at different wavelengths (λ_1 and λ_2). The theory is similar to the SPV technique.

2.3.3 Photoluminescence (PL)

Luminescence is the observation of the emitted light due to external excitation source from specific classes of materials, and which is not due to temperature increase (blackbody radiation) [43, 56]. The term Photoluminescence (PL) refers to the luminescence due to material stimulation via an external light source. In crystalline semiconductor materials, luminescence occurs when the excited electrons from the conduction band relax back to a valence band state while releasing its excess energy, or a part of it, (as discussed in section 2.2.1 the rest is released as a phonon in the case of indirect bandgap materials such as crystalline silicon (c-Si)) via emitting photons. The PL technique is used in various forms such as spectral luminescence measurements or PL imaging for material characterisation investigating properties like crystal defects, impurities, and excess carrier density and lifetime. In this section, PL imaging is explained as it used in some parts of this thesis as an independent technique to compare with the results of quasi-steady state photoconductance measurements.

Depending on the characterisation objectives, silicon or InGaAs charge coupled device (CCD) cameras are usually used to capture megapixel images of the luminescence emissions from the samples. Trupke *et al*. [60] employed PL imaging of silicon wafers with an expanded high power fibre-coupled diode laser for uniform illumination of the entire sample simultaneously. The sample is kept under continuous illumination to maintain true steady state conditions while the luminescence emission is captured by the camera. The challenge in this technique is the strong light reflection from the sample surfaces, particularly those with unpassivated surfaces, which can be up to 12 orders of magnitude larger than the sample luminescence signal. Hence, sophisticated filtering is required during the PL imaging measurements to eliminate the reflected signal while capturing the significantly weaker luminescence signal. However, high-resolution minority carrier lifetime images on passivated silicon wafers with the PL imaging technique can be obtained in fractions of a second [61], where previously several hours were required, using techniques like microwave photoconductance decay mapping or LBIC [43].

Amongst the other techniques, photoluminescence imaging has also attracted interest recently for multicrystalline silicon brick and monocrystalline ingot characterisation. This will provide invaluable immediate process feedback during crystallization as well as early-stage characterisation data in solar cell fabrication [11, 43]. The primary advantage of characterisation on thick samples is that the minority carrier lifetime measurement is significantly less affected by the rear surface recombination than in wafer measurements [12]. It has been shown that the PL intensity under low injection conditions not only depends on the minority carrier density, Δn, but also the doping densities, $N_{A/D}$ [62]. Thus, a challenge is introduced to PL imaging lifetime techniques at ingot and brick levels, as the doping densities vary along the sample's length. Trupke *et al*. [63] introduced a two-filter Intensity Ratio, PLIR, method to address this challenge by

correcting the doping variations. The technique was initially employed to determine the diffusion length on silicon solar cells [64] and is based on the ratio of two PL signals measured at any location with the PL detector sensitivity tuned to two different spectral ranges. This can be practically achieved by inserting two filters with different spectral ranges in front of the camera lens during the measurements when the luminescence signals are being captured. Mitchell *et al.* [14] combined the PLIR imaging technique with analytical models for the carrier distribution as a function of bulk lifetime to generate a lifetime (or diffusion length) image in which the background doping variation dependency was eliminated. There have been other absolute lifetime approaches in which dynamic calibrations employed to adjust for doping variations along the ingot [65].

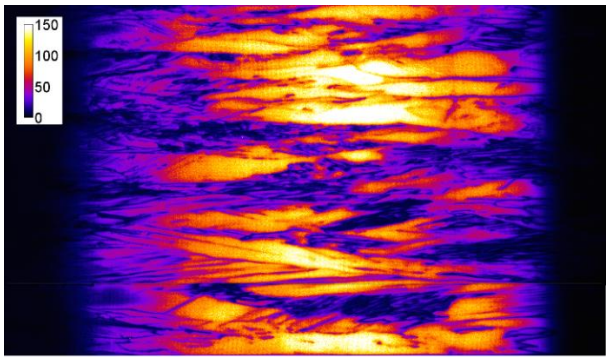

Figure 2-9: A sample bulk lifetime image of the side of a 6-inch high multicrystalline silicon brick obtained using the PL intensity ratio method. The scale bar represents the lifetime in microseconds, the left to the right represents the bottom to the top of the ingot (figure from [9]).

An example of a bulk lifetime image of a p-type multicrystalline silicon brick taken with the PLIR method is shown in figure 2-9. The typical low bulk lifetime regions in the top and bottom sections of a cast multicrystalline ingots are visible in the image. The low lifetimes suggest the presence of impurities (primarily iron) diffused from the crucible into the bottom of the ingot as well as segregation and subsequent solid-state impurity diffusion at the top. The dark lines represent recombination active structural defects such as grain boundaries as well as dislocations, with an increasing density towards the top of the ingot [43].

PL imaging techniques are also capable of characterising silicon wafers as well as finished solar cells, which make it used not only for faster process feedback in wafer manufacturing but also for effective quality control [43].

2.3.4 Microwave Photoconductance Decay (µPCD)

Microwave-detected photoconductance decay (µPCD) is a technique based on monitoring a sample photoconductance changes to measure the carrier lifetime. The carrier lifetime is determined from the rate in which an initial excess carrier density decays asymptotically to equilibrium conditions [66]. The changes in photoconductance are measured via changes in the microwave reflectance from the sample [67, 68].

The highly non-linear dependency of the microwave reflectance on the free carrier density restricts the µPCD to a small signal technique [23, 69]. Although there is no constraint on measuring carrier lifetime by the µPCD at low injection levels, lifetime measurements at high injection levels require an additional steady-state bias light. The bias light generates the desired background carrier density to superimpose the small-signal transient pulse which allows the changes in microwave reflectance to be detected. The first complication of using a bias light is that a differential effective lifetime, $\frac{\partial \tau_{eff}}{\partial \Delta n}$, is measured, rather than the actual effective lifetime. To determine the actual effective lifetime, τ_{eff}, in the presence of the bias light, the differential effective lifetime needs to be measured across a broad range of lower carrier densities and then integrated. Furthermore, the reflectance signal does not include the absolute magnitude of excess carrier density. Therefore, the bias light must be calibrated to calculate the steady-state generation rate in the sample, which eliminates the simplicity of the transient measurements as one of its advantages [23].

2.3.5 Quasi-Steady State Photoconductance and Transient Photoconductance

Sinton and Cuevas [7] introduced the quasi-steady-state photoconductance measurement which is a contactless [70] technique used to determine the lifetime of photogenerated excess carriers in semiconductor samples [71]. In this section, the techniques and their applications in lifetime measurements of various samples are briefly introduced, but the detailed physics behind the methods is discussed in depth in the next chapter.

The tools used in this project for both wafers and bulk (thick) lifetime measurements are from Sinton Instruments Inc. The tools are capable of performing lifetime measurements in both quasi-steady-state and transient modes at both wafer (WCT-120) and ingot (BCT-400 for brick, slab, and any other thick sample) levels. The WCT-120 can also perform a so-called generalised analysis at the wafer level as explained in detail in [72].

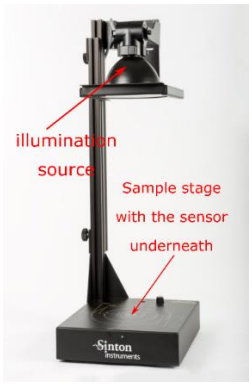

Figure 2-10: A Sinton WCT-120 setup used for silicon wafer characterisation. The conductive RF sensor coil is located under the sample stage (image source Sinton Instruments).

As shown in figure 2-10, the WCT-120 uses a regular xenon flash as its light source with any desired IR filter inserted in front of the flash. The sample is placed on the stage with a conductive coil underneath which is a part of a high-frequency AC circuit. There is also a reference solar cell located on the edge of the stage that used to measure the generation rate which is needed during quasi-steady state measurements.

The excess carrier densities are generated in the sample by a light pulse from the xenon flash. The charge carriers interact with the high-frequency electromagnetic field and generate eddy

currents that are either detected with a second coil acting as receiver or monitored as changes in the phase and amplitude of the current flowing in the primary coil [58]. The changes in the sample electrical conductance due to a changing excess carrier density cause a change in this eddy current and a corresponding change in the phase and amplitude of the current in the AC circuitry. Since the method detects the change in the sample conductance, the presence of metals with their significantly larger conductivity introduces large errors in lifetime measurements. Hence, the measurements must be performed before metal contacts are deposited [58]. The WCT-120 a very well-established tool for carrier lifetime measurements on silicon wafers in photovoltaics for both R&D and industrial applications.

The BCT-400 is a tool for lifetime measurements on semi-infinite thick samples where the sample thickness is significantly larger than the excess carrier diffusion length. The tool has very similar components as the WCT-120 except that the bulk thickness of samples imposes several modifications in the physical design, as well as defining new variables. The detailed analysis and explanation of the setup are provided in the next chapter where the photoconductance lifetime measurements in thick samples are modelled and simulated.

The photoconductance lifetime measurement technique has several advantages and is widely used across research and development laboratories as well as various industries from crystalline silicon growth to solar cell manufacturers. Their main advantage, perhaps, is the capability of non-destructive and fast characterisation that can be performed in laboratory and industrial environments. Several material properties such as minority carrier lifetime across a broad range of injection levels, doping concentrations, and sample resistivity can be directly characterised by this technique. The method is also able to indirectly characterise other parameters such as material impurities (e.g. $[Fe_i]$ in p-type C-Si) and trap densities [16, 73].

Chapter 3: Simulating photoconductance lifetime measurements in crystalline silicon ingots

3.1 Introduction

This chapter contains the description of a model which has been developed to simulate carrier densities of photoconductance under Quasi-Steady State (QSS) conditions and, eventually, QSSPC lifetime measurements in a semi-infinite thick semiconductor sample. The key property in these samples is their thickness, which is significantly longer than the charge carrier diffusion length. The model is further extended to lifetime measurements in transient conditions where the light source is terminated after the QSS condition is reached within the sample bulk and, subsequently, the excess carrier density decays because of recombination in the absence of generation.

3.2 Simulating QSSPC lifetime measurements

Quasi-Steady State conditions in a sample with an almost infinite thickness in comparison to the carrier diffusion length is simulated here. First, the photogeneration profile from the desired light source in the sample is modelled. Then, the carrier density profile under quasi-steady state conditions is determined based on the generation profile, boundary conditions, and the bulk properties of the material. The final step is to calculate the effective lifetime in the sample.

The QSSPC technique was introduced by Sinton and Cuevas [7] to simplify the carrier lifetime determination for lifetimes lower than those measurable with transient photoconductance decay. The generation and recombination rates of electron-hole pairs are perfectly balanced across the whole sample thickness under steady-state conditions in semiconductor materials. Therefore, the

excess charge carrier effective lifetime, τ_{eff} (s), at a given injection level, Δn (cm^{-3}), can be determined from:

$$\tau_{eff} = \frac{\Delta n\, W}{g_{cum}} \qquad 3\text{-}1$$

where W (cm) is the sample thickness, and g_{cum} is the cumulative areal carrier generation rate (cm^{-2}) over the entire thickness [not to be confused with the conventional volume generation rate, G (cm^{-3})]. In other words, an approximately direct method to determine the excess charge carrier effective lifetime in a silicon sample is to determine Δn and g_{cum} during the quasi-steady state lifetime measurement.

As the sample conductance, σ, reflects the total charge carriers within the sample, measuring the change in the sample conductance under illumination, $\Delta\sigma$, (photoconductance) can probe the photogenerated excess carrier density in the sample, Δn_{total}. Therefore:

$$\Delta n_{total} = \frac{\Delta\sigma}{q\,(\mu_n + \mu_p)} \qquad 3\text{-}2$$

where μ_n and μ_p are the electron and hole mobilities, respectively which themselves are functions of doping concentration and injection level in the sample. Accurate values for carrier mobilities in silicon, as the most common material in semiconductor research, have been widely determined in the literature [39, 74]. The mobility values in this thesis are from Klaassen [75, 76] and are slowly varying functions of the carrier density and temperature.

It should be noted that in typical thin samples (wafers) where the minority carrier diffusion length is usually significantly larger than the sample thickness, the excess carrier density profile is almost uniform across the entire sample thickness. Hence, the injection level, Δn, is the arithmetic

mean of total photogenerated charge carriers in the sample and, therefore, it is determined by total excess carrier density, Δn_{total}, divided by the sample thickness, *W*:

$$\Delta n = \frac{\Delta \sigma}{q\,(\mu_n + \mu_p)W} \qquad 3\text{-}3$$

However, as it will be shown in section 3.2.2, the excess carrier density profiles are not uniform in semi-infinite thick samples and, as a result, using the arithmetic mean is not an accurate representation of injection levels to determine the excess carrier effective lifetime. It will be shown in section 3.2.3 that a weighted-average value, Δn_{avg}, needs to be defined when measuring a semi-infinite thick sample.

Replacing the Δn from equation 3-3 in equation 3-1 results in an approximately direct method to determine excess carrier effective lifetime in crystalline silicon:

$$\tau_{eff} = \frac{\Delta \sigma}{q\,(\mu_n + \mu_p) g_{cum}} \qquad 3\text{-}4$$

Equation 3-4 indicates that the excess carrier effective lifetime can be determined by measuring the change in sample conductance due to the photogenerated charge carriers, $\Delta \sigma$, and the total areal photogeneration rate in the sample, g_{cum}. As mentioned previously in chapter 2, an RF sensor coil is employed in the QSSPC lifetime measurement technique for contactless measurements of the change in the sample conductance due to photogeneration. The incident light from the light source which hits the sample is also measured by a reference solar cell, and the corresponding g_{cum} is determined according to the sample properties such as surface conditions and sample thickness [7].

3.2.1 Photogeneration

Determining the generation rate is the initial step for the QSS lifetime measurement as indicated in equation 3-1. The incident light on the sample in this model can be selected from various light sources from any monochromatic light, with a wavelength of λ, to full spectrum wavelengths excluding those with energy less than crystalline silicon bandgap (approximately 1.14 eV) to generate an electron-hole pair in silicon.

The photon flux, $N_{ph-\lambda}$, of any monochromatic light at a given depth, *x*, of the sample can be calculated from:

$$N_{ph-\lambda}(x) = N_{ph-\lambda}(0)[1 - e^{-\alpha x}] \quad 3\text{-}5$$

where $N_{ph-\lambda}\ (0)$ is the photon flux at the sample surface, and α is the light absorption coefficient.

The excess carrier generation within a sample with thickness of W due to illumination is:

$$G_{\lambda} = \frac{N_{ph-\lambda}(0)}{W}\ e^{-\alpha W} \quad 3\text{-}6$$

The total carrier generation for a white light source can be calculated by:

$$G_{cum} = \sum_{\lambda=310nm}^{\lambda=1200nm} \frac{N_{ph-\lambda}(0)}{W}\ e^{-\alpha W} \quad 3\text{-}7$$

Figure 3-1.a shows the light absorption depth in crystalline silicon as a function of wavelength. As can be seen, the absorption depths for light with wavelengths of less than 800 nm is shorter than 10 µm. Therefore, the light spectrum in that range has a negligible contribution to the photogenerated excess carrier densities in the bulk of silicon samples.

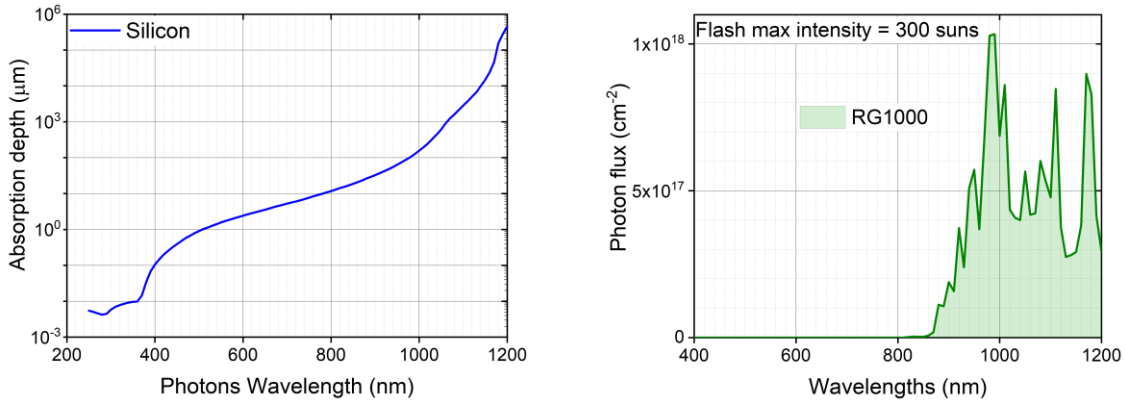

(a) (b)

Figure 3-1: (a) Photon absorption depth in crystalline silicon as a function of wavelength. (b) The xenon flash photon flux spectrum filtered by a standard RG1000 IR filter (prefiltered light intensity equivalent of 300 suns).

Since the purpose of crystalline silicon material characterisation is to identify the bulk properties, the shorter wavelength spectrum is usually removed using an Infra-Red (IR) filter. Thus, the characterisation signals contain more information about material properties deeper in the bulk.

Figure 3-1.b illustrates the xenon flash spectra (equivalent of 300 suns) filtered by a standard 1000-nm IR-Pass Schott glass (RG1000) filter used in a Sinton Instrument BCT-400 (frequently used in this work for silicon ingot characterisation) for lifetime measurements. The use of such a simple light source in contrast with monochromatic laser sources is one of the practical advantages of the boule tester. This allows the tool to be used in different environments without the complexity of radiation safety regulations and system maintenance.

The flash power was set to 400 Ws with a 3.8 ms decay constant in all the measurements in this work. The assumption of steady state conditions is only valid for the bulk lifetime range of less than 150-200 μs where the QSSPC mode is an appropriate technique to be employed. Therefore,

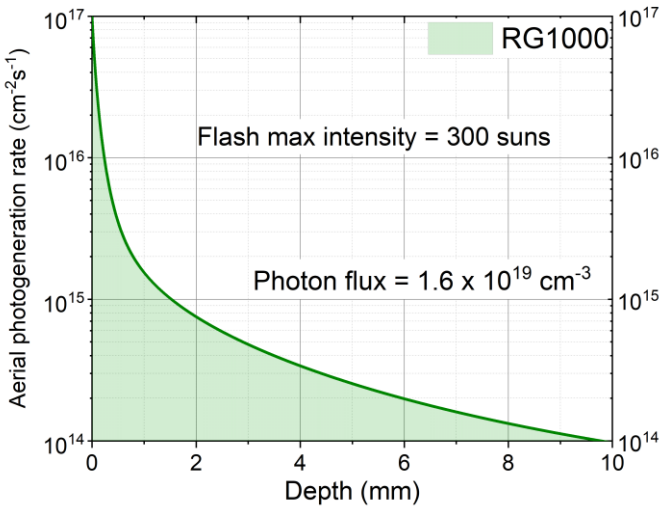

Figure 3-2: Areal photogeneration rate as a function of samples depth generated using the RG1000 to filter xenon flash spectrum with 300 suns maximum intensity.

the decay time constant is sufficiently long to ensure there is no dynamic changes in the carrier densities while the flash peak is decaying during lifetime measurements [7, 8].

The photogeneration profile from the RG1000 spectrum in a crystalline silicon sample is shown in figure 3-2. The photogeneration rate was calculate from the part of photon flux, which is absorbed by the sample and, then, calculating absorption depth of each wavelength based on its coefficient. It can be observed that the excess carriers photogeneration drops more than two orders of magnitude only within the first 2 mm of the sample.

3.2.2 Carrier density profile

Cuevas [77] proposed a model to simulate quasi-steady state conditions in silicon wafers, utilizing numerical analysis in order to calculate the carrier density profile for a given thickness, *W*. Subsequent determination of the excess photoconductance, $\Delta\sigma$, as well as the cumulative photogeneration, g_{cum}, in the sample eventually determine τ_{eff} from equation 3-4.

As illustrated in figure 3-3, a Δx thickness interval [10, 77] is assumed to be small enough to ensure the electron current across the Δx thickness can be considered constant. At any time, *t*, the excess carrier density within the volume created by Δx thickness can increase (green colours) due to the injection of electrons into that volume, $-J_n(x,t)$ (assuming p-type material), or because of the photogeneration occurring within it, $G(x,t)$. The mechanisms that decrease (red colours) carriers concentrations are the current that leaves the slice of material, $J_n(x+\Delta x,t)$, and recombination within it, given by $U(x,t)$ which is the volume recombination rate that represents all recombination mechanisms described in the previous chapter.

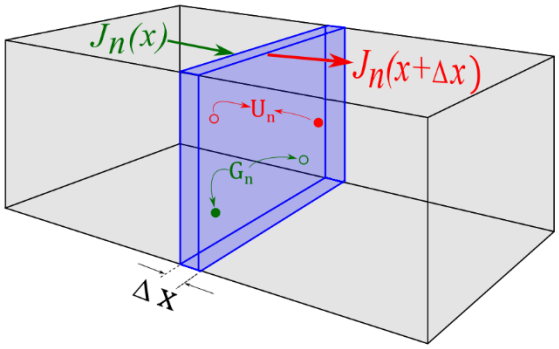

Figure 3-3: The sample thickness interval Δx with the constant electron current across it. Electron injection into ($J_n(x)$) and the photogeneration (G_n) within the interval increase the excess carriers density (Δn) whereas electron injection out of ($J_n(x+\Delta x)$) and the carrier recombination (U_n) within the interval decrease the excess carriers density (Δn).

Thus, the change in the carrier density at any time, *t*, within the Δx interval can be calculated from [78]:

$$\frac{\partial \Delta n(x,t)}{\partial t} = G(x,t) - U(x,t) + \frac{1}{q}\left(-J_n(x+\Delta x,t) + J_n(x,t)\right) \qquad 3\text{-}8$$

In steady state conditions, in which the excess carrier densities do not change over time, and $\frac{\partial \Delta n(x,t)}{\partial t} = 0$, the total augmentation and reduction mechanisms are perfectly balanced, so:

$$-J_n(x+\Delta x) = -J_n(x) + q[G(x) - U(x)] \quad \text{3-9}$$

If the size of the interval, Δx, is infinitesimally small, equation 3-9 represents the integral form of the continuity equation.

The transport equation is used to determine the carrier density from the electron current.

$$J_n(x) = J - J_p(x) \quad \text{3-10}$$

In general, the current is composed by a diffusion term and a drift component. However, both can be represented with an effective diffusion coefficient, D_{eff}, as below [77]:

$$J_n(x) = qD_{eff}\frac{dn}{dx} + J\frac{nD_n}{nD_n + pD_p} \; where \; D_{eff} = \frac{(n+p)D_pD_n}{nD_n + pD_p} \quad \text{3-11}$$

so, it can be implied that:

$$\Delta n(x+\Delta x) = \Delta n\,(x) + \frac{J_n(x)}{q\,D_{eff}}\Delta x - \frac{J}{q\,D_{eff}}\frac{n\,D_n}{n\,D_n + p\,D_p}\Delta x \quad \text{3-12}$$

where the effective diffusion coefficient, described in detail in [77], is defined as:

$$D_{eff} = kT\,q\mu_n\,\mu_p\left(\frac{(n_0+\Delta n)+(p_0+\Delta n)}{\mu_n(n_0+\Delta n)+\mu_p(p_0+\Delta n)}\right) \quad \text{3-13}$$

with *k* is the Boltzmann constant and *T* is the temperature.

As there is no output current in ingot measurements, $J = 0$, the last element of equation 3-12 is eliminated in the calculations, and so:

$$\Delta n(x+\Delta x) = \Delta n\,(x) + \frac{J_n(x)}{qD_{eff}}\Delta x \quad \text{3-14}$$

The numerical analysis then uses equation 3-14 to simulate the minority carrier density profile. The analysis involves equating the generation and recombination rates across the entire sample, including the diffusion of carriers into and out of the elements.

For the boundary conditions at the surface (at $x = 0$):

$$J_n(0) = \left[\frac{\Delta n(0) q n_i^2}{\Delta n(0)[N_A + \Delta n(0)]} \right] SRV \qquad 3\text{-}15$$

where $J_n(0)$ and $\Delta n(0)$ are the current density and the excess carrier density at the surface, respectively. N_A is the sample doping, and *SRV* is the Surface Recombination Velocity which is assumed to be $10^6\ \mathrm{cms}^{-1}$ [79, 80] in all simulations presented in this thesis. As the sample thickness is assumed to be significantly larger than the diffusion length, the back surface of the sample has no impact on the calculation and so, there is no boundary condition imposed from the back surface.

The unpassivated surface of an as-cut sample introduces a very high *SRV* due to its numerous defect levels within the material bandgap acting as significantly active recombination centres. Thus, there is a large deviation in the measured effective lifetime from the actual bulk lifetime in the QSSPC lifetime measurement induced by the high *SRV*. Therefore, a transfer function is employed to eliminate the impact of high *SRV* providing an adequately accurate estimation of the actual bulk lifetime. However, the simulation results in this chapter only include the effective lifetime and the estimated lifetime results will be shown in next chapters. There are also other sources of uncertainties which should be considered during the determination of the transfer function that will be discussed further in the coming sections.

The numerical analysis starts its iteration with an initial guess for $\Delta n(0)$ and solves the continuity equations 3-9 and transport equation 3-14 to determine the carrier density profile, Δn,

across the sample thickness. Then, the calculated carrier density profile is used to determine the total recombination across the sample thickness at the end of every iteration. The loop is continuously performed until the calculated carrier density profile results in a total recombination value equal to the total photogeneration in the sample (U=G).

3.2.2.1 Recombination processes

In order to find the total recombination rate in the sample to equate it with the total generation, as mentioned in the previous chapter, recombination processes in the bulk and surface are taken into account to determine the excess carrier effective lifetime (equation 2-16).

The intrinsic recombination consists of the radiative recombination and the Auger recombination as mentioned before.

$$U_{intrinsic} = U_{rad} + U_{Auger} \qquad 3\text{-}16$$

The model accepts arbitrary dopant densities N_A and N_D as inputs which then calculate the appropriate intrinsic lifetimes at each depth interval, Δx, and the injection level, Δn, within it. The intrinsic lifetime in this thesis is calculated using the intrinsic recombination model from Richter *et al.* [30] when doping is less than 6×10^{16} cm^{-3} and can be represented as:

$$\tau_{intrinsic} = \frac{\Delta n}{np(8.7 \times 10^{-29} n_0^{0.91} + 6 \times 10^{-30} p_0^{0.94} + 3 \times 10^{-29} \Delta n^{0.92} + 4.73 \times 10^{-15})} \qquad 3\text{-}17$$

where the effect of the various enhancement process for both radiative and Auger recombination are quantified by the term in brackets [30, 81].

The lifetime due to Shockley-Read-Hall recombination in the bulk material is calculated from equation 2-11. Each impurity introduces a distinctive defect level within the silicon bandgap which

is characterised by its capture cross sections along with the defect (impurity) density, that are used to determine the carrier lifetime imposed by each impurity at each depth.

The last component of equation 2-16, τ_{other}, is a manually-input variable which represents all other recombination like recombination at internal interfaces such as grain boundaries, GBs, in multicrystalline samples. It is a convenient method for allowing background SRH bulk recombination to be included in the modelling, when studying specific impurities such as iron (Fe).

3.2.2.2 Total recombination

The final step to determine the total recombination is to calculate the recombination current at each Δx as:

$$J_r(x + \Delta x) = q\ \Delta n\ (x)\ \Delta x \left(\frac{1}{\tau_{int}} + \frac{1}{\tau_{SRH-bulk}} + \frac{1}{\tau_{other}}\right) \qquad 3\text{-}18$$

At the end of each iteration in the loop, the total recombination rate is compared to the total generation rate across the sample thickness, and the loop stops when they are perfectly balanced.

Figure 3-4 shows the carrier density profile for quasi-steady state conditions under the illumination with the same light source (RG1000), as figure 3-2, in the first 1 cm of a thick boron-doped silicon crystalline sample with the bulk lifetime (τ_{bulk}) of 50 µs, N_A= 10^{16} cm^{-3} and surface recombination velocity of 10^6 cms^{-1}. As shown here, and as will be discussed in the next section, the carrier density profile is not uniform across the sample thickness in semi-infinite samples. Therefore, an arithmetic mean of total excess carriers is not an appropriate representation of injection levels within the sample [11].

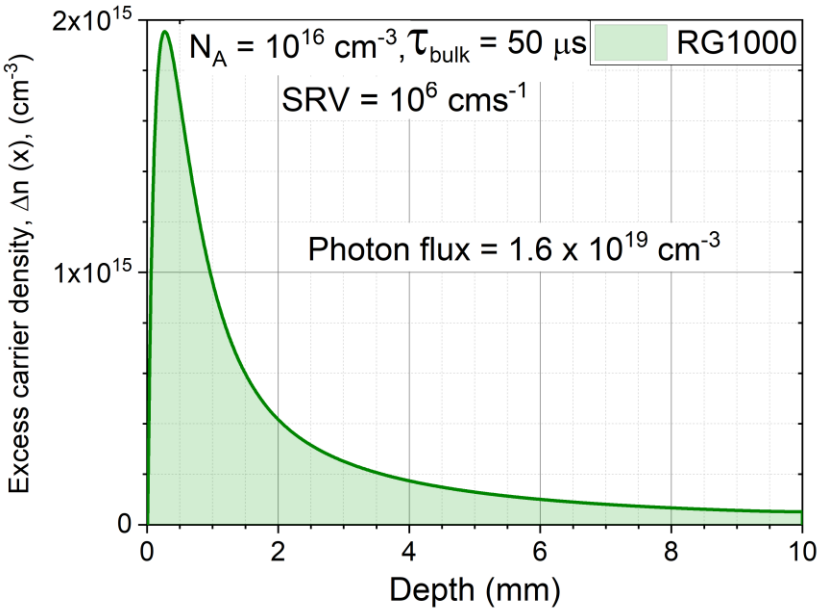

Figure 3-4: The excess carrier density profile (Δn) as a function of depth for a boron-doped crystalline silicon sample with the dopant density of 10^{16} cm^{-3} and minority carrier bulk lifetime of 50 µs (the same light source as figure 3-2) and SRV = 10^6 cms^{-1}.

It should be noted here, as illustrated in figure 3-2 and figure 3-4, that the generation and carrier densities are significantly lower for the deeper part of samples like ingots and blocks (depth > 4 mm) in comparison with the shallower parts. In these deep regions, the difference between $\Delta n(x + \Delta x)$ and $\Delta n(x)$ becomes very small, and, consequently, the evaluation of equation 3-14 became a slow and ineffective process. In order to address this issue, the depth interval, Δx, is enlarged continuously in the deeper parts of the sample which significantly improves the simulation performance and speed to equate total generation and recombination in thick samples.

3.2.3 Effective lifetime

As illustrated in figure 3-2 and mentioned in section 3.2.1, the generation of carriers is confined to the first few millimetres of the block, even for high lifetime materials [11]. In contrast with regular 200-300 µm thick wafers in which the surface is passivated and, thus, have very steady

carrier densities across the sample, the Δn profile in a block is never uniform [10]. Hence, replacing an arithmetic average of Δn_{total} into equation 3-1 is not appropriate to determine the effective lifetime for thick as-cut samples as it is for passivated wafers.

The determination of injection levels during the QSSPC measurements is a significant challenge when the technique is applied to semi-infinite samples. A weighted average excess carrier density, Δn_{avg}, was proposed by Bowden and Sinton [11] to address this problem, which is a weighted average carrier concentration replacing the injection levels as:

$$\Delta n_{avg} = \frac{\int_0^\infty \Delta n^2 dx}{\int_0^\infty \Delta n dx} \qquad 3\text{-}19$$

The weighted average considers only the sections of the sample that have a light-induced excess carrier concentration. Consequently, the deeper parts of the sample that have no excess carriers are automatically discarded from the analysis [11]. A new definition of an effective thickness was also proposed [11] to represent the width of the region with the high carrier densities as the total generated excess carrier concentration, Δn_{total}, divided by the defined Δn_{avg} as:

$$W_{eff} = \frac{\int_0^\infty \Delta n dx}{\Delta n_{avg}} = \frac{\left(\int_0^\infty \Delta n dx\right)^2}{\int_0^\infty \Delta n^2 dx} \qquad 3\text{-}20$$

The average excess carrier concentration and the sample effective thickness are then used to calculate the effective lifetime from equation 3-1:

$$\tau_{eff} = \frac{\Delta n_{avg}\, W_{eff}}{g_{cum}} \qquad 3\text{-}21$$

The arithmetic-mean of Δn_{total} vs. Δn_{avg} as well as sample effective thickness are illustrated in figure 3-5. As the new parameters show, the average excess carrier density, Δn_{avg}, is about four times larger than the arithmetic-mean of the total excess carrier density. It also illustrates that the majority of the photogenerated excess carriers are confined in the first 2 mm of the bulk, and the rest of the sample thickness has negligible impact on the calculation for accurate effective lifetime determination.

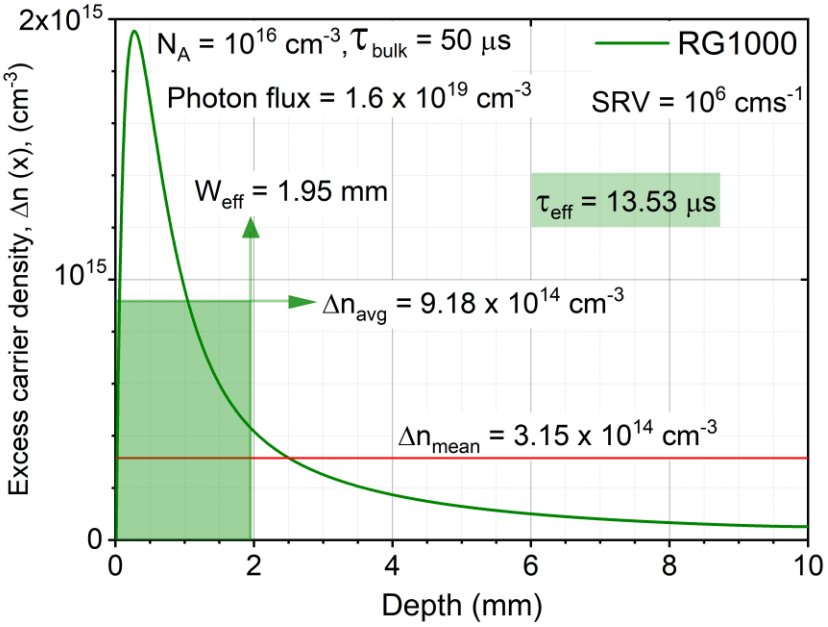

Figure 3-5: Calculated effective lifetime (τ_{eff}) from equation 3-21, effective thickness (W_{eff}), average carrier density (Δn_{avg}) and arithmatic-mean carrier density (Δn_{mean}) for the sample in figure 3-4.

As discussed in the second chapter, the surface recombination velocity of unpassivated surfaces severely affects the effective lifetime, τ_{eff}, causing a large deviation from the actual sample bulk lifetime, τ_{bulk}. The deviation is clearly presented in figure 3-5 where the bulk lifetime of 50 µs was determined as τ_{eff}= 13.53 µs. Hence, a transfer function must be determined to estimate the bulk lifetime according to the effective lifetime which is discussed in detail in the next section.

One of the most important advantages of the photoconductance measurement on the block is its fast and uncomplicated method of characterisation. Accordingly, Sinton BCT-400 boule tester which is used in this thesis to conduct the measurements is equipped with a xenon flash as the source of photogeneration. A 1000-nm IR-Pass Schott glass filter is inserted in front of the light source to eliminate the short wavelength light from the incident light. As discussed, the short wavelengths elimination is important as the lower absorption coefficients of the longer wavelength light cause a deeper excess carrier generation profiles in the sample bulk. The most important advantage of this deep photogeneration is being distant from the surface with the high SRV. Subsequently, more excess carriers recombine in the bulk material before they diffuse into the surface and recombine there. The reduction in recombination at the unpassivated surface results in a higher contribution of the bulk recombination to the effective lifetime. Hence, the effective lifetime has less deviation from the actual bulk lifetime resulting in much more accurate characterisation.

A rectangular RF conductive coil is used in a Sinton BCT-400 to monitor changes in sample conductivity during the illumination when the lifetime measurements are being performed. The large sample thickness includes distant areas from the conductive coil and, therefore, the detected conductivity values from those areas are less than their actual conductivity. To address this issue, Swirhun *et al*.[80] comprehensively studied the depth sensitivity of the conductive coil used in the tool. As the conductivity and excess carrier density are linearly related [80], the detected excess densities, $\Delta n_{sensed}(x)$, from the depth *x*, were found to be:

$$\Delta n_{sensed}(x) = \Delta n_{actual}(x) e^{-x/x_{sensed}} \qquad 3\text{-}22$$

where the x_{sensed} is measured as 2.5 mm for Sinton BCT-400 [80]. This relationship is instrument-dependent and the x_{sensed} can be determined for any instruments.

The modified effective thickness is defined to incorporate the coil depth sensitivity into measurements as the average excess carrier density divided by total sensed carrier density [80]:

$$W_{sensed-eff} = \frac{\int_0^{\infty} \Delta n_{sensed} dx}{\Delta n_{avg}} \quad 3\text{-}23$$

The importance of this modification is to accurately simulate the measurement and evaluate the accuracy of the silicon characterisation performed by Sinton BCT-400. Thus, the effective lifetime measured by the instrument is determined as:

$$\tau_{eff} = \frac{\Delta n_{avg}\, W_{sensed-eff}}{g_{cum}} \quad 3\text{-}24$$

The impact of the coil sensitivity as a function of depth is illustrated in figure 3-6. As can be seen, the difference between the actual excess carrier densities (solid line) and the sensed carrier densities (dashed line) increase moving away from the sensor towards the deeper parts of the bulk. Figure 3-6 also shows the change in the effective thickness value when the total sensed carrier densities (Δn_{sensed}) is used to determine the sensed effective thickness, $W_{sensed-eff}$.

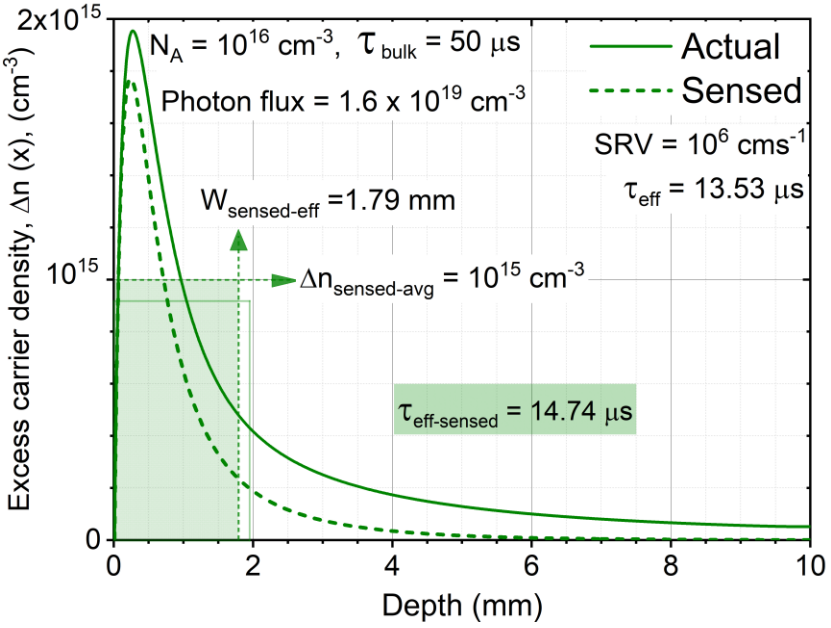

Figure 3-6: The actual vs sensed values of calculated effective lifetime, effective thickness, average carrier density after applying the RF coil depth sensitivity function to the simulation results.

As shown in figure 3-5 and figure 3-6, due to the high surface recombination velocity of an as-cut sample, the effective measured lifetime is significantly lower than the actual bulk lifetime. Such a large deviation in the effective lifetime from the actual bulk lifetime is because the dominance of the surface recombination to the bulk recombination as expected from equation 2-14. Hence, a transfer function is always needed to remove the effect of surface recombination velocity and estimate the bulk lifetime ($\tau_{effective} \rightarrow \tau_{QSS-bulk}$) based on the measured effective lifetime. Such a transfer function provides the most accurate results at a specific injection level at which lifetime measurement simulations are performed.

3.2.4 Simulation depth

The typical simulation depths in the simulations in this thesis has been 1 cm due to the limits on conductive sensor depth sensitivity [80] as well as the fact that most excess carriers are generated just below the surface. To ensure the simulation is sufficiently deep to include all

influential parameters on the lifetime measurements, a qualitative demonstration is needed to confirm the conservative assumption for simulation depth.

The carrier density profiles generated by the RG1000 filter for various depths are simulated in this section to evaluate the impact of simulation depth on the accuracy of lifetime measurement simulations in semi-infinite silicon samples.

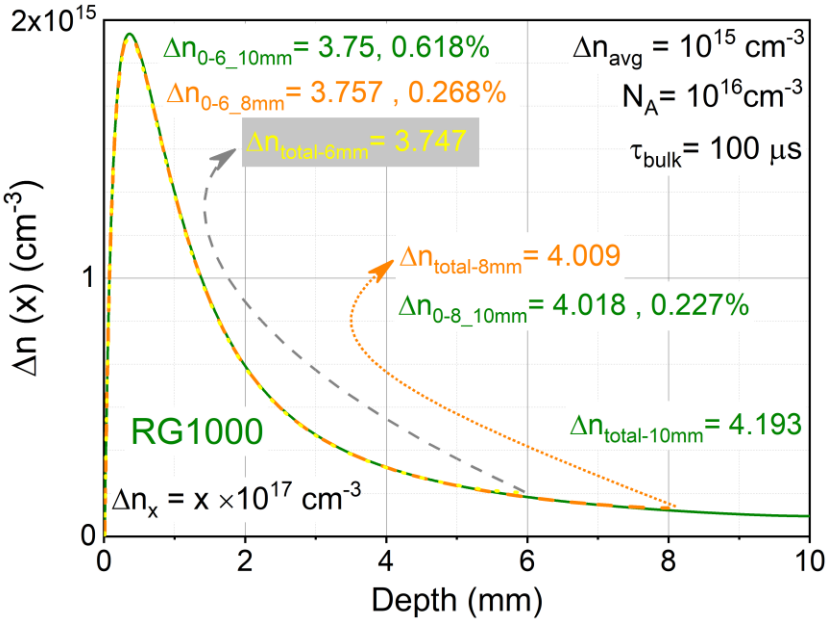

Figure 3-7: Carrier density profile generated with RG1000 for 6, 8 and 10 mm simulation depth of a sample with 10^{16} cm^{-3} dopant density and 100µs bulk lifetime. The total excess carriers in the first 6 mm of 8 and 10 mm are respectively 0.62% and 0.27% higher than the total excess carriers when the simulation depth is 6mm. However, the difference dropped to 0.23% between the first 8 mm of 10 mm simulation depth and the 8 mm simulation depth.

As figure 3-7 shows, total generated excess carriers in the first 6 mm of 8 mm and 10 mm simulation depths are respectively 0.62% and 0.27% higher than the case when the simulation depth is 6 mm. The difference between the first 8 mm when the simulation depth is 10 mm and the simulation depth of 8 mm dropped to 0.23%. In addition, due to the typical silicon blocks and ingots thicknesses, the back-surface reflection and carrier regeneration are negligible. Therefore,

1 cm simulation depth is a conservative assumption which considers all phenomena that can influence the lifetime measurements.

3.3 Transient decay PhotoConductance lifetime measurement

As mentioned in section 3.2.1, the QSS lifetime measurement results are not accurate in the long lifetime ranges (τ_{bulk} > 150 µs) due to dynamic changes in excess carrier densities during the flash decay that are not considered for the QSS approximation [7, 8]. In contrast, the transient mode of photoconductance lifetime measurements cannot be used in the low lifetime range where the sample bulk lifetime is not long in comparison with the light source decay constant. Therefore, transient measurements are the appropriate method to apply for bulk lifetimes in the range above 150 µs [10].

3.3.1 Initial excess carriers

Lifetime measurements in transient conditions of equation 3-8 is performed when the excess carrier concentration decays over the time ($\frac{\partial n(x,t)}{\partial t} \neq 0$) in the absence of photogeneration ($G(x,t) = 0$). Therefore, the sample needs to be initially illuminated to quasi-steady state conditions and, subsequently, the light source (photogeneration) is terminated at $t = 0$. The excess carrier transient lifetime, $\tau_{transient}$, is then determined from the rate at which the excess carrier densities profile decays.

The simulation is based on a finite elements approach, with the depth and time intervals Δx and Δt chosen to be small enough to ensure the local changes in the excess carrier density are approximately linear in x and t. The excess carrier density within each depth interval, Δx, constantly changes over time ($\frac{d\Delta n(t)}{dt} \neq 0$) as there is no photogeneration. The changes are not

only because of the recombination within an element, Δx, but also because of carrier diffusion to and from the adjacent depth intervals in the absence of constant charge carrier injection.

$$-J_n(x,t) = J_{n-r}(x,t) + J_{n-dif}(x,t) \qquad 3\text{-}25$$

The recombination element of the current, $J_{n\text{-}r}(x,t)$, is similarly calculated from equation 3-18 as in the QSS mode where different recombination mechanisms influence the recombination current densities. However, the diffusion component at a given depth, x, needs to be determined according to the differences in the excess carrier densities between the adjacent depth interval before, $(x - \Delta x)$, and after, $(x + \Delta x)$, x from:

$$J_{n-dif}(x, t+\Delta t) = D_{eff}\frac{\Delta t}{\Delta x^2}(\Delta n(x+\Delta x, t+\Delta t) - 2\Delta n(x, t+\Delta t) + \Delta n(x-\Delta x, t+\Delta t) \qquad 3\text{-}26$$

To ensure equation 3-26 is a valid equation to calculate the diffusion current, Δt has to be significantly shorter than the lifetime (order of 10 ns) such that the carrier recombination impact in changing the excess carrier concentrations within the depth interval is negligible during that time interval (Δt).

3.3.2 Transient carrier density decay

Figure 3-8 shows the excess carrier density profiles as a function of depth at various elapsed times after turning the light source off. The results are for a case of p-type silicon with a bulk lifetime of 300 μs.

As can be seen, in the absence of photogeneration, the peak of the excess carrier density profiles moves deeper into the bulk as time elapses after eliminating the light source. Therefore, the high SRV of the as-cut unpassivated surface impact on the calculated lifetime reduces over time and, consequently, the transient lifetime is expected to become closer to the actual bulk lifetime [78].

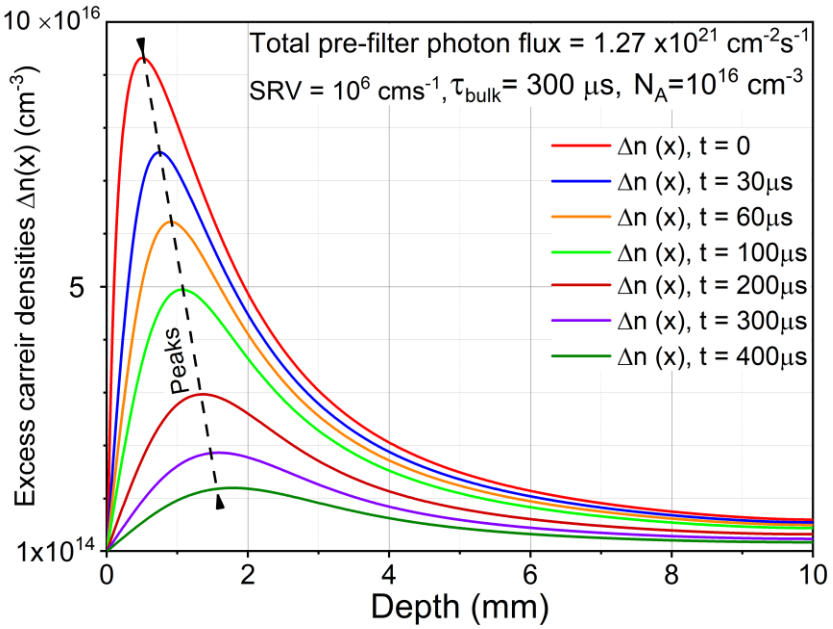

Figure 3-8: Excess carrier density profile as a function of sample depth at various elapsed times after turning the light source off for a boron-doped crystalline silicon sample with bulk lifetime of 300 μs, dopant density of 10^{16} cm^{-3} and SRV = 10^6 cms^{-1}.

As expected from carrier density profiles in figure 3-8, the weighted average minority carrier density profiles decrease as the function of time, $\Delta n_{avg}(t)$, after terminating the illumination source. The continuous decay of the weighted average minority carrier density, $\Delta n_{avg}(t)$, in figure 3-8 over time after illumination was terminated is illustrated in figure 3-9. The tangent of the weighted average minority carrier profiles decay at a given time with corresponding injection level is inversely related to the transient lifetime, $\tau_{transient}$, at a specific injection level as:

$$\tau_{transient} = \frac{\Delta n_{avg}}{-\left(\frac{d\Delta n_{avg}(t)}{dt}\right)} = \frac{\Delta n_{avg}\, \Delta t}{\Delta n_{avg}(t) - \Delta n_{avg}(t + \Delta t)} \qquad 3\text{-}27$$

As shown in figure 3-9, the $\Delta n_{avg}(t)$ tangent decreases over time meaning that the measured transient lifetime, $\tau_{transient}$, is increasing as time elapses after eliminating the light source, confirming the expectation of reduced impact of the high SRV over time in figure 3-8.

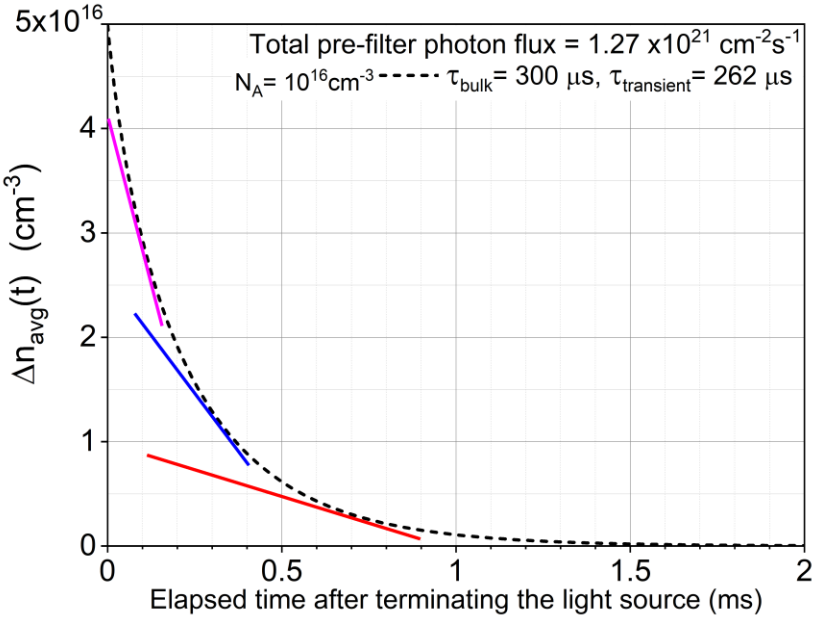

Figure 3-9: The rate at which $\Delta n_{avg}(t)$ decays (the tangent of the average carrier densities as a function of time) decreases over time resulting in an increasing measured transient lifetime, $\tau_{transient}$, as time elapsed after the light source is terminated.

Figure 3-10 shows the continuous decay of the weighted average minority carrier density, $\Delta n_{avg}(t)$, over time after illumination was terminated for various bulk lifetimes. The injection level (10^{15} cm^{-3}) at which the transient lifetimes, $\tau_{transient}$, are determined is indicated with a dashed line.

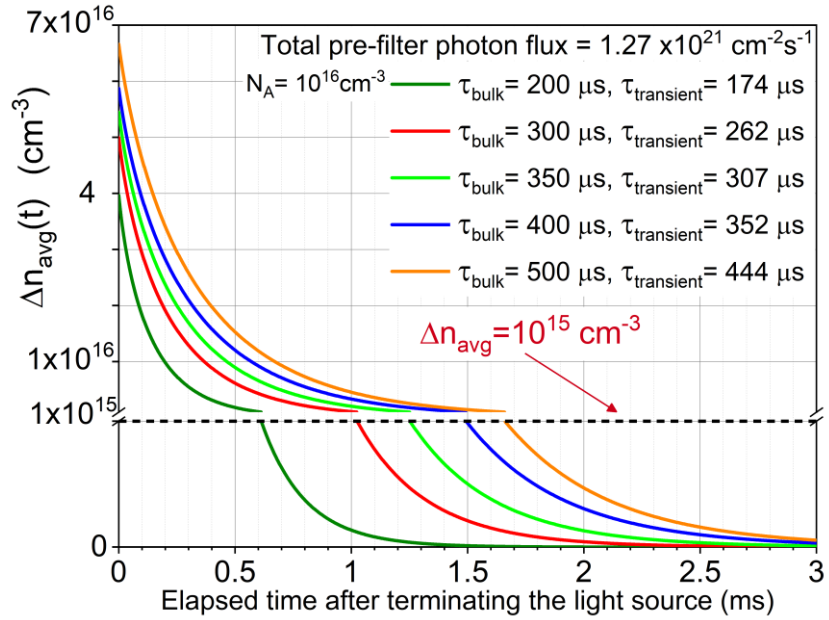

Figure 3-10: Simulated weighted injection level (Δn_{avg}) decay as a function of elapsed time for different bulk lifetime values. The dashed line intercepts with the curves indicate when the injection level has decayed to 10^{15} cm^{-3} where the slope is calculated to determine the transient lifetime. Simulations were performed assuming a standard RG1000 filter.

3.4 Summary

This chapter explained a model in detail to simulate photoconductance minority carrier lifetime measurements in the QSS and transient modes. The biggest challenge in the lifetime measurements of semi-infinite thick samples is the non-uniform excess carrier density in the sample which is addressed by introducing a weighted average density, Δn_{avg}, and an effective thickness, W_{eff}. The largest deviation in the measured effective lifetime, τ_{eff}, and the transient lifetime, $\tau_{transient}$, from the actual bulk lifetime, τ_{Bulk}, in the sample is due to the high surface recombination velocity introduced by the unpassivated sample surface.

A transfer function was introduced to estimate the bulk lifetime, $\tau_{QSS-bulk}$, corresponding to the measured effective lifetime, τ_{eff}, in the QSS mode. The transfer function aims mainly to eliminate the impact of high surface recombination velocity on effective lifetime. However, it reduces the uncertainties that variables like the average carrier density, Δn_{avg}, and the effective thickness, W_{eff}, may impose on lifetime measurements.

Transient measurements, however, have less complexity as there is no need to determine the total photogeneration rate in the sample, as is required in QSS. The measured lifetime is closer to the actual bulk lifetime if a longer time has elapsed after terminating the light source to reduce the effect of the surface recombination velocity.

More details about the effect of different factors on the measurement accuracy will be explained in chapter 5 and chapter 6 when the improvement of both techniques are discussed by using new filters.

Chapter 4: Determination of Interstitial Iron Concentration in mc-Si p-type Blocks

4.1 Introduction

As discussed earlier in the second chapter, Shockley-Read-Hall (SRH) recombination due to material impurities is the most influential recombination on carrier lifetimes (figure 2-2), particularly in low to medium quality materials such as multicrystalline silicon. Limiting minority carrier lifetime decreases the probability of generated carriers to be collected by cell contacts and, hence, results in the reduction of a solar cells conversion efficiency. Therefore, impurity identification is one of the most important purposes of material and device characterisation in silicon photovoltaic solar cells.

In this chapter, the source of impurities and their impact on silicon properties are discussed briefly. Then, the focus is on the determination of iron in p-type crystalline silicon as a very common impurity in silicon photovoltaics which degrades the performance of solar cells. The simulation tool introduced in the third chapter is employed to model the determination of the interstitial iron concentration in mc-silicon blocks and investigate the accuracy of its determination on such a sample.

4.2 Source of impurities and their impacts on silicon properties

Different crystallisation techniques are used to produce silicon ingots. The presence of impurities, such as carbon, oxygen, aluminium, copper, transition metals, etc depends on the technique used to produce silicon. These impurity sources can be the impurities in the feedstock used in the technique itself as well as the equipment used in each process to grow the crystals. Al,

C, O and transition metals are introduced to silicon from the crucible during Czochralski growth. The same impurities plus nitrogen, N, from the crucible coating layer (Si_3N_4) are introduced into the silicon ingot growth by directional multicrystalline solidification [49]. Hot-zone parts are also common sources of impurities in the ribbon method, directional crystallisation, as well as Czochralski technique.

The presence of impurities as external elements in the crystalline structure can result in point defects (substitutional or interstitial) or precipitated elements in silicon lattice structures. Their chemical states and distribution patterns within the silicon crystal structure depends on their solubility and diffusivity which are the signature properties of each element. Impurities atomic sizes and chemical affinity in silicon lattice determine this solubility and diffusivity. The presence of these foreign elements introduce defect energy levels within the silicon bandgap structure which were explained before as SRH recombination centres and severely impact minority carrier lifetime [49]. In addition to the impurities introduced in silicon during the crystallisation techniques, new impurities are also introduced during solar cell manufacturing processes. Solar cell fabrication processes can also affect the existing impurities via thermal changes or chemical reactions to improve or degrade device performances [82]. Therefore, defect engineering where some steps are integrated into the fabrication process is needed to improve cell performance and stability for final cell efficiency.

Iron is one of the most important and common impurities in silicon material particularly because of its frequent use in the construction of equipment components in the crystal growth industry [21]. Due to the high chemical affinity of iron to bond with doping atoms, iron plays an influential role in the properties of p-type, particularly in boron-doped multicrystalline silicon. The presence of iron atoms, even at very low concentrations, in silicon lattice structure limits the carrier lifetime

drastically due to SRH recombination [22]. Such a reduction in carrier lifetime decreases different cell parameters such as short-circuit current, I_{sc}, and open-circuit voltage, V_{oc}, which directly degrade solar cell performance [83-85].

4.3 Determination of iron concentration in boron-doped Si

As mentioned above, the common form of the iron impurity in boron-doped p-type silicon material under the equilibrium conditions is iron-boron (FeB) pairs. Dissociation of the iron-boron pairs by either thermal annealing or illumination introduces iron atoms in the interstitial form, Fe_i, to the silicon structure. Each form (FeB or Fe_i) introduces its signature energy levels within the silicon bandgap as well as having their unique capture cross sections causing their distinctive recombination properties [22]. Hence, dissociation of iron-boron pairs drastically changes the nonequilibrium carrier diffusion lengths/lifetimes and, therefore, a sensitive way to measure the interstitial iron concentrations in silicon material is to employ carrier lifetime measurements techniques (or diffusion lengths measurements as discussed in the second chapter).

As shown in many studies before, the accuracy of the lifetime measurements on unpassivated surface samples depends on several factors [65, 79, 86]. Particularly the impact of a high surface recombination velocity which introduces large deviations between the measured and actual bulk lifetime [11, 12, 15].

Zoth and Bergholz [21] showed that if all other recombination centres remain the same during the dissociation, the total iron concentration in the boron-doped p-type silicon wafer can be determined by:

$$[Fe_i] = A\left(\frac{1}{L_1^2} - \frac{1}{L_0^2}\right) = C\left(\frac{1}{\tau_1} - \frac{1}{\tau_0}\right) \qquad 4\text{-}1$$

For $N_A = 1 - 3 \times 10^{15}\ \mathrm{cm}^{-3}$, where the empirical value of A was determined as $1.06 \times 10^{16}\ \mu\mathrm{m}^2\ \mathrm{cm}^{-3}$, and L_0 and $L_1$are the low-injection carrier diffusion lengths before and after dissociation of iron-boron pairs, respectively. As shown in equation 4-1, replacing coefficient A with $A = D_nC$ (where D_n is minority carrier, electron, diffusion coefficient) [22] allows using minority carrier lifetimes (τ_1 and τ_0) at low-injection levels to determine interstitial iron concentration.

Due to the pre-assumptions on injection levels, photoconductance measurement techniques are not suitable to determine the carrier lifetimes before and after iron-boron pairs dissociation at low-injection levels. This is because photoconductance techniques are often suffering from the minority carrier trapping effect at low-injection levels which introduces large inaccuracy to measurement results. Hence, with the cost of much less convenient than photoconductance techniques, voltage-based lifetime measurement techniques such as surface photovoltage (SPV) or luminescence-based such as photoluminescence intensity ratio are preferable to be used at low-injection levels [22]. Moreover, the restrictions on material doping ($1 - 3 \times 10^{16}\ \mathrm{cm}^{-3}$) limit the application of the method to resistivity range above 5 Ωcm. However, solar grade boron-doped multicrystalline silicon wafers that are widely used for solar cell manufacturing these days (~ 1 Ωcm) are excluded from such a range.

Macdonald *et al.* [22] addressed the above issues by using the known recombination parameters of FeB pairs and Fe_i to determine the coefficient C for any desired injection level and a broad range of dopant densities from 10^{14} to $10^{16}\ \mathrm{cm}^{-3}$. Their work greatly extended the application of the method proposed by Zoth and Bergholz to broad ranges of doping and injection levels in silicon wafers for photovoltaic applications. It should be noted here that knowing the proportion of Fe

present as FeB pairs is a critically important factor during the measurements before and after dissociation. Macdonald *et al.* [22] demonstrated that dissociation by a strong illumination would break more than 99% of the existing iron-boron pairs in the silicon sample which is adequately accurate to be used for determination of interstitial iron concentration. They also showed that leaving the sample in a dark environment for at least 24 hours is sufficient for an almost complete re-pairing for typical dopant densities.

Here in this chapter, the determined *C* value for equation 4-1 is used to determine the interstitial iron concentration in a multicrystalline p-type silicon block by measuring the carrier lifetime before and after dissociation using the quasi-steady state photoconductance technique.

4.4 Simulation

The simulation tool introduced in the third chapter is employed here to evaluate the accuracy of interstitial iron concentration in multicrystalline p-type silicon block. The carrier lifetimes before and after iron-boron pairs dissociation are resulted from the Sinton BCT-400 transfer function applied to the calculated lifetimes from 3-24. Then, the extended form of the method in 4-1 is used with the coefficient *C* determined by Macdonald *et al.* in [22] to determine interstitial iron concentration.

4.4.1 Inaccuracy in the determination of $[Fe_i]$

Figure 4-1 shows the simulation results of QSS-bulk lifetimes as a function of injection level for a 10^{16} cm^{-3} boron-doped p-type silicon block with 10^{11} cm^{-3} iron contamination. The $\tau_{other}$was selected to be 1 ms to ensure that Shockley Read Hall recombination due to dissolved iron contamination is the dominant recombination mechanism in the sample. As indicated, the crossover point is just above 10^{14} cm^{-3} as reported in the literature which is observed in typical

lifetime versus injection level data measured on wafers [22, 87]. In principle, the impact of diffusion currents resulting from the non-uniform carrier densities, and the approximation in definition of the effective thickness (W_{eff}) and average excess carrier density (Δn_{avg}) may vary the position of the crossover point of a block measurement [10].

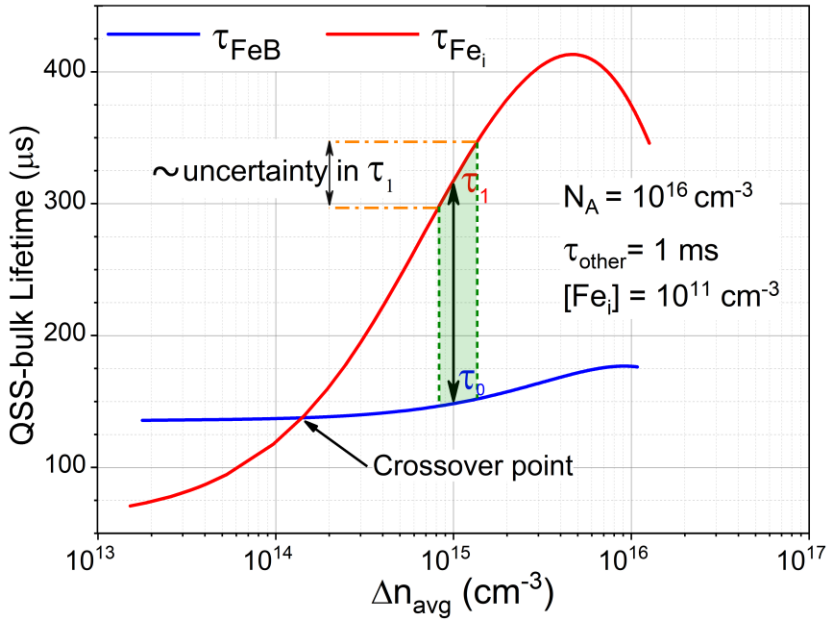

Figure 4-1: Simulated extracted QSS-bulk lifetime ($\tau_{QSS-bulk}$) as a function of the average excess carrier density (Δn_{avg}) before (τ_{FeB}) and after (τ_{Fe_i}) breaking the Fe–B pairs: the crossover point is located at an excess carrier density just above 10^{14} cm^{-3}. The approximate uncertainty in the τ_1 (τ_{Fe_i} at $\Delta n_{avg} = 10^{15}$ cm^{-3}) is shown only for illustration to emphasise that $\Delta n_{avg} = 10^{15}$ cm^{-3} does not mean $\Delta n = 10^{15}$ cm^{-3} at every *x* as shown in figure 3-4.

As can be seen in figure 4-1, the carrier lifetime as a function of injection level for Fe_i has a steep slope around $\Delta n_{avg} = 10^{15}$ cm^{-3} where QSSPC is usually performed. Therefore, a small uncertainty in injection level, Δn, leads to a large error in τ_1 resulting in inaccurate determinations of interstitial iron concentrations. Since the Δn is never uniform across thick samples and the

defined Δn_{avg} is used to approximate the injection level in the sample, errors are to be expected when using 4-1 for determination of dissolved iron concentration on p-type silicon blocks [10].

As mentioned in the chapter 3, the densities of common impurities in solar grade silicon materials like iron are accepted as input variables in the simulation tool. For a given input iron concentration, the QSS-bulk lifetimes are determined by running simulations before and after dissociating the iron-boron pairs. Then, both lifetimes are used in equation 4-1 to determine the calculated iron concentration using the method extended by Macdonald *et al.* [22]. The error introduced by the method is defined as:

$$Error = \frac{[Fe_i]_{calculated} - [Fe_i]_{actual}}{[Fe_i]_{calculated}} \qquad 4\text{-}2$$

where $[Fe_i]_{actual}$ and $[Fe_i]_{calculated}$ are the simulation input iron concentration and the calculated interstitial iron concentration applying τ_1 and τ_0 from the simulation results in 4-1 respectively.

In the following sections, the impacts of different factors on the accuracy of determination of interstitial iron concentrations, $[Fe_i]$, in a multicrystalline boron-doped silicon block are investigated. These factors are injection levels, Δn_{avg}, at which the measurement is performed, boron doping concentration, N_A, iron concentration, $[Fe_i]$, itself as well as τ_{other}. To do so, simulations are performed for a given iron concentration for several values of one of the factors mentioned above while the others remained unchanged. The simulations are repeated with different iron concentration, and errors are calculated for each case scenario to evaluate the accuracy of the method at the ingot level.

4.4.1.1 Impact of iron concentration

To evaluate the accuracy of determining the interstitial iron concentration, the concentration of iron impurity itself in a multicrystalline p-type silicon sample is the first factor investigated here using the mentioned method. The error in the determination of interstitial iron concentration as a function of dissolved iron concentration in a boron-doped silicon block with τ_{other} = 300 µs is shown in figure 4-2 . In this figure the lifetimes before and after dissociation of iron-boron pairs are simulated at $\Delta n_{avg} = 10^{15}$ cm^{-3}. The reason for choosing relatively low τ_{other}(300 µs) is to compare the cases where the iron impurity is the dominant recombination mechanism ($[Fe_i]$ > 10^{11} cm^{-3}) against the cases that other extrinsic mechanisms are dominant ($[Fe_i]$ <10^{11} cm^{-3}).

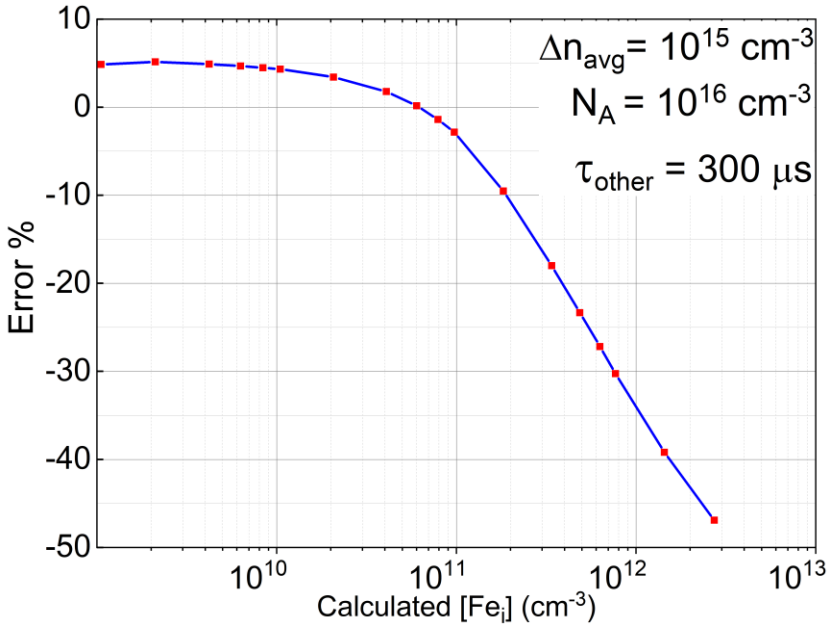

Figure 4-2: Effect of interstitial iron concentration on the $[Fe_i]$ calculation error for a boron-doped crystalline silicon sample with dopant density of 10^{16} cm^{-3} and SRV =10^{6} cms^{-1}, when the QSS-bulk lifetime simulated at $\Delta n_{avg} = 10^{15}$ cm^{-3}.

The results show a slight overestimation of interstitial iron concentrations when the iron impurity is not the dominant recombination centre in bulk ($[Fe_i]$ <10^{11} cm^{-3}). The calculation

error changes by only around 10% over the one and half orders of magnitude increase in dissolved iron concentration to around 6×10^{10} cm^{-3}. By contrast, when iron impurity becomes the dominant recombination mechanism in the bulk ($[Fe_i]$ >10^{11} cm^{-3}), there is an underestimation of the interstitial iron concentration which rises drastically with the increasing iron impurity concentration. As can be seen in figure 4-2, one and a half orders of magnitude increase in iron concentration (to 2×10^{12} cm^{-3}) causes a 50% changes in the error (almost five times more than the low iron concentration range) in this highly iron contaminated range [10].

4.4.1.2 Impact of injection level, Δn_{avg}

The injection level at which the lifetime measurements are performed also impacts the accuracy of dissolved iron concentration determination. To investigate this effect, several lifetime simulations at different injection levels are performed before and after breaking iron-boron bonds in multicrystalline p-type silicon with various iron concentrations.

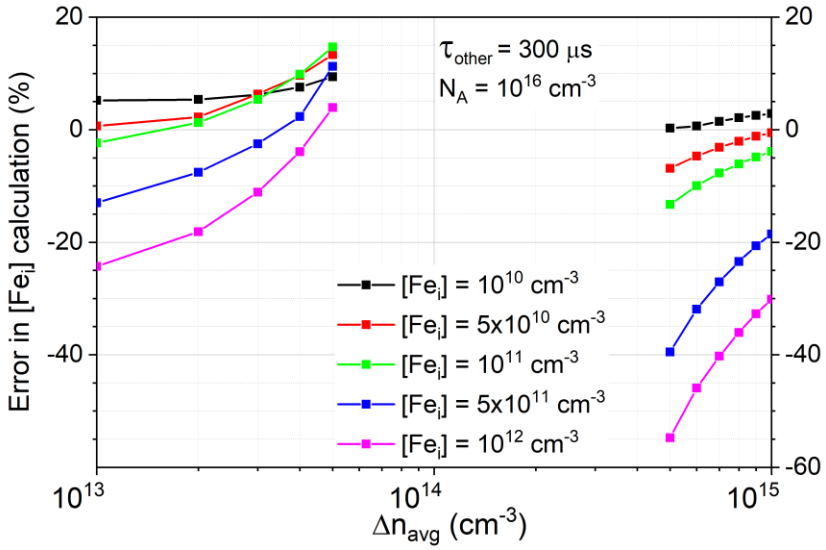

Figure 4-3: Effect of injection level on the $[Fe_i]$ calculation error for various $[Fe_i]$ concentrations. Values in the range Δn_{avg}= 5 × 10^{13} to 5 × 10^{14} cm^{-3} were excluded due to the impact of the crossover point. The samples assumed to be a boron-doped crystalline silicon with dopant density of 10^{16} cm^{-3}.

The effect of injection level, Δn_{avg}, on the error in $[Fe_i]$ determination is shown in figure 4-3 for various $[Fe_i]$ concentrations when $N_A = 10^{16}$ cm^{-3} and τ_{other} = 300 µs. As shown, the injection levels in the range of $\Delta n_{avg} = 5 \times 10^{13}$ to 5×10^{14} cm^{-3} are excluded to avoid the impact of the crossover point near $\Delta n_{avg} = 10^{14}$ cm^{-3} [10, 22]. The results show that the error in determination of the dissolved iron concentrations is reduced by increasing the injection level at which the lifetime measurements are performed in both high and low injection levels ($<5 \times 10^{13}$ and $> 5 \times 10^{14}$ cm^{-3}). The main interest is in the injection level range is $\Delta n_{avg} > 5 \times 10^{14}$ cm^{-3} when analysing the results as the QSSPC lifetime measurement is commonly performed at those injection levels.

The results show that the error in the determination of [Fe$_i$] is less than |5|% when the concentration of iron impurity is the is below 10^{11} cm^{-3} and $\Delta n_{avg} > 5 \times 10^{14}$ cm^{-3}.

4.4.1.3 Impact of other recombination mechanisms, τ_{other}

As discussed in the previous chapter, the effects of any recombination centres in the bulk, other than intrinsic and SRH mechanisms, are represented by τ_{other}. In this section, the carrier lifetime measurements before and after iron-boron pair dissociation at $\Delta n_{avg} = 10^{15}$ cm^{-3} are simulated for different values of τ_{other} and iron concentrations when $N_A = 10^{16}$ cm^{-3}.

Errors in interstitial iron determination as a function of $[Fe_i]_{calculated}$ are shown in figure 4-4 for different values of τ_{other}. The results show a rising trend in underestimation errors (error < 0) by an increase in iron concentration in the highly iron contaminated range ($[Fe_i] > 10^{11}$ cm^{-3}). The underestimation errors show a sharp increase in this area when the iron is the dominant cause of recombination (τ_{other} > 100 µs) but become quite moderate when the iron impurity is not the limiting factor of the bulk lifetime anymore (τ_{other} < 100 µs). However, when $[Fe_i] < 10^{11}$ cm^{-3}

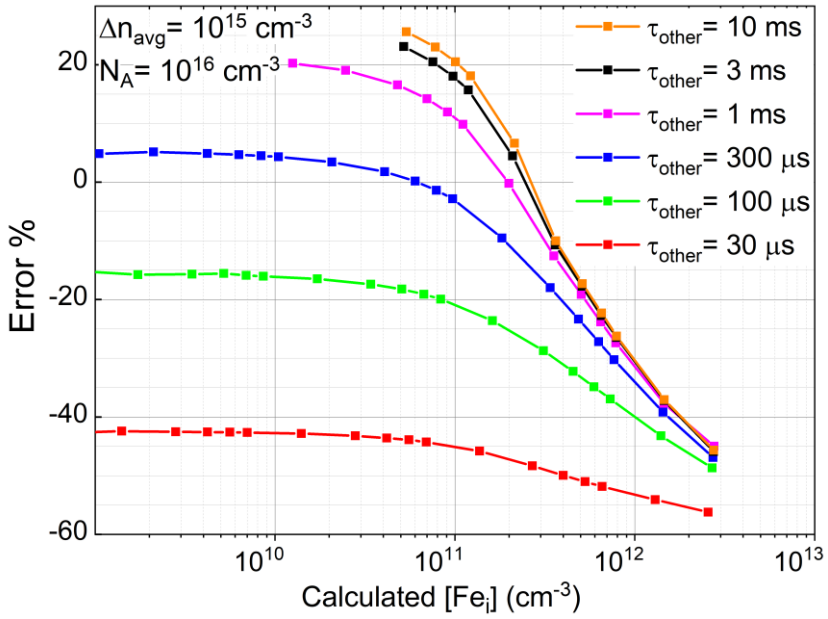

Figure 4-4: Effect of τ_{other} on the [Fe_i] calculation error as a function of [Fe_i] for boron-doped crystalline silicon samples with $N_A = 10^{16}$ cm^{-3} when lifetimes are simulated at $\Delta n_{avg} = 10^{15}$ cm^{-3}.

and τ_{other} < 100 µs the underestimation errors remain almost unchanged by increasing the dissolved iron concentration as the iron impurity is not the dominant recombination process.

4.4.1.4 Impact of doping levels

The carrier lifetime measurements at $\Delta n_{avg} = 10^{15}$ cm^{-3} before and after iron-boron pairs dissociation are simulated in this section for various boron concentrations and different iron concentrations when τ_{other}= 300 µs.

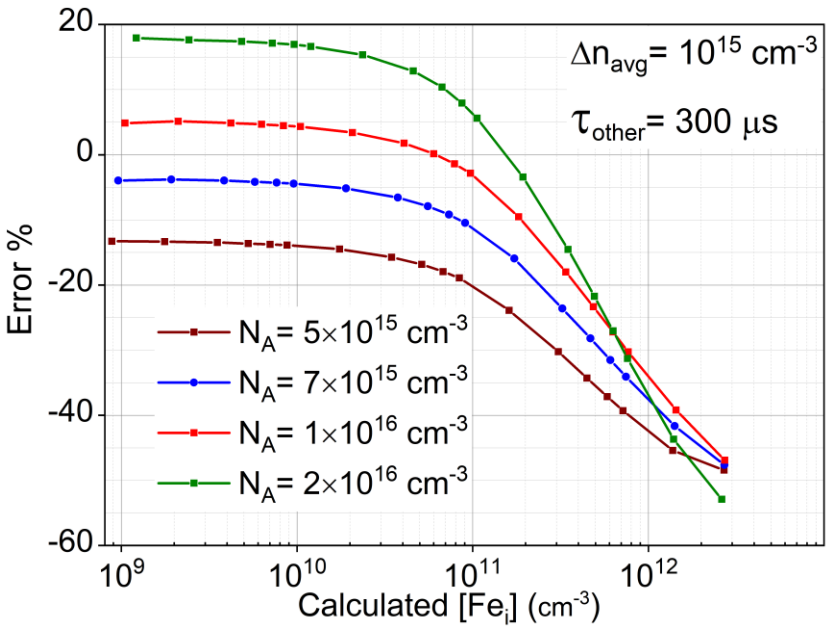

Figure 4-5: Effect of dopant density on the $[Fe_i]$ calculation error as a function of $[Fe_i]$ for boron-doped crystalline silicon samples with various N_A values when lifetimes are simulated at $\Delta n_{avg} = 10^{15}$ cm^{-3}.

The results presented in figure 4-5 show the error in calculated interstitial iron concentrations when the boron doping in the sample is changed from 5×10^{15} to 2×10^{16} cm^{-3}. Such changes in doping concentration is a reasonable assumption considering the silicon ingots grown for the PV industry these days by directional crystallisation such as the case for p-type mc-Si. However, even for such a conservative assumption, four times changes in dopant densities results in slight changes of around 20% in error in the determination of dissolved iron concentrations around the typical iron concentrations in the p-type mc-Si ingots ($[Fe_i] \sim 10^{11}$ cm^{-3}).

The change in the calculation error due to the change in doping concentration drops to 10% when the iron impurity is the dominant recombination mechanism with concentrations above $10^{12}\ cm^{-3}$. It should also be noted here that the doping concentration is one of the factors which is measured directly and reasonably accurately with QSSPC and, hence, there is not much uncertainty introduced by this factor to the determination of interstitial iron concentrations.

4.4.2 Simulation outcomes

The simulation results show that the iron concentration itself has the most significant impact on the accuracy of interstitial iron measurements in p-type mc-Si block [10]. Short carrier lifetimes due to either high iron contamination ($[Fe_i] > 10^{11}$ cm^{-3}) or other recombination mechanisms (τ_{other}< 100 μs) cause the underestimation of interstitial iron concentrations. The introduced errors from the mentioned method remain almost unaffected from the change in dissolved iron concentration when the iron impurity is not the dominant recombination process. However, an increase in dissolved iron concentration causes a drastic change towards the underestimation error when the iron was the dominant recombination mechanism in the bulk ($[Fe_i] > 10^{11}$ cm^{-3}).

4.5 Experimental Methods

A standard G6 mc-Si ingot shown in figure 4-6-a illustrates how it is cut to 36 blocks to produce 156 ×156 mm^2 wafers. The bottom of all blocks and sides of those which were in contact with the crucible were highly contaminated with iron atoms.

However, as the bottom part of the ingot solidifies earlier, the iron contamination from the molten silicon itself diffuse to the top molten phase from the bottom solid phase and makes the remaining melt relatively more contaminated. The trend remains the same during the solidification with enforcing the iron atoms to the top molten part until the very top part solidifies with a high level of iron contamination as there is no more space left for the iron to diffuse to above layers [49].

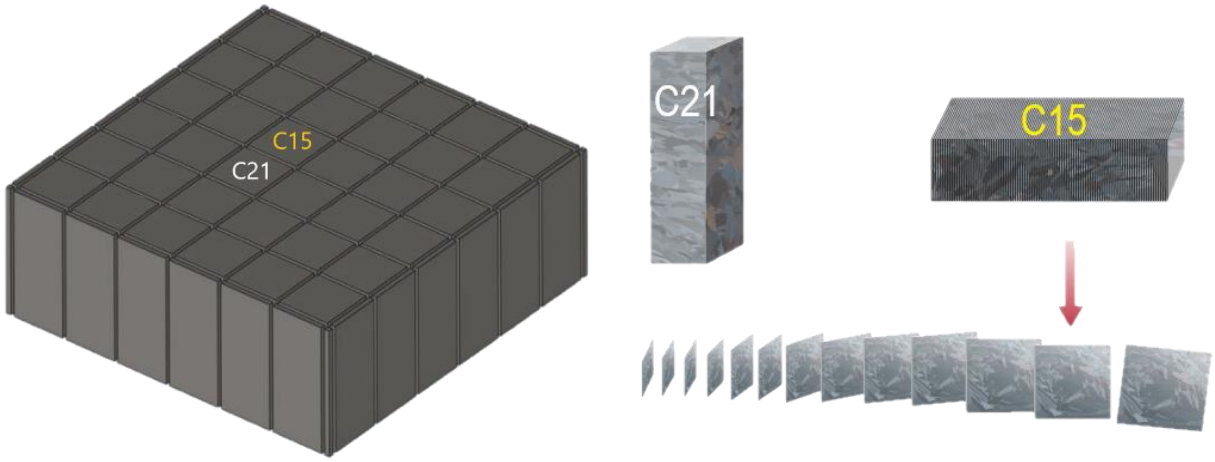

a b

Figure 4-6: (a) Two boron-doped multicrystalline silicon blocks from the middle of ingot. (b) The C21 was delivered as an uncropped block and C15 was wafered with each wafer labelled according to the block position.

The fact that the iron profile is vertically uniformed across the blocks in the ingot is used here to evaluate the accuracy of interstitial iron measurements on silicon blocks. Two adjacent blocks from the middle of an ingot, as indicated in figure 4-6-a, grown at Jinko Solar, were selected to perform interstitial iron measurements.

4.5.1 Measurements procedure

QSSPC lifetime measurements were performed before and after breaking Fe–B pairs on the C21 block using a BCT-400 (figure 4-7-a) measurement system from Sinton Instruments which was in the QSSPC mode with a 1000-nm IR-Pass Schott glass filter to remove short wavelength photon flux. The C21 was an uncropped rectangular block with a square base of 156 × 156 mm and a height of 367 mm. The measurement points started at 10 mm from the bottom edge up to 10 mm from the top edge with a 13 mm gap equal to the tool sensor height (figure 4-7-b) between each point to scan the whole height of the block.

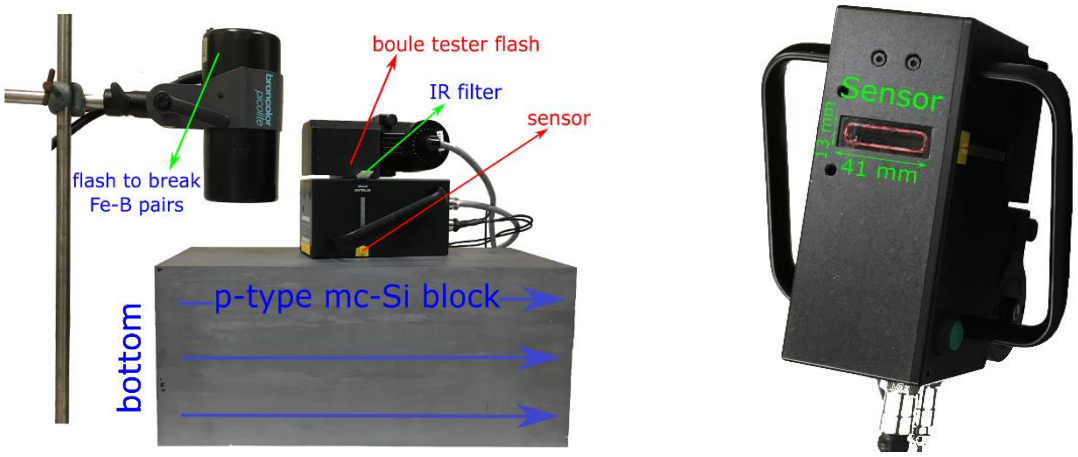

a b

Figure 4-7: (a) The setup used to determine interstitial iron concentration on a silicon block. Three blue lines on the side of the block show the path by which the boule tester scans the silicon block to measure lifetimes. (b) The RF sensor coil used in the boule tester. The scan steps were selected to be equal to the slit dimensions (slightly larger than the coil dimensions) to avoid overlapping measured areas.

As indicated with blue lines in figure 4-7-a, the measurements were performed in three columns on each side of the block to maximise the scanning area on each side.

For the QSSPC mode in all the measurements in this chapter, the system's flash power was set to 400 Ws with a 300 suns peak intensity and a 3.8 ms decay constant. Therefore, measured bulk lifetimes must be significantly shorter than the flash decay time constant (3.8 ms) to ensure the assumption of steady state conditions were valid to employ the QSS technique. Thus, only samples with the bulk lifetimes below 400 µs can be measured with reasonable accuracy. Transient measurements are recommended for longer lifetimes where dynamic changes in the generated excess carrier densities, Δn, occur during the flash decay as they are not accounted for under the QSS approximation [10].

For the wafer measurements, a total of fourteen 50 ×50 mm pieces were cut out of nine 156× 156 mm wafers from different heights of the C15 block. The wafers were passivated with PECVD deposited SiN_x films at 250° C for a total time of 30 minutes on both surfaces to eliminate the

impact of surface recombination velocity on the measured bulk lifetime. The measured data on the wafers as a well-established reliable method [22] is then used as a comparison benchmark for validating the extracted interstitial iron concentrations on the corresponding height of the C21 block. The lifetime measurements on wafers were performed by a WCT-120 standard lifetime tester from Sinton Instruments using the transient method.

Illumination procedure to break the Fe–B pairs in the block and the wafers were performed with a Broncolor Picolite flash with a peak power of 1600 W applying multiple flashes until complete dissociation was achieved. It has been shown that this method of breaking Fe–B pairs can achieve up to 99% dissociation in ingots for lifetimes above 5 μs [88]. The samples' temperatures were carefully monitored by an IR camera during the illumination, and the change in temperature did not exceed 2° C in the block and the wafers.

4.5.2 Lifetime Results

The carrier lifetime measurements were performed at an average excess carrier density of $\Delta n_{avg} = 10^{15}$ cm^{-3}. figure 4-8-a illustrates the minority carrier QSS-bulk lifetime (estimated lifetime after applying the transfer function used in Sinton BCT-400) in the C21 block before breaking the iron-boron pairs as a function of block height. The results show a total of 12 different columns on 4 sides of the block as dotted lines while exhibiting large variations amongst some scans. These variations are due to the presence of inhomogeneously distributed crystallographic defects, such as GBs and dislocation clusters [10]. The mean τ_{FeB} is the arithmetic mean of lifetime values determined on 12 points at the same height on four sides of the block. As can be seen in figure 4-8-a, there was a band close to the bottom of the block with significantly low lifetime which is usually cropped from the blocks before the wafering process.

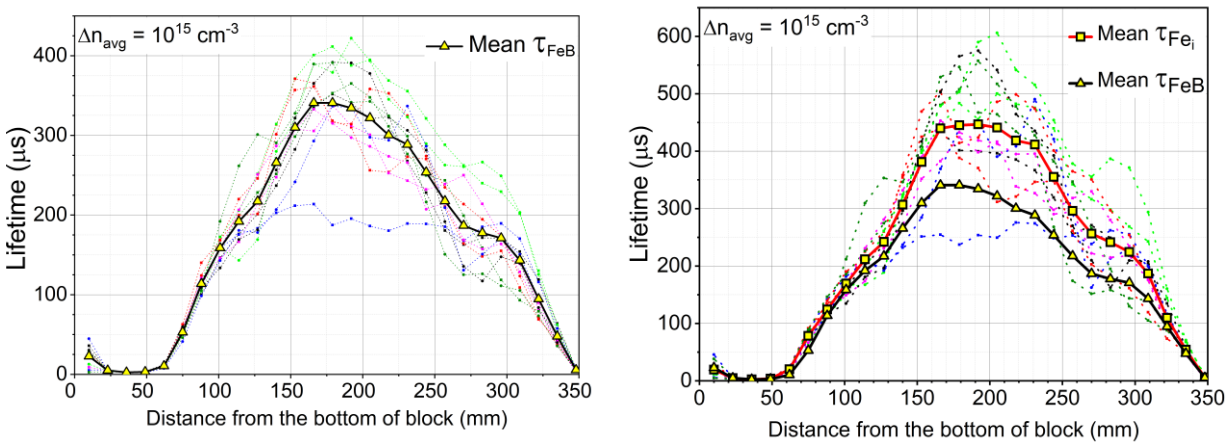

a b

Figure 4-8: (a) QSSPC bulk lifetime versus block position before breaking Fe–B pairs. The dotted lines represent the lifetime from 12 scans on the four sides of the block and the solid line represents the mean value of those 12 scans. (b) QSSPC bulk lifetime versus block position after breaking Fe–B pairs with illumination (red line with triangle data points) which is generally higher than the mean lifetime before breaking pairs (black line with square data points). The dotted lines represent the lifetime from 12 scans on the four sides of the block after breaking Fe–B pairs.

The very low lifetime at this region is due to the presence of small grains as well as high levels of contamination from the contact with the ingot crucible.

The same procedure was performed for the lifetime measurements at the same points on the block after breaking the iron-boron pairs with multiple flashes as mentioned before. The results are shown in figure 4-8-b exhibiting a general increase in the lifetimes in comparison with the lifetimes before breaking the iron-boron pairs. According to figure 4-1, such an increase was expected as the measurements were performed above the crossover point (~10^{14} cm^{-3}) at Δn_{avg} = 10^{15} cm^{-3} [22]. Here again, the mean τ_{Fe_i} is the arithmetic mean of lifetime values determined on 12 points at the same height on four sides of the block after breaking the iron-boron pairs. The mean τ_{FeB} is also shown in figure 4-8-b to illustrate the average increase in the minority carrier lifetime to the mean τ_{Fe_i} after dissociation of iron-boron pairs in the block.

4.5.3 Determination of iron concentrations on the block

Before proceeding any further analysis of the collected lifetime data, it must be confirmed that the presence of dissolved iron impurity in the block is the reason behind the observed changes in the carrier lifetimes after sample illumination.

In order to confirm that the changes in the lifetime before and after flashing the block were due to iron-boron pair dissociation (presence of dissolved iron), the sample was left in the dark allowing the iron and boron atoms to re-bond to form Fe-B pairs again. It has been shown in [22] that during the repairing time, such lifetime data exponentially decay at a rate of $\frac{1}{\tau_{assoc}}$ (where τ_{assoc} is the association time) for silicon wafers containing interstitial iron that is, in principle, applicable to block measurements as well. Multiple lifetime measurements were performed during this relaxation period at one point on the block to monitor the rate at which iron and boron atoms were repairing. The lifetimes were then used to calculate the relative interstitial iron concentration as a function of elapsed time after complete iron-boron pairs dissociation. The results are illustrated in figure 4-9 for the mentioned set of measurements on the block.

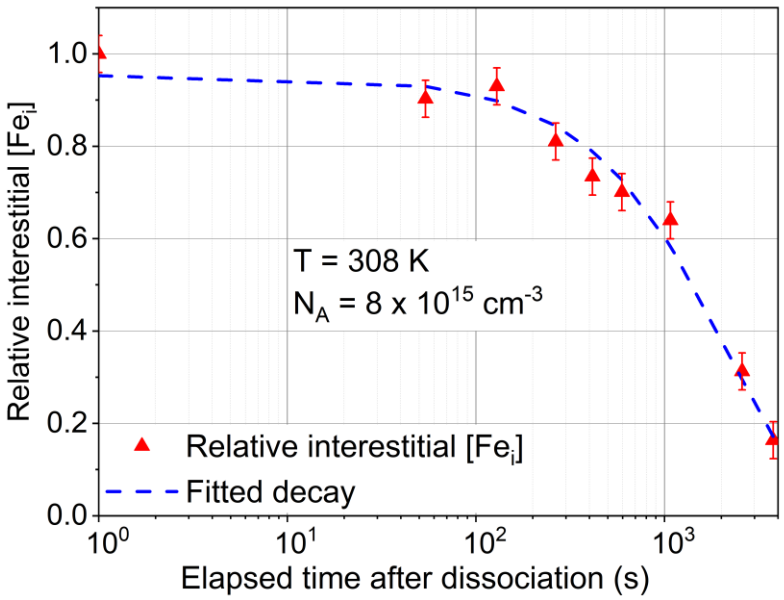

Figure 4-9: Fe–B repairing as a function of time, after breaking the Fe–B pairs. The error bars were obtained from the 4% uncertainty in lifetime of the bulk samples as reported in [89]. The repairing time extracted from the fitted decay was 25 min, approximately equal to the expected value which was calculated based on the doping and temperature (23 min).

Tan *et al.* [90] showed the relationship between the Fe–B pair association time, τ_{assoc}, and the dopant density, N_A, and the sample temperature, T (in kelvin), can be expressed as:

$$\tau_{assoc} = \frac{5.7 \times 10^5}{N_A} T \, exp \frac{0.66}{kT} \qquad 4\text{-}3$$

where k is the Boltzmann constant.

The dopant density of 8×10^{15} cm^{-3} which is determined from the dark conductance during the lifetime measurement and the block temperature of 308 K results in an expected association time of approximately 23 minutes for iron and boron atoms to form Fe–B pairs again. The time agreed well with repairing time of 25 minutes extracted from fitting the exponential decay to the lifetime data in figure 4-9. These results confirm that the observed increases in lifetimes after the block illumination were indeed due to the presence of interstitial iron atoms.

The lifetime data presented in figure 4-8-a and b were used in equation 4-1 to calculate the interstitial iron concentration with the method developed by Macdonald *et al*. [22] and the recombination parameters (energy levels, capture cross sections and the thermal velocity) from Ref [91] for $\Delta n_{avg} = 10^{15}$ cm^{-3}, including the impact of the doping density variation along the block. The calculated interstitial iron concentrations along the block are shown in figure 4-10. The interstitial iron concentration displays an initial rapid decrease along the growth direction in the first 10 cm of the bottom of the block and then exhibits a steady increase in the middle part of the block with a final sharp increase at the top of the block. Such a trend has earlier been reported by several authors, for example, Sinton *et al*. [12] and Mitchell *et al*. [88], and occurs because of the solid-state in-diffusion of iron from the ingot crucible, and impurity segregation into the molten phase during crystallisation, respectively [10].

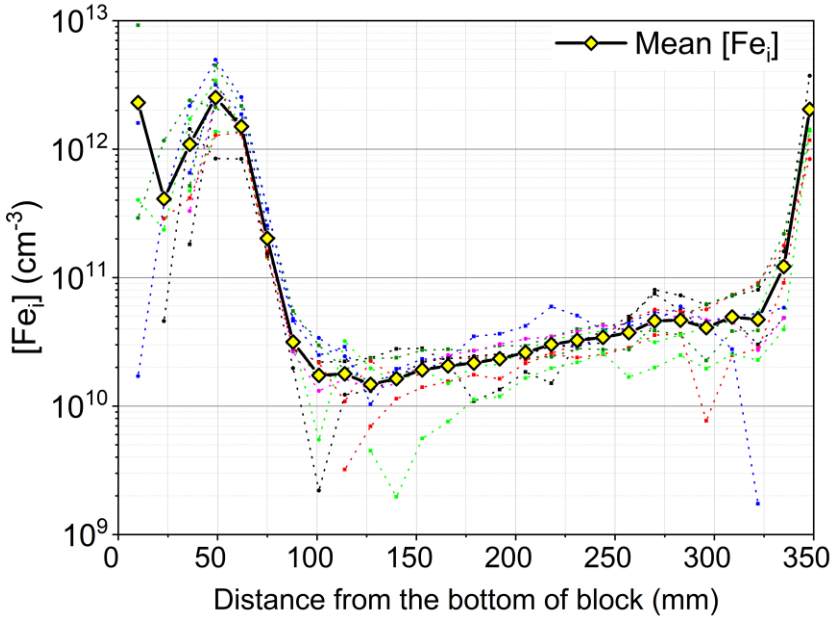

Figure 4-10: Extracted interstitial iron concentration as a function of the block position. The dotted lines represent the $[Fe_i]$ on 12 columns on the four sides of the block and the solid line represents the mean value of those 12 at each point.

The notable observation here is that the extracted dissolved iron concentration on different sides of the block are less scattered in comparison with the lifetime data in figure 4-8. This confirms that the dissolved iron concentrations are almost equal at the same height of ingot across adjacent blocks which makes our initial assumption reasonably accurate.

4.5.4 Iron concentrations: block vs wafers

As mentioned before, a WCT-120 lifetime tester is used to perform the lifetime measurements on 12 wafers after passivating their surface with SiN_x deposition. The wafers were chosen from different heights of the middle part of C15 block as the bottom and top parts are usually cropped before wafering. The lifetime measurements were performed before and after breaking iron-boron pairs to determine the interstitial iron concentrations on the wafers. Figure 4-11 presents the results to be compared with the results from the block measurements.

Liu *et al.* [92] have recently shown that the surface passivation via SiN_x deposition with PECVD causes gettering of interstitial iron into the SiN_x films resulting in lower measured $[Fe_i]$ on passivated wafers in comparison with initial contamination before passivation. The $[Fe_i]$ reduction in the wafers after passivation is about 20% due to the gettering effect after applying the model in Ref [92] for the SiN_x deposition conditions used in this work (deposition temperature of 250° C for a total time of 30 minutes). The corrected interstitial iron concentrations are also shown in figure 4-11, demonstrating the expected $[Fe_i]$ values in the as-cut wafers. As can be seen, the same trend in increasing in the interstitial iron concentration with increasing ingot height is observed in wafers as in the data for the block measurements. The error bars for the wafer data at each point was calculated assuming an 8% uncertainty in the transient lifetime measurements before and after iron-boron pair dissociation [89].

Figure 4-11 also shows the mean values of the measured $[Fe_i]$ that was determined on the block with the error bars considering 4% uncertainty in the measured lifetimes on the block before and after iron-boron pair dissociation [89]. The measured $[Fe_i]$ values were then corrected according to the doping, N_A, and τ_{other} values at each point using the error plots presented in figure 4-4, figure 4-5 and [10]. The uncorrected and corrected block data are both shown in figure 4-11. It should be noted here that the measurement of the interstitial iron concentration below 10^{11} cm^{-3} on the block is subject to less uncertainty than wafer-based measurements, because of the considerably larger volume to surface ratio, as well as the well-defined surface conditions in the block [10].

There is a good agreement between sets of data from the wafers and the block after the relatively minor correction made for the effects of non-uniform carrier profiles in the block measurements as well as the effects of SiN_x gettering in the wafer data.

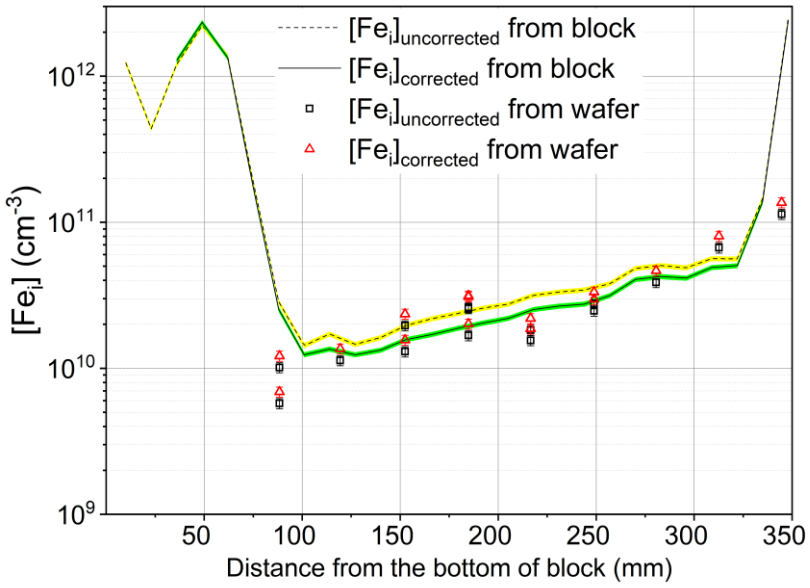

Figure 4-11: Average interstitial iron concentration from the block before and after correcting for nonuniform carrier profiles, and the $[Fe_i]$ from the wafers before and after correcting for SiN_x gettering. The error shadow on the block $[Fe_i]$ data is from 4% uncertainty in QSS lifetime measurements, and the error bars on the wafer data are 8% uncertainty of the transient lifetime data as reported in [89].

The results confirm the reliability of the determination of dissolved iron concentration values using block lifetime measurements under typical measurement conditions for p-type multicrystalline ingots, and can, in any case, be corrected for the effects of non-uniform injection levels [10].

4.6 Comparison between QSSPC and PLIR

The PLIR lifetime measurement used in this section as an independent method to evaluate the accuracy of the QSSPC in the determination of interstitial iron concentrations on semi-infinite thick silicon samples.

In this section, the same block was wafered after performing interstitial iron concentration measurements with the both QSSPC and the PLIR image techniques on the block. The sample was an edge block of a G6 industrial p-type high-performance multicrystalline ingot with doping in the

range of 1–3 Ω.cm [93]. The block was cut into standard 180 μm thick wafers and nine, evenly distributed across the height of the block, were taken for the iron measurements. A plasma-enhanced chemical vapor deposition Roth and RauMaia tool used to deposit silicon nitride (SiN) on both surfaces at 440 °C for total 4.5 minutes [93] and the lifetime measurements were performed with a WCT-120 lifetime tester.

As shown in figure 4-12-a, lifetime measurement results from the QSSPC are visualised in a much lower resolution image with the pixel size equal to the tool coil dimensions. As indicated in figure 4-12-a and b, the measured lifetime ranges are different between the QSSPC and PLIR due to the different injection levels that each measurement technique is performed at. While the QSSPC measurements on both block and wafer samples were performed at $\Delta n_{avg} = 10^{15}$ cm^{-3}, the PLIR image technique is typically performed at $\Delta n_{avg} = 10^{13}$ cm^{-3}.

As the PLIR provides more details with much higher resolution, the highly contaminated parts of the block which are in contact with crucible are illustrated clearly. The very dark region in the bottom and the right (bottom line of the image) of the block in figure 4-12-b are representing these parts.

Figure 4-12-c shows the normalized (wafer data are normalized from min to max measured lifetime as the scale are different from those in the a and b which are collected from block side) lifetime measurement results on three wafers from the bottom, middle and top regions of the block after wafering. Apart from the expected difference in the lifetimes in the wafers, it should be noted here that the small size of grains in the bottom of the block is clearly shown on the left wafer in comparison with the other two.

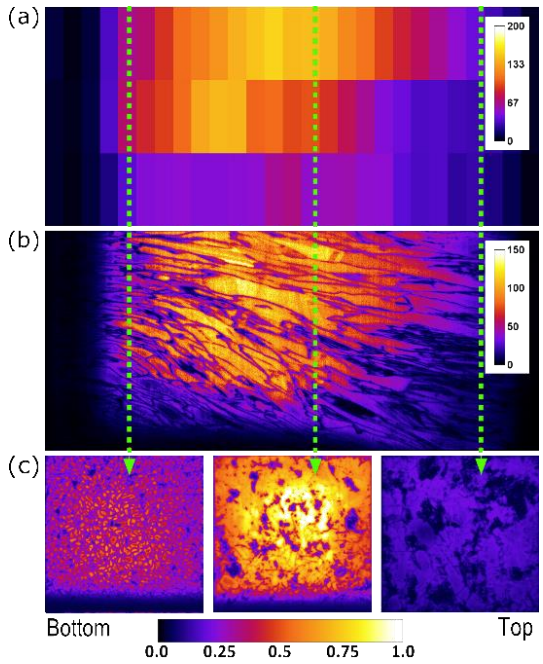

Figure 4-12: Bulk lifetime measurements made on a side face of the mc-Si brick using (a) QSSPC mapping and (b) PL imaging both in units of μs. (a) and (b) are orientated with the bottom of the brick on the left-hand side. (c) Doping normalized PL images are shown in arbitrary units for three exemplary surface passivated wafers cut from the brick. The green dotted arrows indicate the position which the wafers originated from in the brick [93].

The same procedure followed with a flash with a peak power of 6400-J for illumination of the entire block in both QSSPC and PLIR measurements to dissociate iron-boron pairs in the samples. The extracted interstitial iron concentration in the block by the PLIR image technique is presented in figure 4-13-a. The results show the high iron contamination was indeed responsible for the very low lifetime at the bottom and the right side of the block due to iron diffusion from the crucible to the molten silicon during the crystallisation [10]. The general increase in dissolved iron concentration from the bottom to the top of the block is also due to the segregation of iron at the liquid/solid interface.

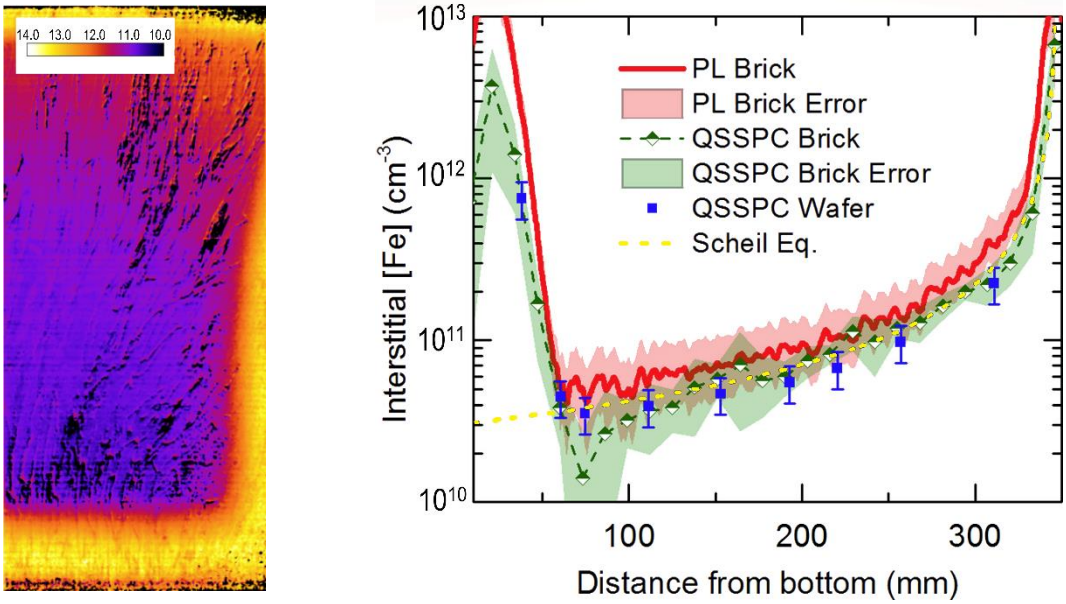

a b

Figure 4-13: a) Interstitial iron concentration [Fe_i] image from PL imaging. The colour scale values indicated are Log_{10} of interstitial iron concentration in units of cm^{-3}. b) Interstitial iron concentration as a function of brick height for the PL and QSSPC methods on bricks in comparison to the QSSPC method surface passivated wafers. The heavily contaminated areas are excluded from the averages. The Scheil equation is plotted with the segregation coefficient of 1.5×10^{-5}. Error bars and areas are calculated based on estimated uncertainty in the lifetime measurements used for calculating [Fe_i][93].

Figure 4-13-b shows the extracted interstitial iron concentration in the block with both QSSPC and the PLIR image as well as in the wafers. There are good agreements between the results from two techniques as well as the measured results on the wafers particularly in the trend of dissolved iron in the samples [93]. The results from the QSSPC measurements on the block were corrected according to [10], and error bars and error area in the results are calculated from [10, 89, 93].

Figure 4-13-b also illustrates the fitted Scheil equation [94] in the yellow dashed line with the segregation coefficient, $k = 1.5 \times 10^{-5}$ for mc-Si, the block dimensions while the initial impurity concentration was adjusted to fit the equation to the measured data. As expected, the fitted Scheil equation did not agree with the measurement results in the first 50 mm of the block bottom region as the interstitial iron concentration is dominantly affected by the iron diffusion from the crucible

[9]. However, for the rest of ingot height, the measured interstitial iron concentration profile displayed a good agreement with the expected trend from Scheil equation which is a further validation for the $[Fe_i]$ measurements by both techniques.

In this section, the interstitial iron measurement results on the p-type mc-Si block by QSSPC technique were confirmed by the results employing the PLIR imaging technique as an independent lifetime measurement method. The results were also in good agreements with the extracted dissolved iron concentrations in the wafers from different heights of the same block after wafering [93].

4.7 Summary

A brief explanation of the sources of typical impurities and their effects on silicon ingots, blocks and wafers were presented in this chapter. Then, the focus was on interstitial iron contamination as one of the most common impurities in silicon which considerably limits the minority carrier lifetimes, particularly in p-type materials. After which, a systematic study on the accuracy of interstitial iron concentrations extracted from QSSPC lifetime measurements on silicon blocks was presented. The simulation results demonstrated that the error in the extracted interstitial iron concentration is generally less than 20% for typical iron contamination densities in the central regions of multicrystalline ingots ($[Fe_i] < 10^{11}$ cm^{-3}). The modeling and simulation tool enabled us to validate the accuracy of the interstitial iron concentration measured with the BCT-400 tool and correct the results for different cases. In general, the non-uniform carrier profiles during the QSSPC measurements in an ingot resulted in only a small error in the measurements of dissolved iron concentrations at the ingot level. The measurement results were in good agreement with $[Fe_i]$ measurements on wafers from an adjacent block as a comparison benchmark.

Chapter 5: Improving Transient Photoconductance Lifetime Measurements on Ingots with Deeper Photogeneration

5.1 Introduction

As discussed in chapter 3, the effective lifetime itself is a decisive factor in the choice of which lifetime measurement technique to apply [79, 95]. The quasi-steady state photoconductance is valid for the lifetime range up to 150-200 μs and the transient photoconductance decay for lifetimes above this range. The reason that transient photoconductance decay is practically difficult to use in samples with low carrier lifetimes is the illumination source decay time which is typically not fast enough to measure lifetimes below 100 μs. On the other hand, there are dynamic changes in carrier density in high ranges of lifetime when using typical flash decay times. Therefore, the assumptions for the steady state approximations are not valid and so transient decay lifetime measurements are recommended techniques for silicon blocks with high minority carrier lifetimes [86].

In this chapter, the simulation tool developed in the third chapter is employed to investigate influential parameters on the accuracy of transient photoconductance lifetime measurements on silicon blocks. Then, the application of new filters with longer cut-off wavelengths for deeper carrier density generation is proposed to improve the accuracy of transient lifetime measurement on semi-infinite silicon samples. The simulation results will then be supported by measurement results performed on a p-type Cz silicon block [78].

5.2 Accuracy of Transient Photoconductance Lifetime Measurements

As discussed in the third chapter, the high surface recombination velocity of the as-cut unpassivated surface induces a large carrier diffusion current towards the surface which leads to the inaccuracy in photoconductance lifetime measurements [11, 15, 86]. Although the transient photoconductance decay is less prone to the surface recombination effects, the accuracy of the lifetime measurements can improve by reducing the impact of high SRV. There are two parameters during the transient measurement that can be altered to reduce the high SRV effects which are discussed in the following sections.

As shown in figure 3-9, one effective parameter on the accuracy of reported transient lifetimes is the elapsed time after terminating the light source at which the lifetime measurement is performed. The other factor is the initial injection level reached in quasi-steady state conditions before terminating the light source. Several simulations are performed to demonstrate the effects of each factor on the accuracy of transient measurements, while the impact of the initial injection level is confirmed by measurement data on a p-type Cz silicon block [96].

5.2.1 SRV impact and elapsed time after light source termination

As illustrated in figure 3-8, the peak of the carrier density profile moves deeper in the bulk over time after the light source is terminated [78]. Therefore, surface recombination effects are largely removed from the carrier density decay over time. Consequently, the accuracy of the transient lifetime measurement depends on the time elapsed after which the decay rate is measured.

The simulation results of the transient lifetime for several injection-independent bulk lifetimes as a function of elapsed time after terminating the flash with an intensity of 400 suns are presented in figure 5-1 [96].

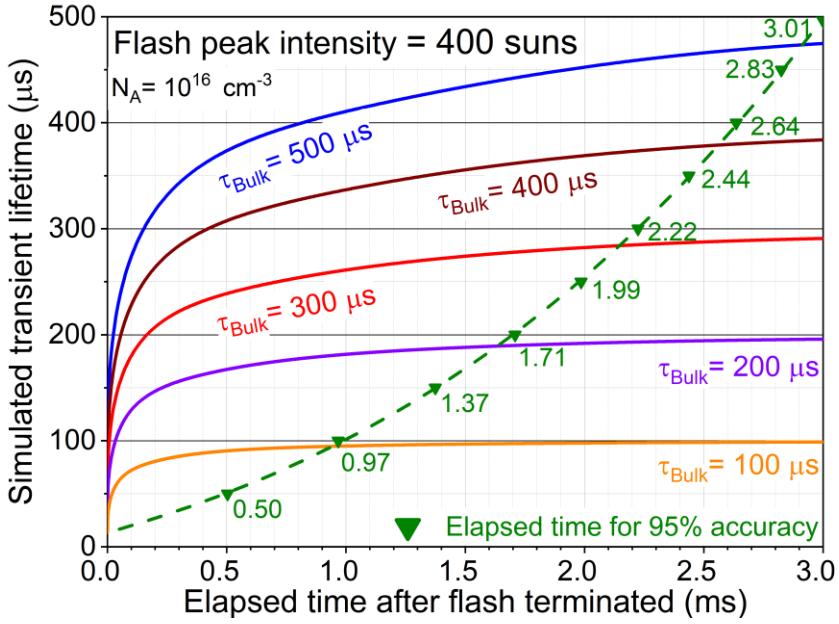

Figure 5-1: Simulated transient lifetime value vs the time of measurement elapsed after the light source is terminated. The labelled data are the required elapsed time to report the lifetime with 95% accuracy. The dashed line is fitted to present the required elapsed time for 95% accuracy as a function of the bulk lifetime [96].

The figure demonstrates that a very accurate result is achievable in principle using the transient technique, if a sufficiently long time has elapsed. In practice, the achievable delay time is constrained by the initial injection levels due to the flash intensity as there is typically a constrain on the injection level in which the lifetime measurement is performed. Figure 5-1 also specifies the required delay time after the flash is terminated for the simulated bulk lifetime to approach the true bulk lifetime with 95% accuracy. The required elapsed time starts from 10 times longer than the bulk lifetime for lower lifetimes but reduces to 6 times longer for lifetimes around 500 microseconds. Hence, a conservative approach for accurate measurement results is that the elapsed time has to be ten times longer than the sample bulk lifetime [96].

5.2.2 Initial injection level

As mentioned in the previous section, the transient lifetime measurements are usually performed when the excess carrier density decays to a specific injection level, Δn_{avg}. Thus, the initial excess carrier density in QSS conditions before terminating the light source determines the required elapsed time to decay to the specific Δn_{avg}.

The simulation tool was employed to evaluate the impact of light source intensity (as the direct measure of initial excess carrier density) on the accuracy of transient photoconductance decay lifetime measurement. Figure 5-2-a shows the measured transient lifetime with different flash intensities at $\Delta n_{avg} = 10^{15}$ cm^{-3} for different bulk lifetimes. As can be seen, the $\tau_{transient}$ increased towards the actual bulk lifetime as the flash intensity increased in all the presented cases. The reason behind such an improvement was that the higher flash intensity generated higher initial excess carrier density before the light source was terminated. Therefore, the elapsed time for the excess carrier density to decay to $\Delta n_{avg} = 10^{15}$ cm^{-3} was longer in comparison with lower flash intensities resulting in more accurate results as shown in figure 3-9. It should be noted here that the reported transient lifetimes are noticeably lower than the corresponding bulk lifetimes when the flash peak intensities are below 200 suns [96]. In contrast, the difference between the reported lifetime with 600 suns and the result with 400 suns peak intensity across different bulk lifetimes was insignificant. Therefore, the light source with 400 suns peak intensity appeared to be a suitable choice for transient measurements at $\Delta n_{avg} = 10^{15}$ cm^{-3} in this lifetime range.

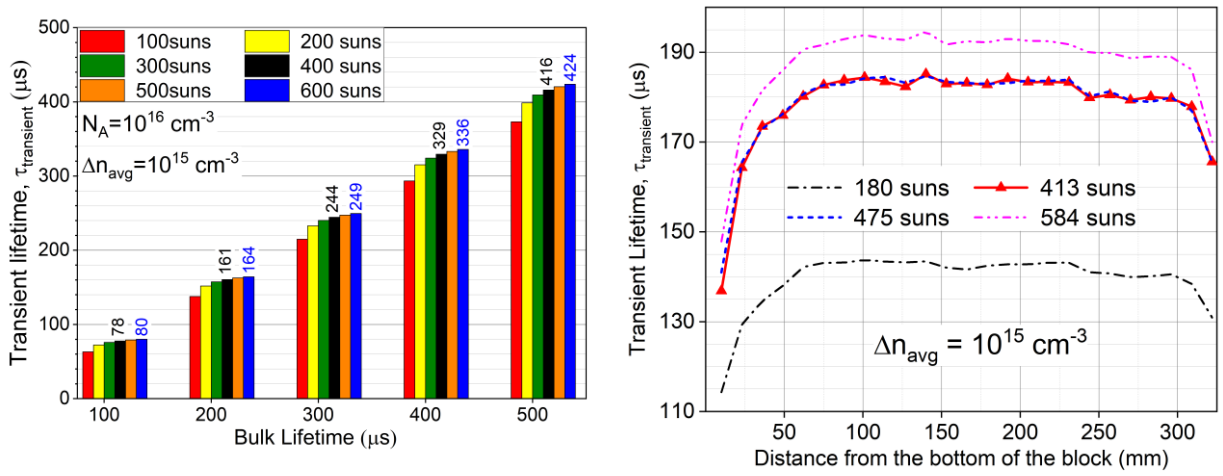

a b

Figure 5-2: (a) Simulated transient lifetime with different flash peak intensities. (b) The measured transient lifetime on a standard p-type Cz block at $\Delta n_{avg} = 10^{15}$ cm^{-3} with flash peak intensities of 180, 413, 475 and 584 suns [96].

5.2.3 Measurements results

Several transient lifetime measurements with different flash intensities were performed along a standard p-type Cz silicon ingot at $\Delta n_{avg} = 10^{15}$ cm^{-3}. Different grey filters were inserted in front of the flash to modify the light intensity to the values comparable to the simulation assumptions for light sources. The results are shown in figure 5-2-b for four different flash peak intensities.

As expected from the simulation results, there was an almost 30% increase in the reported lifetimes when the light source intensity increased from 180 to 413 suns. However, the difference between the measured transient lifetimes reported by 413 and 584 suns peak flash intensities were mostly less than 5%.

The simulations and the measurement results confirmed that increasing the elapsed time after the light source terminated and prior to performing transient lifetime measurements significantly reduced the impact of high surface recombination velocity in as-cut samples [96]. The solution to

increase this elapsed time when measurements were performed at a specific injection level was to increase the initial excess carrier densities via stronger light intensities.

5.3 Deeper generation with long cut-off wavelengths filters

It has previously been shown that reducing the impact of SRV significantly increases the accuracy of lifetime measurements due to the dominance of bulk recombination. In this section, the light source spectrum was modified to investigate the effects that a high SRV from an unpassivated surface has on the accuracy of the transient photoconductance decay for lifetime measurements.

Schuler *et al*. [97] compared two lifetime measurement techniques with a steady state and transient photogeneration on thick silicon samples. Their work demonstrated the improved accuracy of lifetime measurements by using a deeper generation profile in MDP (Microwave Detected PhotoConductance) in comparison with μPCD technique (microwave detected PhotoConductance Decay). Several studies (for example Mitchell *et al.* in [14, 88, 98], and other researchers in [86, 99, 100]) have also demonstrated the accuracy of Photo-Luminescence techniques for lifetime measurements on silicon blocks, such as PL intensity Ratio methods, in which the ratio of PL intensities at two different detection wavelength ranges is used to determine the lifetime. More recently, Chung *et al*. [101], have demonstrated a PLIR technique in which two different excitation wavelengths of 915 nm and 1064 nm are used to generate different carrier profiles with deep generation [78].

New filters with longer and sharper cut-off wavelengths are proposed here to remove the part of the spectrum in which photons generate shallower excess carrier densities close to the sample surface. Theoretically, deeper photogenerations move the peak of excess carrier densities deeper away from the sample surface which must significantly reduce the carrier diffusion into the

surface. Such a reduction in the carrier diffusion to the surface will consequently increase the measured transient lifetime.

5.3.1 Flash and filters spectrums

The assumptions for the light source and the filter transmission in the simulations in this thesis are adapted from a Sinton Instruments BCT-400 tool setup which is used in all measurements. A X5dR Q-flash, a xenon flash lamp from Quantum Instruments was used as the light source in the tool with a pre-filter peak photon flux of $1.27 \times 10^{21}\ \mathrm{cm^{-2}s^{-1}}$, equivalent to an intensity of 5500 suns. A standard 1000-nm IR-Pass Schott glass RG1000 filter was inserted in place to remove the short wavelengths photons which further reduced the on-sample photon flux to $2.3 \times 10^{20}\ \mathrm{cm^{-2}s^{-1}}$. The xenon flash spectrum and the measured transmission function for the standard RG1000 filter are shown in yellow and green lines respectively in figure 5-3-a.

Two high-performance OD-4 long-pass filters from Edmund Optics with a sharp cut-off wavelength at 1050 nm (EO-1050) and 1100 nm (EO-1100), respectively were proposed to generate such deep photogenerations. Figure 5-3-a also shows the measured transmission function for these two filters along with the standard RG1000 filter and the xenon flash spectrum. The filtered photon flux which hit the samples are shown in figure 5-3-b for three filters. The total filtered photon flux by RG1000 were reduced by 40% and 60% after removing the short wavelengths photons by replacing EO1050 and EO110 respectively [78]. Therefore, in practice with a given light source, there is a trade-off between achieving a deeper generation profile and initial generated excess carrier density to improve the accuracy of transient lifetime measurements.

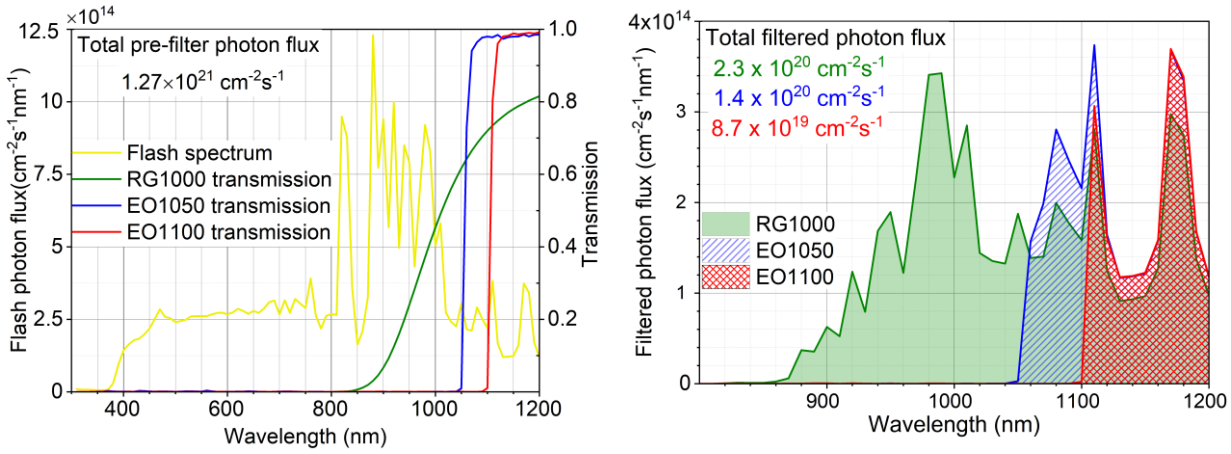

a b

Figure 5-3: (a) Xenon flash spectrum and measured filter transmission functions. (b) Filtered light spectrum with 3 filters as functions of wavelength. The total light intensity is reduced as the cut-off wavelength increases.

Since the photons with shorter wavelengths were removed from the photon flux, the light was mostly absorbed deeper in the bulk and so the carrier density profiles' peaks move deeper in the bulk. The generation and carrier density profiles for three filters are illustrated in figure 5-4 for a semi-infinite p-type silicon sample with the bulk lifetime of 300 µs. As can be seen, the carrier profile peak moved about 125% deeper below the surface from its initial 500 µm depth when the RG1000 filter was replaced by EO1100. However, such a deeper generation profile is achieved at the cost of significant reduction in initial excess carrier density as shown on the carrier profile for each filter.

In the next section, the transient lifetimes are simulated using the conditions in figure 5-4, for each filter, to evaluate the impact of deeper photogeneration on the accuracy of the transient photoconductance lifetime measurements [78].

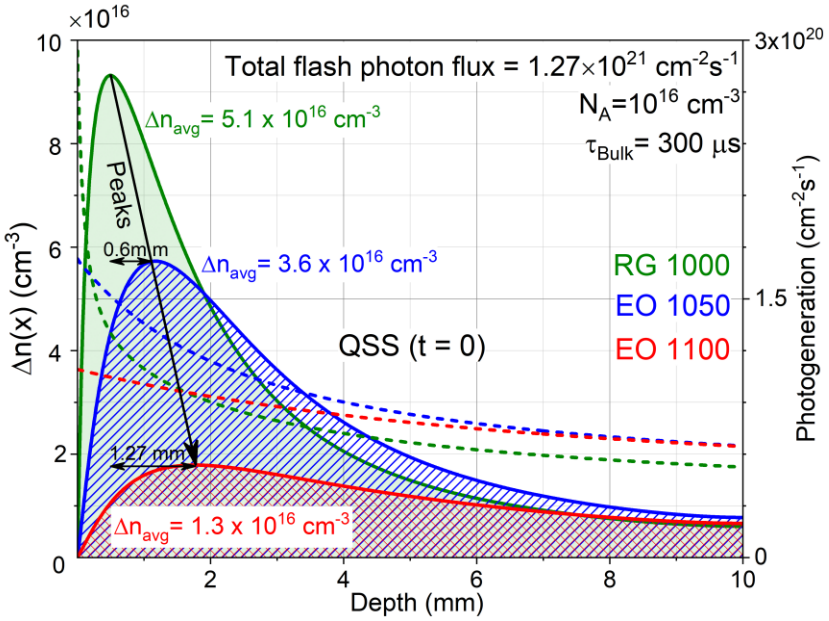

Figure 5-4: Generation (dashed lines) and excess carrier density (solid lines) profiles at $t = 0$ as functions of sample depth for the three different filters: just before terminating the flash and under steady-state conditions with the pre-filtered photon flux = 1.27×10^{21} $cm^{-2}s^{-1}$ (generating different initial injection levels as labelled)

5.3.2 Lifetime simulation with different filters

Figure 5-5-a is a plot of the decay in excess carrier densities that were illustrated in figure 5-4 as a function of elapsed time after the flash was turned off for three filters. As mentioned in the third chapter, the transient lifetime inversely correlates to the rate at which the excess carrier density decays in the absence of photogeneration [102]. The normalised excess carrier densities' decays are illustrated in figure 5-5-b for direct comparison amongst three filters. The results show that despite the significant reduction in the initial excess carrier density, the decay's rate decreased as the cut-off wavelength increased.

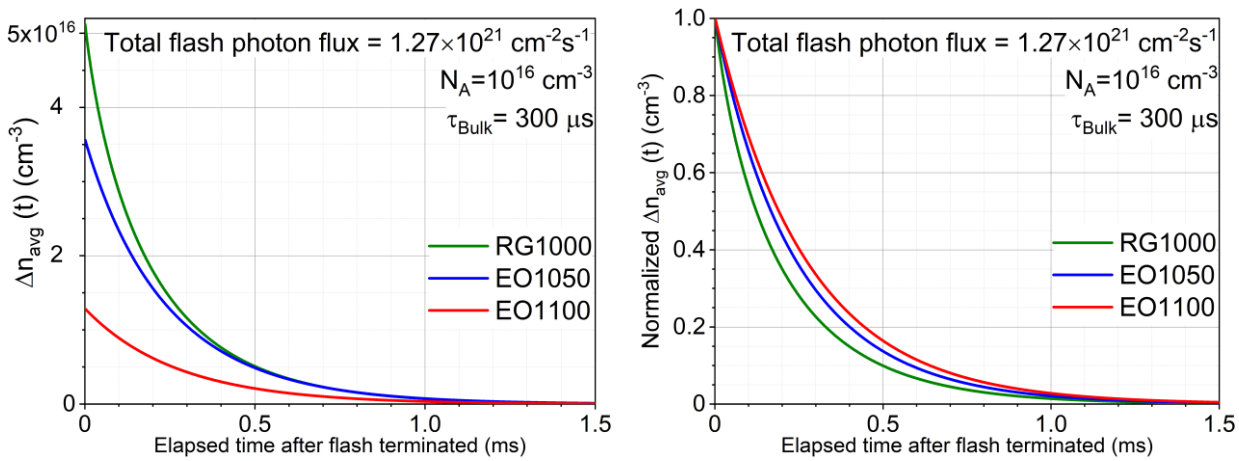

a b

Figure 5-5: Simulated (a) excess carrier density, and (b) normalised excess carrier density, decays as function of elapsed time after the flash is terminated for a semi-indefinite p-type silicon sample with three filters and total pre-filtered photon flux = 1.27×10^{21} $cm^{-2}s^{-1}$.

The simulation of typical transient PCD lifetime measurements with three filters as function of injection levels (elapsed time) provides quantities analysis on the improvement of measurement results. Figure 5-6 shows the subsequent simulated transient lifetimes, calculated from the decays in figure 5-5-a, as a function of injection level after the flash was terminated for τ_{bulk} = 150, 300 and 500 μs for comparison.

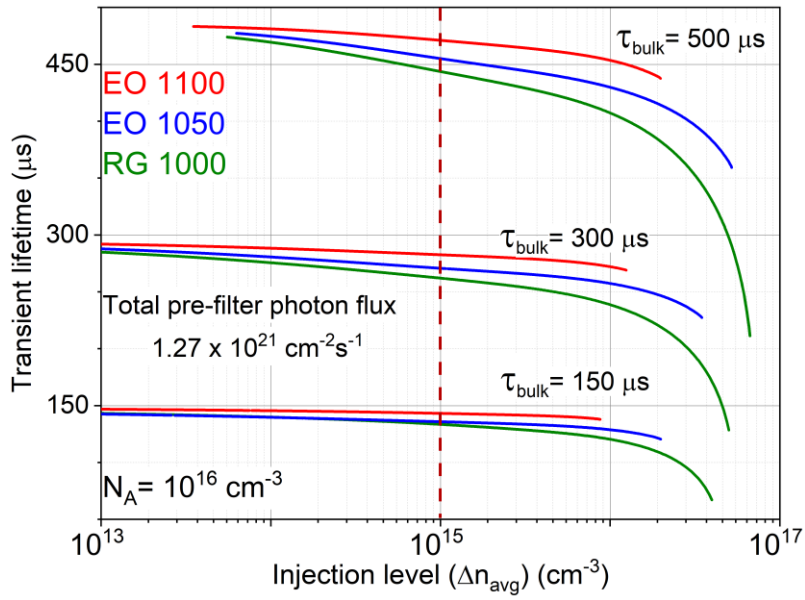

Figure 5-6: Simulated transient lifetime as functions of injection levels for three different filters for bulk lifetime of 150, 300 and 500 μs, for boron-doped samples with $N_A = 10^{16}$ cm^{-3} [78].

As can be observed, the filters with longer cut-off wavelengths reported higher transient lifetimes which were closer to the assumed bulk lifetimes at all injection levels. As the purpose of this study was to investigate the effect of deeper photogeneration, the lifetime assumed to be injection level-independent in all cases to simplify the simulations. The accuracy of the reported transient lifetime improved by approximately 10%, when EO1100 replaced the standard RG1000 filter at a typical injection level of $\Delta n_{avg} = 10^{15}$ cm^{-3}, which the PCD lifetime measurement was performed. As mentioned already and shown in figure 3-7, the impact of high surface recombination velocity reduced as time elapsed after eliminating the light source. Therefore, the gap amongst reported transient lifetimes using different filters reduces as the excess carrier densities decay to lower injection levels.

In the next section, several transient lifetime measurements are performed on a p-type Cz silicon block with three filters to evaluate the simulation results presented in this section.

5.4 Measurements results

Three sets of transient measurements on a Cz block were performed with a BCT- 400 measurement system from Sinton Instruments in the transient mode with the RG1000 filter and the EO 1050 and EO 1100 filters respectively. The measurements were performed on a rectangular block with a square base of 156×156 mm and a height of 320 mm, cut from a standard industrial p-type Cz monocrystalline silicon ingot. Transient lifetime measurements were first performed at one fixed point on the block to compare lifetime results at different injection levels measured with three filters [78].

Figure 5-7-a displays the transient lifetime results measured on a fixed point on the block by three different filters. The results showed that the longer cut-off wavelength filters reported longer measured lifetimes at all injection levels. As can be seen, there was a much larger gap between the

RG1000 and EO1050 in comparison with the gap between EO1050 and EO1100 filters. The reason for this difference was that generated carrier density profile's peak had already moved from 500 µm (for RG1000) to 1.1 mm (for EO1050) below the surface. Therefore, the reduction in the impact of high surface recombination velocity on the accuracy of transient lifetime measurements was much more significant than the case when the peak moved from 1.1 mm (for EO1050) to 1.77 mm (for EO1100) below the surface. Moreover, the probability of the minority carriers diffusing out of the RF coil sensitivity range [80] to the bulk was much higher in the carrier profile generated by EO1100 than the one by EO1050. This disappearing of the excess carriers can be miscounted as carrier recombination and, consequently, lead to underestimation of minority carrier transient lifetimes when the excess carrier density photogeneration approaches the sensitivity limits.

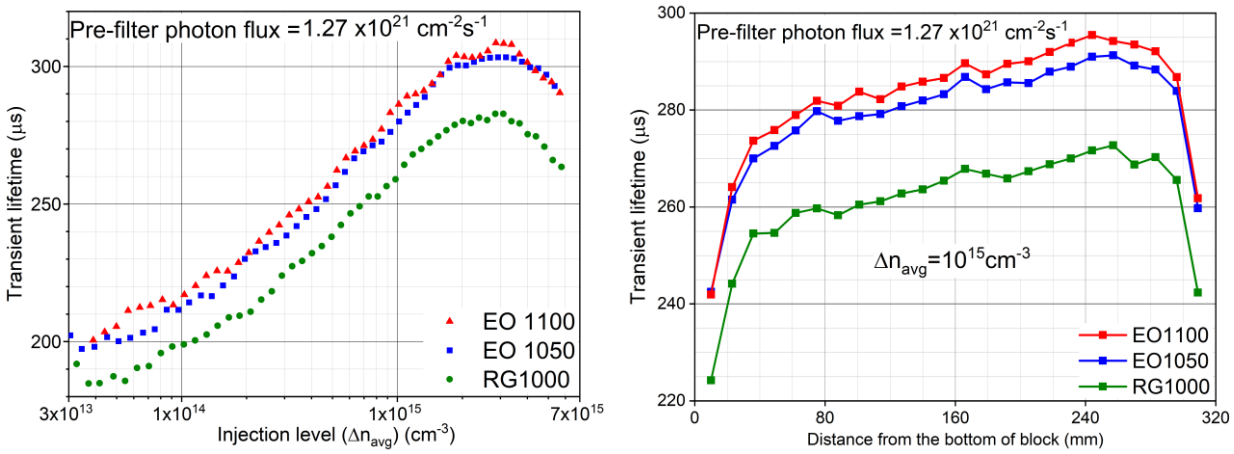

a b

Figure 5-7: (a) Measured transient lifetime as a function of injection levels for three filters. Longer cut-off wavelengths result in higher lifetimes at a given injection level. (b) Measured transient lifetime along the p-type Cz silicon block for different filters at $\Delta n_{avg} = 10^{15}$ cm^{-3}.

Figure 5-7-b represents the transient lifetime measurement results at $\Delta n_{avg} = 10^{15}$ cm^{-3} along the p-type Cz silicon block performed by three filters. The measurements results confirmed

approximately 10% increase in the reported transient lifetimes when the standard RG1000 is replaced by EO1100. However, the measured transient lifetimes improvement when the EO1050 was replaced by the EO1100 was rather insignificant. Therefore, there is a trade-off between such an imperceptible improvement at the cost of 40% reduction in photon flux on the samples' illumination as illustrated in figure 5-3-b.

5.5 Summary

It has been shown that reducing the impact of high surface recombination velocity is the key to increase reported transient lifetime towards the actual bulk lifetime. As shown, the impact of high SRV reduced as time elapsed after the flash was terminated as there was no photogeneration in the sample. The simulation results demonstrated that higher light source intensities to generate higher initial injection levels improves the measurement results, performed at a given injection level, which was confirmed by the experimental results.

The simulation results also proposed an improvement in transient lifetime measurements with deeper photogeneration via filters with longer cut-off wavelengths. The measurement results confirmed approximately 10% increase after replacing the standard RG1000 filter with a gradual cut-off wavelength at 1000 nm in comparison with the EO1100 filter with the sharp cut-off at 1100 nm.

Chapter 6: Quasi-Steady-State Photoconductance Bulk Lifetime Measurements on Silicon Ingots with Deeper Photogeneration

6.1 Introduction

One of the advantages of early material characterisation on silicon blocks and ingots is that there is no need for surface treatments or passivation prior to the lifetime measurements. As mentioned before (figure 2-4), such an as-cut surface has defect states continuously distributed within the bandgap introducing a high surface recombination velocity. The impact of such a high SRV is more significant in quasi-steady state photoconductance measurement in comparison to transient photoconductance decay. The reason behind this, as shown in the fourth chapter, is that the minority carrier diffusion into the surface reduces as time elapses after the light source is terminated (figure 3-8) during transient measurements. However, due to the injection of constant photogenerated carriers into the sample in QSS conditions, there is a high constant carrier diffusion towards the surface. As shown already, photogeneration by filters with longer cut-off wavelengths shift the excess carrier profile peak further from the surface, and so fewer carriers will diffuse to the surface to recombine [78, 97, 103].

As illustrated in equation 3-1, the accurate determination of the total photogeneration in the sample is a crucial parameter for the determination of the minority carrier lifetime [7, 11]. The need to determine cumulative photogeneration adds constraints to the QSSPC measurements in comparison with the transient technique. A solar cell is used in the BCT-400 system from Sinton Instruments to measure the total photon flux on a sample during the QSSPC lifetime

measurements. Therefore, the EQE of the reference cell adds uncertainty to the photogeneration determination and, consequently, QSSPC lifetime measurements.

In this chapter, the possibilities of improving QSSPC measurements by deeper photogeneration is investigated with the simulation tool, and the results are evaluated by measurement results. As the transient measurement results are more reliable due to absence of the above-mentioned complications, the QSSPC and transient modes from every filter are compared to assess the accuracy of the QSSPC measurement results provided by each filter.

6.2 Simulation

Different optical filters are used in this section for photogeneration at various depths. As a BCT-400 from Sinton Instrument is used for all measurements here, the optical specifications of such a system with different filters are explained first. Constraints imposed by the tool depth sensitivity and the reference cell EQE on how deep the generation profile can be in practice are crucial factors to identify the most suitable filter. Then the generation and carrier profiles from the filters are simulated to compare the determined lifetimes using each filter. In the last stage, before proceeding to the measurement section, a detailed explanation on accurate determination of the total photogeneration is provided.

6.2.1 Optical specifications

Figure 6-1 shows the spectrum of the X5dR Q xenon flash and the EQE of the reference cell used in the BCT-400 tool, along with the measured transmission functions for the four filters used in simulations and measurements in this work. The filters are two IR-Pass Schott glass 850 and 1000 nm filters (RG850 and RG1000), of which the RG1000 is the standard filter currently used with the BCT-400 tool, as well as two high-performance OD-4 long-pass filters from Edmund

Optics with sharp cut-off wavelengths at 1050 nm (EO1050) and 1100 nm (EO1100) respectively. As mentioned before, the two EO filters have sharper edges and greater transmission at longer wavelengths in comparison with the RG850 and RG1000. Due to the elimination of photons with shallower absorption coefficients, excess carrier densities generated by these filters are shifted deeper in the bulk. However, it will also tend to decrease the maximum injection level created in the sample due to the lower total photon flux [104].

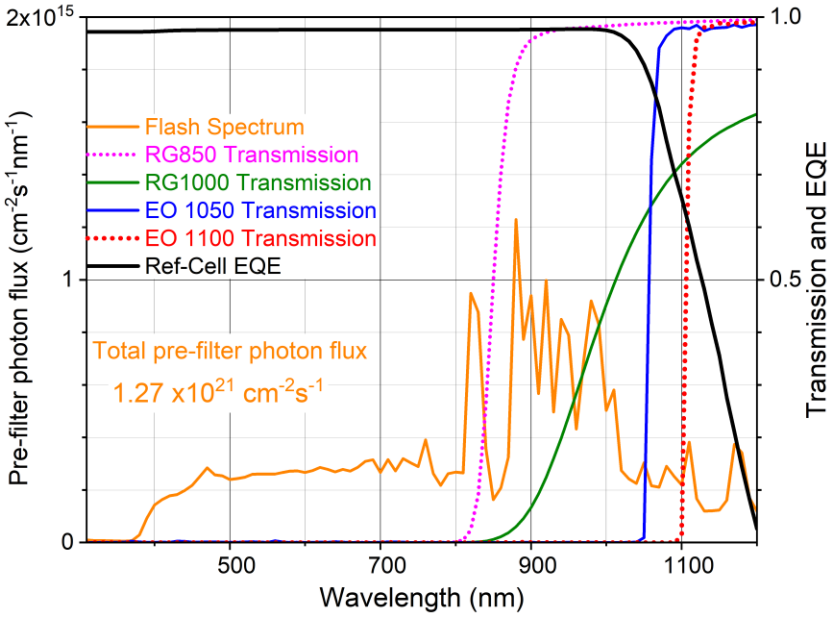

Figure 6-1: Xenon flash spectrum, reference cell EQE and measured transmission functions for 4 filters.

As can be seen in figure 6-1, a longer cut-off wavelength pushes the photogeneration spectrum closer to the part of the spectrum in which the reference cell EQE exhibits a sharply decreasing tail [104]. This introduces uncertainty to the determination of the cumulative photogenerated carriers which consequently leads to uncertainty in the QSSPC carrier lifetime determination. As figure 6-1 shows, the EO1050 transmission spectrum starts at the very beginning of the mentioned decreasing tail introducing less uncertainty in comparison with the EO1100. However, the severity

of this uncertainty for the EO1100 filter makes the g_{cum} determination quite unreliable. Thus, despite being the favourable filter for the transient measurement, the EO1100 is not considered a suitable choice to improve the accuracy of lifetime measurements in the QSS mode. This conclusion is further supported when the calculations are performed to determine the amount of light absorbed by samples during the QSSPC measurements.

Swirhun *et al.* [80] previously showed that pushing the photogeneration deeper in the bulk by using the RG1000 instead of the RG850 significantly improved the accuracy of the QSSPC lifetime measurements. In this work, the RG850 is also used in simulation to confirm the results in [80] as well as being able to directly compare further improvement by filters with a cut-off wavelength longer than 1000 nm. However, in the experimental phase, the performances of the RG1000 and the EO1050 are compared to select the best filter for the QSS measurement.

6.2.2 Generation and carrier densities profiles

Figure 6-2-a shows the photogeneration profiles required to generate an average excess carrier density of $\Delta n_{avg-sensed}$ = 10^{15} cm^{-3} in a p-type semi-infinite thick sample with an SRV = 10^{6} cms^{-1} for an unpassivated surface for each filter [104]. The generated excess carrier density profiles corresponding to each filter are illustrated in figure 6-2-b along with the excess carrier profiles which are sensed by the tool sensor. As a result of longer cut-off wavelengths, the carrier profiles become broader with higher peaks more distant from the surface. The reason for the higher peaks for deeper generation is that the coil sensitivity decays with depth, and the carriers closer to the surface have a significantly higher weight when Δn_{avg} is being calculated as discussed in [11]. Therefore, a higher initial pre-filter photon flux is needed for the filters with longer cut-off wavelengths to generate the same average injection level to be sensed ($\Delta n_{avg-sensed}$ = 10^{15} cm^{-3}).

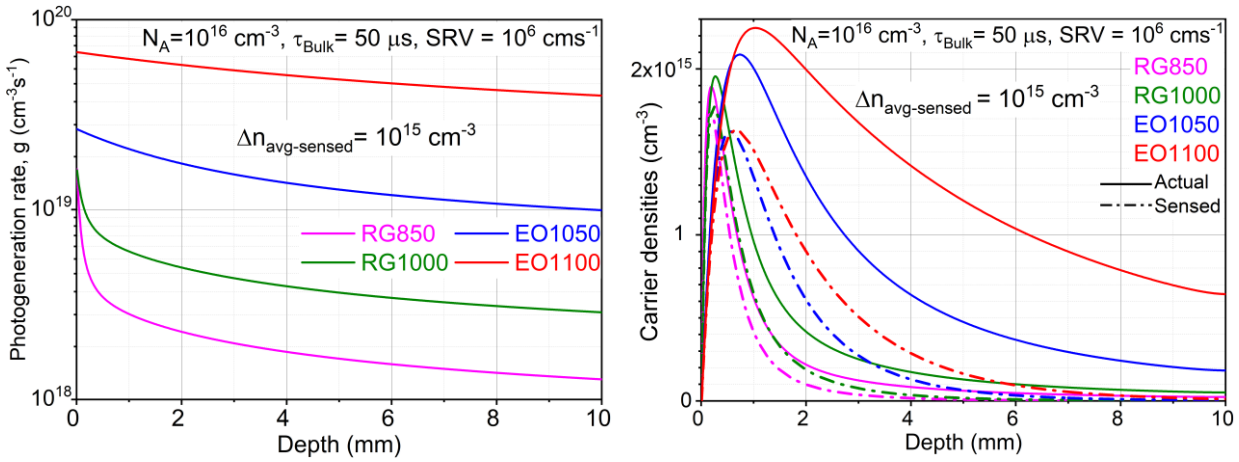

a b

Figure 6-2: (a) Typical generation profiles for 4 filters to generate $\Delta n_{avg-sensed}$ = 10^{15} cm^{-3}, and (b) Excess carrier density profiles at $\Delta n_{avg-sensed}$ = 10^{15} cm^{-3} under steady-state conditions, as functions of sample depth for the four filters.

Practically, this reduces the maximum injection levels that can be reached when the EO1050 and EO1100 are used. However, this is not practically a disadvantage in ingot and block measurements, as high injection measurements such as required for J_0 measurements on wafers are not performed on ingots.

As can be seen in figure 6-2-b, there is a relatively significant difference between the generated carrier density and the sensed one with the coil sensor when the EO1100 filter is used. Such a deep carrier profile approaches the tool sensitivity limits which makes the measurements unreliable. This is another reason not to consider the EO1100 as a suitable choice for the QSSPC measurements and, therefore, it is not included in the simulation of the QSSPC lifetimes determination [104].

6.2.3 Lifetime determination

The QSSPC lifetime measurements are simulated using the simulation tool for various bulk lifetimes in a p-type silicon block with the three filters. As discussed before, in a sample with an

ideal passivated surface the effective lifetimes are expected to be equal to the input bulk lifetime ($\tau_{effective}$= τ_{bulk}) in the absence of any surface recombination (SRV = 0). However, an as-cut silicon surface introduces a large deviation between the effective and the bulk lifetime.

As illustrated in figure 6-3, the smallest deviation amongst the three filters between the simulated effective lifetimes and the bulk lifetimes at all lifetimes range belongs to the EO1050. In contrast, as Swirhun *et al.* [80] showed, the lowest effective lifetimes are reported by the RG850 with the shallowest generation profile as more excess minority carriers diffuse to and recombine at the surface before recombining in bulk [104].

For bulk lifetimes lower than 30 μs, the EO1050 and RG1000 filters are relatively close in performance as the low lifetime minority carriers have quite short diffusion lengths. Therefore, more of the excess carriers recombine in bulk before reaching the surface. However, the advantage of deeper generation profiles appears at a bulk lifetime of around 50 μs, at which the standard RG1000 filter demonstrates more deviation in the effective lifetime in comparison with EO1050. This deviation increases for longer bulk lifetimes for all filters because the effect of the high SRV, particularly for the RG filters, becomes more significant as the bulk diffusion length increases. The higher reported effective lifetime means the transfer function has less to do to map the measured lifetimes, $\tau_{effective}$, to the QSS-bulk lifetimes, $\tau_{QSS-bulk}$.

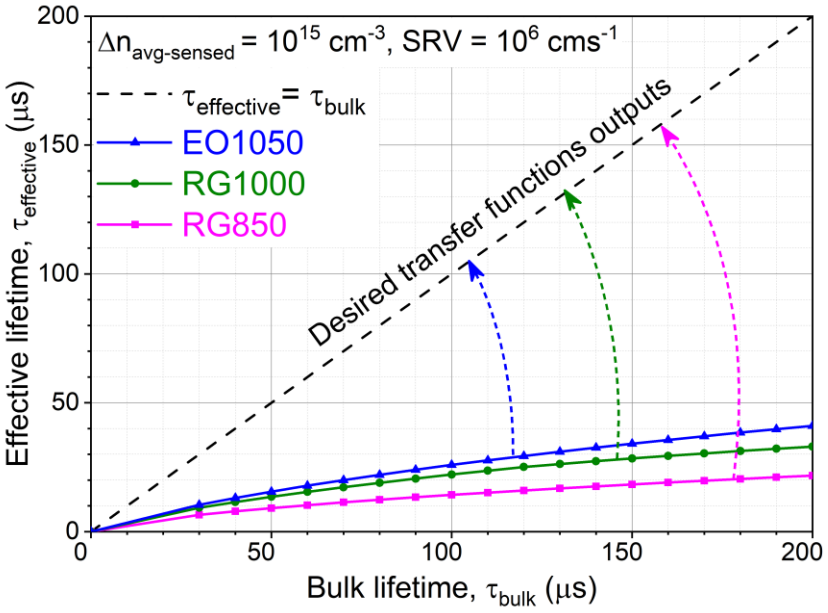

Figure 6-3: Simulated effective lifetimes as functions of bulk lifetimes for three filters (symbol-lines). The dashed line indicates equality between the effective lifetime and the bulk lifetime.

6.2.4 Optical constant

As mentioned before, the light incident on the sample is measured by the reference cell with the EQE shown in figure 6-1 during the QSSPC measurements. The measured flux is then used to determine the cumulative photogeneration in the sample to calculate the minority carrier lifetimes from equation 3-1. Because of the reference cell EQE, as well as light reflection from the sample as-cut surface, there is a discrepancy between the incident light measured by the reference cell and the photogeneration in the sample [104].

Therefore, a coefficient is required to be defined in the QSSPC measurements to account for the such a discrepancy. The coefficient is called the optical constant and is to be set during the measurements, and is defined as:

$$Optical\ constant = \frac{Total\ effective\ \ absorption\ in\ the\ sample}{Total\ absorption\ in\ the\ reference\ cell} \qquad 6\text{-}1$$

The total photon absorption by the reference cell can be determined from the flash spectrum, filters transmissions and the reference cell EQE all illustrated in figure 6-1. However, the total effective photon absorption by the sample needs to be determined considering the sample surface reflection as well as the sample depth at which the photon absorption impact the lifetime measurements.

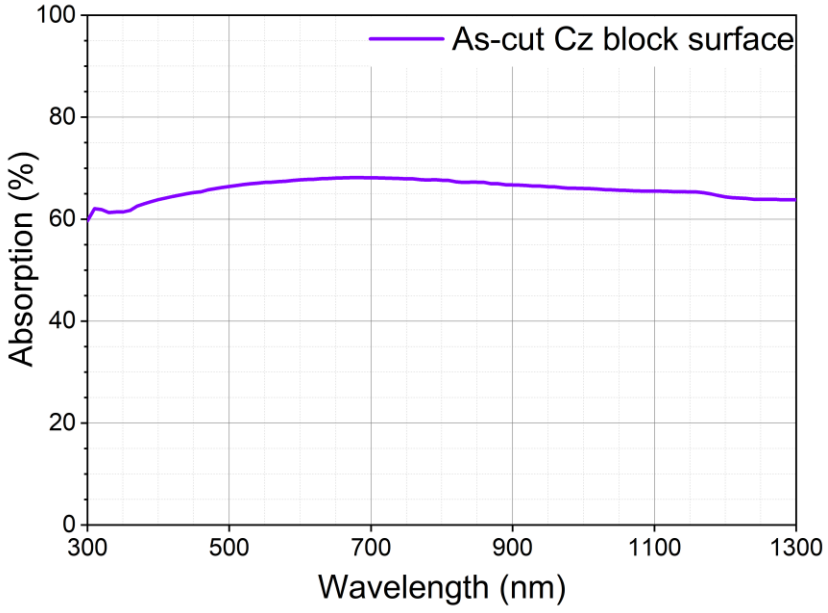

Figure 6-4: Absorption coefficient of the Cz p-type silicon block as-cut surface measured by a Lambda 1050 UV/VIS/NIR spectrophotometer from PerkinElmer Inc.

Figure 6-4 shows the surface absorption of the Cz p-type silicon block used in this section measured by a Lambda 1050 UV/VIS/NIR spectrophotometer from PerkinElmer Inc as a function of wavelengths. The total photons absorbed by the sample can be calculated from the flash spectrum and the filter transmissions in figure 6-1 and the absorption measured in figure 6-4. As

mentioned, total effective photons are the photons absorbed by the sample mostly in the sensed region which affects QSSPC lifetime measurements but not far below the sample. Therefore, the depth assumption is important in determining the optical constant, particularly for the filters with longer cut-off wavelengths due to their larger proportion of photons with low absorption coefficients.

The calculated optical constants for each filter are shown in figure 6-5 as a function of depth for a standard '6 inch' rectangular silicon block with 156 mm thickness. The figure shows an almost flat optical constant as a function of depth for RG850 as most of the spectrum is short wavelengths photons absorbed just below the surface. Due to its deeper generation profile, RG1000 displays an increase as a function of depth below 5 mm and then a gradual increase afterward as there is little photogeneration beyond that depth. A similar increase is observed for EO1050 for depths greater than 40 mm. However, because of the relatively deep generation profile of EO1100 as well as the sharply decreasing tail in the EQE of the reference cell in that spectral range, the EO1100 optical constant varies strongly as a function of depth in the range up to 150 mm [104].

In principle, such a remarkable dependency on the sample depth could result in measured effective lifetimes that are less accurate, due to a higher sensitivity to the choice of the optical factor. Hence, there exists a trade-off between reducing the impact of the high SRV with deeper generation and the consequent uncertainty on the optical constant value.

Due to uncertainty in the reference cell EQE in the EO1100 filtered spectrum, the determined cumulative photogeneration is quite unreliable. Thus, the EO1100 filter is not a suitable choice for improved QSS lifetime measurements.

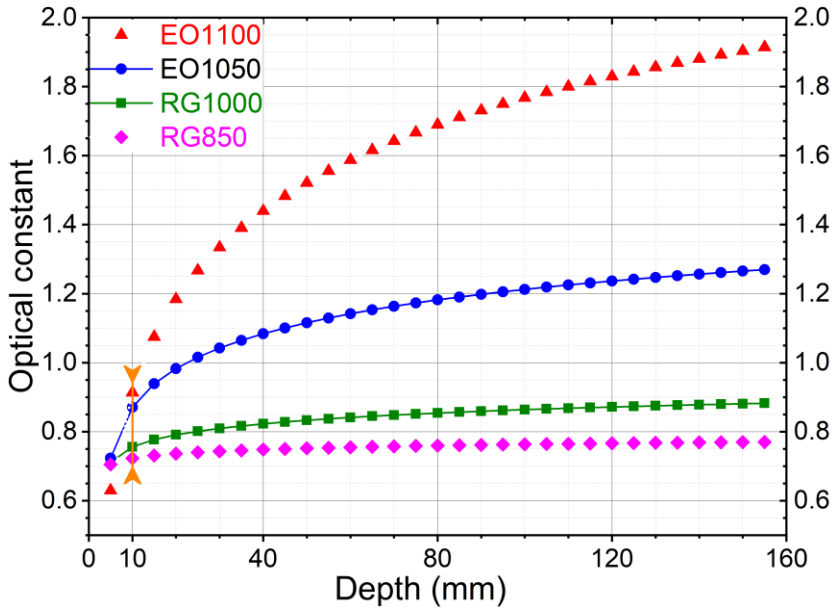

Figure 6-5: Calculated optical constants for the four filters as a function of depth for a sample with an unpassivated as-cut surface measured by the BCT-400 system from Sinton Instruments.

There are several parameters to consider obtaining a proper depth for the suitable optical constant value to select during lifetime measurements, to ensure that the results are not overly affected by generation and recombination beyond that depth. The first is the tool sensitivity depth and its decay constant, which for the Sinton BCT-400 that is used in this work is about 2.5 mm, as discussed in detail in [80]. The carrier diffusion length is also an important factor as the lifetime measurement is affected by carriers diffusing into and out of the tool sensitivity range, which can cause miscounting of carrier generation and recombination. As the QSS conditions are generally only valid for lifetimes below 200 μs, the maximum expected carrier diffusion length is less than 1 mm to consider for the sample depth assumption. Moreover, as discussed above, the rate at which the optical constant value changes as a function of depth can also influence the results.

Considering the above factors, a depth of 10 mm was chosen in this work to calculate the optical constant values for the filters, as any generation and recombination beyond that depth will certainly not have any effect on the measurement results in this work.

6.3 Measurements

The RG850 was not used in the measurements as the simulation section here as well as Swirhun *et al*. [80] have already shown the improvement of QSS lifetime measurement after replacing it with the RG1000. The reference cell EQE and the EO1100 transmission function in figure 6-1 showed uncertainties introduced in the determination of cumulative photogeneration when the EO1100 is used. In addition, the photogeneration beyond the coil sensitivity depth by the EO11000 makes the optical constant calculation highly sensitive which adds more uncertainty in the QSS measurements. Thus, the lifetime measurements were performed on a Cz block in both QSS and transient modes with the RG1000 and the EO 1050 filters to evaluate the simulation results and select the better choice for the QSS lifetime measurements.

The sample was a rectangular block cut from a standard industrial Cz p-type monocrystalline silicon ingot, with a square base of 156×156 mm and a height of 320 mm. The lifetime measurements were performed at one fixed point (10 mm from the bottom of the block) with two filters to compare the lifetime as a function of injection level. During the QSSPC measurements, the optical constant was set to 0.76 and 0.87 for the RG1000 and the EO1050 respectively, which corresponds to absorption up to a depth of 10 mm in the block.

The QSS measurement results are shown in figure 6-6-a which clearly shows that the measured lifetimes with the EO1050 with the longer cut-off wavelength are higher at all injection levels. Removing the short wavelengths photons from the flash results in the slightly lower maximum injection level when the EO1050 filter is used [78].

As mentioned before, the transient photoconductance decay technique is less prone to the effects of high SRV, and the measured lifetimes are expected to be closer to the actual bulk lifetime. The transient lifetime measurement results are also more reliable as there is no need to

determine the cumulative photogeneration which adds more uncertainty to the measurement. The lifetimes were measured in the transient mode, $\tau_{transient}$, at the same point on the block with both filters and the reported values were compared with the QSS mode. The transient measurement results are presented in figure 6-6-b for which the EO1050 filter still demonstrates a better performance. The transient lifetimes are in 160-170 µs ranges whereas the QSS effective lifetimes varied from 20 to 35 µs at $\Delta n_{avg} = 10^{15}$ cm^{-3}.

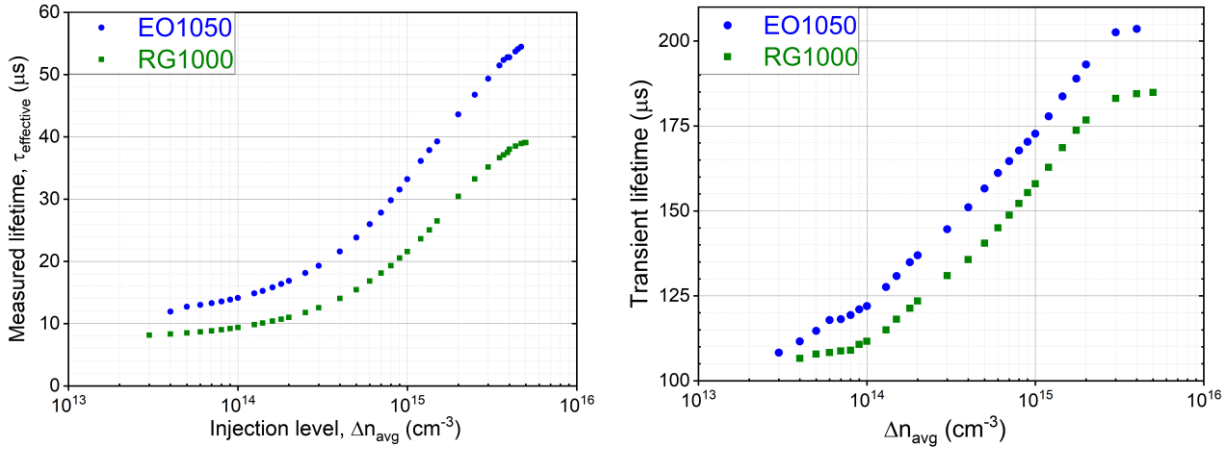

A b

Figure 6-6: (a) Measured QSS lifetimes and (b) Transient lifetimes, as a function of injection level for the filters on a standard industrial Cz p-type monocrystalline silicon block. The maximum injection level is slightly lower when the EO1050 filter is used.

Such a large discrepancy shows the sensitivity of the QSS method to the high surface recombination velocity resulting in the significantly lower measured effective lifetime than the actual bulk lifetime.

Therefore, as discussed in the simulation chapter, a transfer function removes the effect of high SRV to report a QSS-bulk lifetime ($\tau_{QSS-bulk}$) having a lower discrepancy with the transient lifetime. As illustrated in figure 6-3, the function should transfer $\tau_{effective}$ value to a QSS-bulk lifetime ($\tau_{QSS-bulk}$) which should ideally be equal to the actual bulk lifetime,τ_{bulk}.

The measured effective lifetimes, $\tau_{effective}$, the QSS-bulk lifetimes, $\tau_{QSS-bulk}$, resulted from the transfer function in figure 6-3, and transient lifetimes, $\tau_{transient}$, for two filters are presented in figure 6-7. As mentioned before, the transient lifetimes are used as a benchmark here to evaluate the lifetime results in the QSS mode.

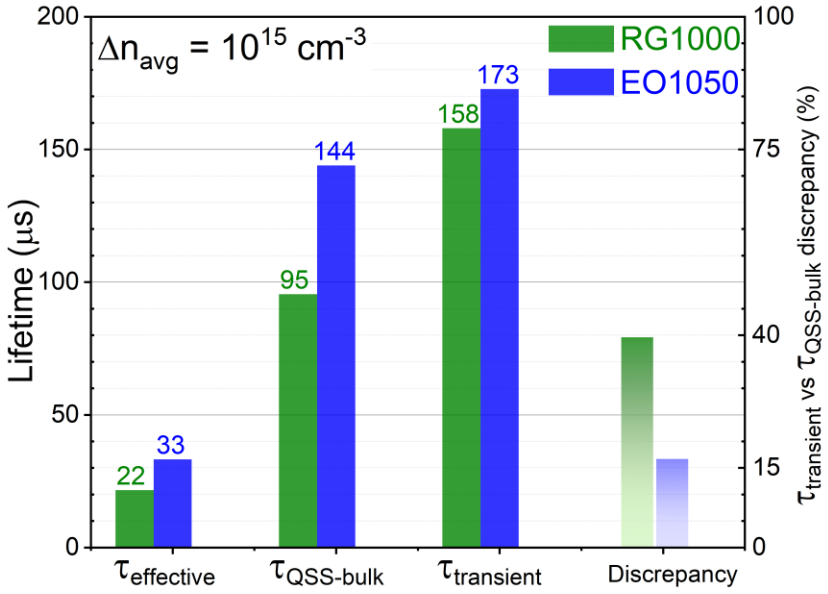

Figure 6-7: The effective, QSS-bulk, transient lifetimes and discrepancy for different filters at $\Delta n_{avg-sensed} = 10^{15}$ cm^{-3}.

In order to quantitively compare the performance of two filters, a discrepancy factor is defined between the transient lifetime and QSS-bulk lifetime to present the accuracy of each filter in reporting the QSS minority carrier lifetime. The discrepancy is defined as the difference between the transient lifetime and the QSS-bulk lifetime presented as the percentage of the transient lifetime.

The discrepancy values for both filters are also presented in figure 6-7. As shown, the current standard RG1000 filters results in 40% discrepancy between the transient and the QSS-bulk lifetime. Such a significant difference is mainly caused by the massive impact of high surface

recombination velocity on the shallower excess carrier density profile. However, the distant carrier profile peak from the surface because of the deeper photogeneration by the EO1050, significantly dropped the discrepancy to around 15% for this filter.

Such a significant improvement in the discrepancy between the transient lifetime and QSS-bulk lifetime as well as the lower effects from the transfer function on the QSS-bulk lifetime make the EO1050 a better choice for further improvement of the QSSPC lifetime measurement.

6.4 Summary

This chapter demonstrated improved QSSPC effective lifetime measurements, particularly in the lifetime range above 50 μs, on silicon blocks. The simulations showed the deeper photo-generation profiles of the filters with longer cut-off wavelengths reduced the impact of surface recombination in this lifetime range. Such a reduction leads to less reliance on the transfer function to estimate the bulk lifetimes in comparison with the standard filter.

However, there is a corresponding increase in the uncertainty of determination of the cumulative photogeneration due to the reference cell EQE in the longer-range wavelengths. Moreover, there is a significant dependency on selecting the proper value for optical constant due to carrier generation beyond the coil sensitivity depth. Such consequences counteract the benefits of reduced surface recombination impact and make the EO1100 filter an unsuitable option for QSS measurements.

The comparison between the results from the QSSPC method and transient photoconductance decay method, revealed a reasonable agreement between the results using the EO1050 filter, reducing the discrepancy to around 15%. In summary, the use of the EO1050 filter is a suitable choice to reduce the uncertainty of the estimated bulk lifetime, due to a decreased reliance on the transfer function, while still allowing sufficiently accurate estimation of the optical constant [104].

Chapter 7: Conclusion and future work

This thesis studied carrier lifetime measurements by photoconductance techniques in crystalline silicon ingots in both the quasi-steady state and the transient decay modes. The simulation tool is developed in MATLAB based on various studies [7, 11, 80, 102] and enabled us to simulate the QSS and the transient photoconductance lifetime measurements in thick silicon samples. Several parameters that can affect lifetime measurement results are embedded in the model and can be defined as desired. These parameters include, but are not limited to, illumination intensity and spectrum, injection level at which measurements are performed as well as the specifications of measurement instruments.

Moreover, the lifetime measurements can be simulated in detail for various types of silicon material (acceptor/donor dopants with different densities) with different properties. Various common impurities existing in the PV grade crystalline silicon with different concentrations as well as sample surfaces with any given surface recombination velocity are also modifiable as input variables for simulations.

The simulation tool is used then to study the accuracy of interstitial iron measurements on boron-doped crystalline silicon blocks by quasi-steady-state photoconductance. Sets of simulations were performed to calculate the iron concentrations from the differences between the simulated lifetimes before and after dissociating iron-boron pairs in a block. The calculated results were then compared to the initial defined iron concentrations (as the simulation input) to evaluate the accuracy of the model to determination of dissolved iron concentration. The simulation results were later confirmed by experimental results where the measured $[Fe_i]$ at different heights of a standard p-type mc-Si block were compared to the values measured in wafers of corresponding heights from an adjacent block in the same ingot [10]. In a separate work, $[Fe_i]$ in a p-type

multicrystalline silicon block are extracted with the photoluminescence intensity ratio imaging technique as well as extracted and corrected with the QSSPC. The results from the both methods on different heights showed good agreements with the extracted [Fe_i] of wafers from the same heights of the same block after wafering [93].

It was shown that the effect of a high surface recombination velocity on the accuracy of the transient photoconductance lifetime measurements is reduced as time elapses after termination of the light source. Therefore, a higher initial injection level or longer time waiting after the light source turned off reduces the gap between the effective measured lifetime and actual bulk lifetime. Introducing filters with longer cut-off wavelengths was also proposed to push the carrier density profile peak more distant from the surface due to deeper photogeneration. The approach reduced the carrier diffusion to the surface and, consequently, decreased the surface recombination contribution to the effective lifetime. The lifetime measurements on a p-type Cz silicon block with three filters with increasing cut-off wavelengths confirmed the simulation results showing up to 10% improvement in the measured carrier transient lifetime [78].

The similar approach was taken to evaluate the accuracy of the lifetime measurements in QSSPC mode by deeper photogeneration. It was shown that increasing uncertainties were added when filter with longer cut-off wavelengths were used. One source of added uncertainty was the filters transmission spectrums being on the decreasing tail of the reference cell EQE which is used to determine the cumulative photogeneration during QSSPC measurements [104]. The other source of uncertainty was the deeper excess carrier density beyond the conductive sensor depth sensitivity which is used to sense the increased conductance due to illumination in samples. Therefore, there was a compromise to be made between reducing the high SRV impact and added uncertainties to determine the cumulative photogeneration and changes in samples conductance

for accurate lifetime measurement results in the QSS mode. The results showed that pushing the excess carrier profile peak deeper but not too far beyond the depth sensitivity limit increases the measured effective lifetimes and, consequently, reduces reliance on the transfer function for accurate results. The measurement results confirmed the better performance of the new filter showing a reduced gap between the QSS results and the transient results (which represents a lower bound of the actual bulk lifetime).

7.1 Future work

This study has presented a comprehensive assessment of photoconductance carrier lifetime measurement techniques on crystalline silicon ingots and bricks, in both the QSS and the transient decay modes.

As seen in chapter 4 during the cross comparison of dissolved iron measurements between the QSSPC and the photoluminescence intensity ratio imaging method, there was a gap between the lifetime measurement results by the two methods. The reason behind this was the difference between the injection levels at which each method reports the measured carrier lifetimes. The PLIR technique usually is a low injection level characterisation method and the lifetime measurements are mostly performed at $\Delta n = 10^{13}$ cm^{-3}. In contrast, the QSSPC lifetime measurements are performed at an injection level range between 10^{13}- 10^{15} cm^{-3}, with the most accurate results at higher injection levels typically at $\Delta n = 10^{15}$ cm^{-3} due to the defined transfer function. The whole range of injection levels can be studied by the QSSPC in detail to ensure a consistent accuracy exists at any given injection level as well as comprehensive cross comparison studies between the QSSPC and other methods like the PLIR.

Such a study can also reveal more details about the gap which currently exists between the QSS and the transient decay methods which was discussed in chapter 6. The QSSPC is recommended

to use for bulk lifetimes below 150 μs, the transient decay mode is typically valid for lifetimes above that range. While the two methods are not technically expected to report exactly the same results for the samples with carrier lifetime around 150 μs, the gap between two the methods can be further reduced [104].

Another study which may extend the application of the QSSPC lifetime measurement technique can be estimating the range of surface recombination velocity with reasonable approximation. As shown, photogeneration with filters with longer cut-off wavelengths push the excess carrier profile peak distant from the surface and reduce the impact of a high SRV to determine the effective lifetime. Hypothetically, changing the weight of the SRV in the effective lifetime determination in equation 2-14 should reveal more detail about the sample SRV. Several sets of simulations can be performed with a long-pass and a short-pass filters for samples with different SRVs and be repeated for different bulk lifetimes. Then, numerical analysis of the results can enable us to estimate the SRV range according to the differences between the lifetime measurements with two filters. Such information may provide a very simple and fast technique to measure SRV values.

List of publications

Publications arising from the work of this thesis:

Refereed journal papers

- M. Goodarzi, R. Sinton, and D. Macdonald, "Quasi-steady-state photoconductance bulk lifetime measurements on silicon ingots with deeper photogeneration," *AIP Advances*, vol. 9, no. 1, p. 015128, 2019.
- M. Goodarzi, R. A. Sinton, H. Jin, P. Zheng, W. Chen, Q. Wang & D. Macdonald, "Accuracy of Interstitial Iron Measurements on P-Type Multicrystalline Silicon Blocks by Quasi-Steady-State Photoconductance". *IEEE Journal of Photovoltaics*, 7(5), 1216-1223. doi:10.1109/jphotov.2017.2716785, 2017.
- D. Chung, B. Mitchell, M. Goodarzi, R. A. Sinton, D. Macdonald, and T. Trupke, "Uncertainty in photoluminescence metrology on multicrystalline silicon bricks and cross validation with wafers," *IEEE Journal of Photovoltaics*, vol. 7, no. 6, pp. 1701-1709, 2017.
- D. Chung, B. Mitchell, M. Goodarzi, C. Sun, D. Macdonald, and T. Trupke, "Bulk lifetimes up to 20 ms measured on unpassivated silicon discs using photoluminescence imaging," *IEEE Journal of Photovoltaics*, vol. 7, no. 2, pp. 444-449, 2017.

Papers presented at international conferences

- M. Goodarzi, R. A. Sinton, and D. Macdonald, "Improving transient photoconductance lifetime measurements on ingots with deeper photogeneration," in Silicon PV 2018, The 8th International Conference on Crystalline Silicon Photovoltaics, Lausanne, Switzerland, 2018, vol. 1999, no. 1, pp. 37-44: AIP Publishing, 2018.
- M. Goodarzi, R. Sinton, D. Chung, B. Mitchell, T. Trupke, and D. Macdonald, "A comparison between quasi-steady state and transient photoconductance lifetimes in silicon ingots: simulations and measurements," in 2017 IEEE 44th Photovoltaic Specialist Conference (PVSC), Washington, DC, 2017, pp. 2707-2710.
- M. Goodarzi, R. Sinton, D. Chung, B. Mitchell, T. Trupke, and D. Macdonald, "Modelling and Characterisation of Multicrystalline Silicon Blocks by Quasi-Steady-State Photoconductance," in 32nd European Photovoltaic Solar Energy Conference and Exhibition, Munich, Germany, 2016, pp. 535 - 538.

Bibliography

[1] IRENA, "Renewable Power Generation Costs in 2017," International Renewable Energy Agency, Abu Dhabi, 2018.

[2] S. Philipps, "Photovoltaics Report," Fraunhofer ISE, PSE Conferences & Consulting GmbH, 2018.

[3] A. LIU, "Precipitation and hydrogenation of Iron in multicrystalline silicon," Doctor of Philosophy, Department of Engineering, The Australian National University, Canberra, 2015.

[4] "Renewables 2018, Analysis and Forecasts to 2023," in "Market Report Series," Internationa Energy Agancy, 2018.

[5] M. Schmela, "Global Market Outlook For Solar Power / 2018 - 2022," SolarPower Europe, 2018.

[6] A. McEvoy, T. Markvart, and L. Castaner, *Practical Handbook of Photovoltaics: Fundamentals and Applications*. Elsevier Science, 2011.

[7] R. A. Sinton and A. Cuevas, "Contactless determination of current–voltage characteristics and minority-carrier lifetimes in semiconductors from quasi-steady-state photoconductance data," *Applied Physics Letters,* vol. 69, no. 17, pp. 2510-2512, 1996, doi: 10.1063/1.117723.

[8] R. A. Sinton, A. Cuevas, and M. Stuckings, "Quasi-steady-state photoconductance, a new method for solar cell material and device characterization," in *Photovoltaic Specialists Conference, 1996., Conference Record of the Twenty Fifth IEEE,* 1996: IEEE, pp. 457-460.

[9] M. Goodarzi, R. Sinton, D. Chung, B. Mitchell, T. Trupke, and D. Macdonald, "Modelling and Characterization of Multicrystalline Silicon Blocks by Quasi-Steady-State Photoconductance," in *32nd European Photovoltaic Solar Energy Conference and Exhibition*, Munich, Germany, 2016, pp. 535 - 538, doi: 10.4229/EUPVSEC20162016-2DO.4.1.

[10] M. Goodarzi *et al.*, "Accuracy of Interstitial Iron Measurements on P-Type Multicrystalline Silicon Blocks by Quasi-Steady-State Photoconductance," *IEEE Journal of Photovoltaics,* vol. 7, no. 5, pp. 1216-1223, 2017, doi: 10.1109/jphotov.2017.2716785.

[11] S. Bowden and R. A. Sinton, "Determining lifetime in silicon blocks and wafers with accurate expressions for carrier density," *Journal of Applied Physics,* vol. 102, no. 12, p. 124501, 2007, doi: 10.1063/1.2818371.

[12] R. Sinton, T. Mankad, S. Bowden, and N. Enjalbert, "Evaluating silicon blocks and ingots with quasi-steady-state lifetime measurements," in *Proceedings of the 19th European Photovoltaic Solar Energy Conference, Paris, France*, 2004, pp. 520-523.

[13] F. Schindler *et al.*, "Material limits of multicrystalline silicon from state-of-the-art photoluminescence imaging techniques," *Progress in Photovoltaics: Research and Applications,* vol. 25, no. 7, pp. 499-508, 2017, doi: 10.1002/pip.2836.

[14] B. Mitchell, T. Trupke, J. W. Weber, and J. Nyhus, "Bulk minority carrier lifetimes and doping of silicon bricks from photoluminescence intensity ratios," *Journal of Applied Physics,* vol. 109, no. 8, p. 083111, 2011, doi: 10.1063/1.3575171.

[15] J. A. Giesecke, M. C. Schubert, F. Schindler, and W. Warta, "Harmonically Modulated Luminescence: Bridging Gaps in Carrier Lifetime Metrology Across the PV Processing

Chain," *IEEE Journal of Photovoltaics*, vol. 5, no. 1, pp. 313-319, 2015, doi: 10.1109/jphotov.2014.2362304.
[16] D. Macdonald, A. Cuevas, A. Kinomura, Y. Nakano, and L. J. Geerligs, "Transition-metal profiles in a multicrystalline silicon ingot," *Journal of Applied Physics*, vol. 97, no. 3, p. 033523, 2005, doi: 10.1063/1.1845584.
[17] B. Sopori, C. Li, S. Narayanan, and D. Carlson, "Efficiency limitations of multicrystalline silicon solar cells due to defect clusters," 2005, vol. 864: MRS Proceedings, doi: 10.1557/PROC-864-E6.2.
[18] A. Istratov, H. Hieslmair, and E. Weber, "Iron and its complexes in silicon," *Applied Physics A*, vol. 69, no. 1, pp. 13-44, 1999.
[19] A. Istratov *et al.*, "Metal content of multicrystalline silicon for solar cells and its impact on minority carrier diffusion length," *Journal of Applied Physics*, vol. 94, no. 10, pp. 6552-6559, 2003, doi: https://doi.org/10.1063/1.1618912.
[20] T. Buonassisi *et al.*, "Synchrotron-based investigations of the nature and impact of iron contamination in multicrystalline silicon solar cells," *Journal of Applied Physics*, vol. 97, no. 7, p. 074901, 2005.
[21] G. Zoth and W. Bergholz, "A fast, preparation-free method to detect iron in silicon," *Journal of Applied Physics*, vol. 67, no. 11, pp. 6764-6771, 1990.
[22] D. H. Macdonald, L. J. Geerligs, and A. Azzizi, "Iron detection in crystalline silicon by carrier lifetime measurements for arbitrary injection and doping," *Journal of Applied Physics*, vol. 95, no. 3, pp. 1021-1028, 2004, doi: 10.1063/1.1637136.
[23] S. Rein, *Lifetime spectroscopy: a method of defect characterization in silicon for photovoltaic applications. 2005*, 1 ed. (Springer Series in Materials Science, no. 85). 2005, p. 489.
[24] R. Nelson and R. Sobers, "Minority-carrier lifetimes and internal quantum efficiency of surface-free GaAs," *Journal of Applied Physics*, vol. 49, no. 12, pp. 6103-6108, 1978.
[25] A. Hangleiter and R. Hacker, "Enhancement of band-to-band Auger recombination by electron-hole correlations," *Phys Rev Lett*, vol. 65, no. 2, pp. 215-218, Jul 9 1990, doi: 10.1103/PhysRevLett.65.215.
[26] A. Beattie and P. Landsberg, "Auger effect in semiconductors," *Proc. R. Soc. Lond. A*, vol. 249, no. 1256, pp. 16-29, 1959.
[27] P. T. Landsberg, *Recombination in Semiconductors*. Cambridge University Press, 2003.
[28] S. Rein, T. Rehrl, W. Warta, and S. J. J. o. A. P. Glunz, "Lifetime spectroscopy for defect characterization: Systematic analysis of the possibilities and restrictions," vol. 91, no. 4, pp. 2059-2070, 2002.
[29] J. Dziewior and W. Schmid, "Auger coefficients for highly doped and highly excited silicon," *Applied Physics Letters*, vol. 31, no. 5, pp. 346-348, 1977, doi: 10.1063/1.89694.
[30] A. Richter, S. W. Glunz, F. Werner, J. Schmidt, and A. Cuevas, "Improved quantitative description of Auger recombination in crystalline silicon," *Physical Review B*, vol. 86, no. 16, 2012, doi: 10.1103/PhysRevB.86.165202.
[31] R. A. Sinton and R. M. Swanson, "Recombination in highly injected silicon," *IEEE Transactions on Electron Devices*, vol. 34, no. 6, pp. 1380-1389, 1987.
[32] P. P. Altermatt, J. Schmidt, G. Heiser, and A. G. Aberle, "Assessment and parameterisation of Coulomb-enhanced Auger recombination coefficients in lowly injected crystalline silicon," *Journal of applied physics*, vol. 82, no. 10, pp. 4938-4944, 1997.

[33] A. Hangleiter and R. Häcker, "Enhancement of band-to-band Auger recombination by electron-hole correlations," *Physical Review Letters,* vol. 65, no. 2, p. 215, 1990.
[34] D. Laks, G. Neumark, and S. Pantelides, "Accurate interband-Auger-recombination rates in silicon," *Physical Review B,* vol. 42, no. 8, p. 5176, 1990.
[35] M. Govoni, I. Marri, and S. Ossicini, "Auger recombination in Si and GaAs semiconductors: Ab initio results," *Physical Review B,* vol. 84, no. 7, p. 075215, 2011.
[36] M. J. Kerr and A. Cuevas, "General parameterization of Auger recombination in crystalline silicon," *Journal of Applied Physics,* vol. 91, no. 4, pp. 2473-2480, 2002.
[37] J. Nelson, *The physics of solar cells*. World Scientific Publishing Company, 2003.
[38] H. C. Sio, "Carrier Recombination in Multicrystalline Silicon: A Study using Photoluminescence Imaging," Doctor of Philosophy, Department of Engineering, The Australian National University, Canberra, 2015.
[39] D. K. Schroder, *Semiconductor material and device characterization*. John Wiley & Sons, 2006.
[40] M. A. Green, *Solar cells: operating principles, technology, and system applications*. University of New South Wales, 1998, p. 269.
[41] W. Shockley and W. Read Jr, "Statistics of the recombinations of holes and electrons," *Physical review,* vol. 87, no. 5, p. 835, 1952.
[42] R. N. Hall, "Electron-hole recombination in germanium," *Physical review,* vol. 87, no. 2, p. 387, 1952.
[43] A. Reinders, P. Verlinden, W. van Sark, and A. Freundlich, *Photovoltaic Solar Energy: From Fundamentals to Applications*. Wiley, 2017.
[44] A. G. Aberle, *Crystalline silicon solar cells : advanced surface passivation and analysis*. Sydney Centre for Photovoltaic Engineering, University of New South Wales, 1999, p. 335.
[45] L. Kronik and Y. Shapira, "Surface photovoltage phenomena: theory, experiment, and applications," *Surface science reports,* vol. 37, no. 1-5, pp. 1-206, 1999.
[46] L. Kronik and Y. Shapira, "Surface photovoltage spectroscopy of semiconductor structures: at the crossroads of physics, chemistry and electrical engineering," *Surface and Interface Analysis: An International Journal devoted to the development and application of techniques for the analysis of surfaces, interfaces and thin films,* vol. 31, no. 10, pp. 954-965, 2001.
[47] A. Shah *et al.,* "Material and solar cell research in microcrystalline silicon," *Solar Energy Materials and Solar Cells,* vol. 78, no. 1-4, pp. 469-491, 2003.
[48] Y. Zhang *et al.,* "Surface photovoltage characterization of a ZnO nanowire array/CdS quantum dot heterogeneous film and its application for photovoltaic devices," *Nanotechnology,* vol. 20, no. 15, p. 155707, 2009.
[49] S. Pizzini, *Advanced silicon materials for photovoltaic applications*. John Wiley & Sons, 2012.
[50] L. Votoček and J. Toušek, "Surface Photovoltaic Effect and Its Applications to Si Wafers and Monocrystalline Si Solar Cells Diagnostics," in *WDS*, 2005, vol. 5, pp. 595-600.
[51] L. L. Kazmerski, "Photovoltaics characterization: A survey of diagnostic measurements," *Journal of materials research,* vol. 13, no. 10, pp. 2684-2708, 1998.
[52] W. Shockley and H. J. Queisser, "Detailed Balance Limit of Efficiency of p-n Junction Solar Cells," *Journal of Applied Physics,* vol. 32, no. 3, pp. 510-519, 1961, doi: 10.1063/1.1736034.

[53] D. Cavalcoli, B. Fraboni, and A. Cavallini, "Surface photovoltage spectroscopy analyses of Cd 1− x Zn x Te," *Journal of Applied Physics,* vol. 103, no. 4, p. 043713, 2008.
[54] T. Wilson and E. McCabe, "Distribution of charge carriers generated in a semiconductor by a focused convergent light beam," *Journal of applied physics,* vol. 59, no. 8, pp. 2638-2642, 1986.
[55] V. I. Orlov, O. V. Feklisova, and E. B. Yakimov, "A comparison of EBIC, LBIC and XBIC methods as tools for multicrystalline Si characterization," in *Solid State Phenomena*, 2014, vol. 205: Trans Tech Publ, pp. 142-147.
[56] C. R. Brundle, C. A. Evans, and S. Wilson, *Encyclopedia of Materials Characterization: Surfaces, Interfaces, Thin Films*. Butterworth-Heinemann, 1992.
[57] C. Donolato, "Beam induced current characterization in polycrystalline semiconductors," in *Polycrystalline Semiconductors*: Springer, 1985, pp. 138-154.
[58] P. Würfel and U. Würfel, *Physics of Solar Cells: From Basic Principles to Advanced Concepts*. Wiley, 2016.
[59] E. Yakimov and V. Orlov, "Defect detection in solar cells via electroluminescence, LBIC, and EBIC methods," *Journal of Surface Investigation. X-ray, Synchrotron and Neutron Techniques,* vol. 8, no. 5, pp. 839-842, 2014.
[60] T. Trupke, R. Bardos, M. Schubert, and W. Warta, "Photoluminescence imaging of silicon wafers," *Applied Physics Letters,* vol. 89, no. 4, p. 044107, 2006.
[61] T. Trupke, R. A. Bardos, M. D. Abbott, F. Chen, J. Cotter, and A. Lorenz, "Fast photoluminescence imaging of silicon wafers," in *IEEE 4th World Conference on Photovoltaic Energy Conference*, Waikoloa, USA, 2006, vol. 1, pp. 928-931.
[62] P. Würfel, *Physics of Solar Cells: From Principles to New Concepts*. Wiley, 2005.
[63] T. Trupke, J. Nyhus, R. A. Sinton, and J. Weber, "Photoluminescence imaging on silicon bricks," presented at the 24th European Photovoltaic Solar Energy Conference, Hamburg, Germany, 2009.
[64] P. Würfel, T. Trupke, T. Puzzer, E. Schäffer, W. Warta, and S. Glunz, "Diffusion lengths of silicon solar cells from luminescence images," *Journal of Applied Physics,* vol. 101, no. 12, p. 123110, 2007.
[65] S. Herlufsen, K. Bothe, J. Schmidt, R. Brendel, and S. Siegmund, "Dynamic photoluminescence lifetime imaging of multicrystalline silicon bricks," *Solar Energy Materials and Solar Cells,* vol. 106, pp. 42-46, 2012, doi: 10.1016/j.solmat.2012.06.002.
[66] D. T. Stevenson and R. J. J. J. o. A. P. Keyes, "Measurement of carrier lifetimes in germanium and silicon," vol. 26, no. 2, pp. 190-195, 1955.
[67] S. Deb and B. Nag, "Measurement of lifetime of carriers in semiconductors through microwave reflection," *Journal of Applied Physics,* vol. 33, no. 4, pp. 1604-1604, 1962.
[68] M. Kunst and G. Beck, "The study of charge carrier kinetics in semiconductors by microwave conductivity measurements," *Journal of Applied Physics,* vol. 60, no. 10, pp. 3558-3566, 1986.
[69] M. Schöfthaler and R. Brendel, "Sensitivity and transient response of microwave reflection measurements," *Journal of Applied Physics,* vol. 77, no. 7, pp. 3162-3173, 1995, doi: 10.1063/1.358670.
[70] G. Miller, D. Robinson, and J. Wiley, "Contactless measurement of semiconductor conductivity by radio frequency-free-carrier power absorption," *Rev. Sci. Instrum,* vol. 47, no. 7, pp. 799-805, 1976.
[71] R. H. Bube, *Photoconductivity of solids*. New York: Wiley (in English), 1960.

[72] H. Nagel, C. Berge, and A. G. Aberle, "Generalized analysis of quasi-steady-state and quasi-transient measurements of carrier lifetimes in semiconductors," *Journal of Applied Physics,* vol. 86, no. 11, pp. 6218-6221, 1999.
[73] D. Macdonald and A. Cuevas, "Trapping of minority carriers in multicrystalline silicon," *Applied Physics Letters,* vol. 74, no. 12, pp. 1710-1712, 1999.
[74] R. K. Ahrenkiel, B. M. Keyes, and D. L. Levi, "Recombination processes in polycristalline photovoltaic materials," in *13th European Photovoltaic Solar Energy Conference, International Conference, Oct 23-27, 1995.*, Nice, France., 1995, vol. 1:

H.S. Stephens & Associates, pp. 914-917.
[75] D. Klaassen, "A unified mobility model for device simulation—I. Model equations and concentration dependence," *Solid-State Electronics,* vol. 35, no. 7, pp. 953-959, 1992.
[76] D. Klaassen, "A unified mobility model for device simulation—II. Temperature dependence of carrier mobility and lifetime," *Solid-State Electronics,* vol. 35, no. 7, pp. 961-967, 1992.
[77] A. Cuevas, "Modelling silicon characterisation," *Energy Procedia,* vol. 8, pp. 94-99, 2011, doi: 10.1016/j.egypro.2011.06.108.
[78] M. Goodarzi, R. A. Sinton, and D. Macdonald, "Improving transient photoconductance lifetime measurements on ingots with deeper photogeneration," in *Silicon PV 2018, The 8th International Conference on Crystalline Silicon Photovoltaics*, Lausanne, Switzerland, Aug 10, 2018 2018, vol. 1999, no. 1: AIP Publishing, 2018, pp. 37-44, doi: 10.1063/1.5049247. [Online]. Available: https://aip.scitation.org/doi/abs/10.1063/1.5049247
[79] R. A. Sinton and T. Trupke, "Limitations on dynamic excess carrier lifetime calibration methods," *Progress in Photovoltaics: Research and Applications,* vol. 20, no. 2, pp. 246-249, 2012, doi: 10.1002/pip.1119.
[80] J. S. Swirhun, R. A. Sinton, M. K. Forsyth, and T. Mankad, "Contactless measurement of minority carrier lifetime in silicon ingots and bricks," *Progress in Photovoltaics: Research and Applications,* vol. 19, no. 3, pp. 313-319, 2011, doi: 10.1002/pip.1029.
[81] T. Trupke *et al.*, "Temperature dependence of the radiative recombination coefficient of intrinsic crystalline silicon," *Journal of Applied Physics,* vol. 94, no. 8, p. 4930, 2003, doi: 10.1063/1.1610231.
[82] G. Coletti, "Impurities in silicon and their impact on solar cell performance," Utrecht University, 2011.
[83] J. Schmidt, "Effect of dissociation of iron–boron pairs in crystalline silicon on solar cell properties," *Progress in Photovoltaics: Research and Applications,* vol. 13, no. 4, pp. 325-331, 2005, doi: doi:10.1002/pip.594.
[84] T. Bartel *et al.*, "Dynamics of iron-acceptor-pair formation in co-doped silicon," *Applied Physics Letters,* vol. 103, no. 20, p. 202109, 2013, doi: 10.1063/1.4830227.
[85] F. Gibaja, T. Bartel, M. Heuer, O. Graf, M. Kaes, and F. Kirscht, "Silicon Ingot Quality and Resulting Solar Cell Performance," *Energy Procedia*, vol. 38, pp. 551-560, 2013, doi: 10.1016/j.egypro.2013.07.316.
[86] J. A. Giesecke, R. A. Sinton, M. C. Schubert, S. Riepe, and W. Warta, "Determination of Bulk Lifetime and Surface Recombination Velocity of Silicon Ingots From Dynamic Photoluminescence," *IEEE Journal of Photovoltaics,* vol. 3, no. 4, pp. 1311-1318, 2013, doi: 10.1109/jphotov.2013.2264622.

[87] D. Macdonald, T. Roth, P. N. K. Deenapanray, T. Trupke, and R. A. Bardos, "Doping dependence of the carrier lifetime crossover point upon dissociation of iron-boron pairs in crystalline silicon," *Applied Physics Letters,* vol. 89, no. 14, p. 142107, 2006, doi: 10.1063/1.2358126.

[88] B. Mitchell, D. Macdonald, J. Schon, J. W. Weber, H. Wagner, and T. Trupke, "Imaging As-Grown Interstitial Iron Concentration on Boron-Doped Silicon Bricks via Spectral Photoluminescence," *IEEE Journal of Photovoltaics,* vol. 4, no. 5, pp. 1185-1196, 2014, doi: 10.1109/jphotov.2014.2326714.

[89] A. L. Blum *et al.*, "Interlaboratory Study of Eddy-Current Measurement of Excess-Carrier Recombination Lifetime," *IEEE Journal of Photovoltaics,* vol. 4, no. 1, pp. 525-531, 2014, doi: 10.1109/jphotov.2013.2284375.

[90] J. Tan, D. Macdonald, F. Rougieux, and A. Cuevas, "Accurate measurement of the formation rate of iron–boron pairs in silicon," *Semiconductor Science and Technology,* vol. 26, no. 5, p. 055019, 2011, doi: 10.1088/0268-1242/26/5/055019.

[91] D. Macdonald, J. Tan, and T. Trupke, "Imaging interstitial iron concentrations in boron-doped crystalline silicon using photoluminescence," *Journal of Applied Physics,* vol. 103, no. 7, p. 073710, 2008, doi: 10.1063/1.2903895.

[92] A. Liu, C. Sun, V. Markevich, A. Peaker, J. Murphy, and D. Macdonald, "Gettering of interstitial iron in silicon by plasma-enhanced chemical vapour deposited silicon nitride films," *Journal of Applied Physics,* vol. 120, no. 19, p. 193103, 2016.

[93] D. Chung, B. Mitchell, M. Goodarzi, R. A. Sinton, D. Macdonald, and T. Trupke, "Uncertainty in photoluminescence metrology on multicrystalline silicon bricks and cross validation with wafers," *IEEE Journal of Photovoltaics,* vol. 7, no. 6, pp. 1701-1709, 2017.

[94] G. Coletti *et al.*, "Impact of Metal Contamination in Silicon Solar Cells," *Advanced Functional Materials,* vol. 21, no. 5, pp. 879-890, 2011, doi: doi:10.1002/adfm.201000849.

[95] J. Schmidt and A. G. Aberle, "Accurate method for the determination of bulk minority-carrier lifetimes of mono- and multicrystalline silicon wafers," *Journal of Applied Physics,* vol. 81, no. 9, pp. 6186-6199, 1997, doi: 10.1063/1.364403.

[96] M. Goodarzi, R. Sinton, D. Chung, B. Mitchell, T. Trupke, and D. Macdonald, "A comparison between quasi-steady state and transient photoconductance lifetimes in silicon ingots: simulations and measurements," in *2017 IEEE 44th Photovoltaic Specialist Conference (PVSC)*, Washington, DC, 2017, pp. 2707-2710, doi: 10.1109/PVSC.2017.8366658. [Online]. Available: http://ieeexplore.ieee.org/stamp/stamp.jsp?tp=&arnumber=8366658&isnumber=8366001

[97] N. Schüler, T. Hahn, K. Dornich, J. R. Niklas, and B. Gründig-Wendrock, "Theoretical and experimental comparison of contactless lifetime measurement methods for thick silicon samples," *Solar Energy Materials and Solar Cells,* vol. 94, no. 6, pp. 1076-1080, 2010, doi: 10.1016/j.solmat.2010.02.028.

[98] B. Mitchell, J. W. Weber, D. Walter, D. Macdonald, and T. Trupke, "On the method of photoluminescence spectral intensity ratio imaging of silicon bricks: Advances and limitations," *Journal of Applied Physics,* vol. 112, no. 6, p. 063116, 2012.

[99] D. Chung, B. Mitchell, M. Goodarzi, C. Sun, D. Macdonald, and T. Trupke, "Bulk lifetimes up to 20 ms measured on unpassivated silicon discs using photoluminescence imaging," *IEEE Journal of Photovoltaics,* vol. 7, no. 2, pp. 444-449, 2017.

[100] J. A. Giesecke, M. C. Schubert, D. Walter, and W. Warta, "Minority carrier lifetime in silicon wafers from quasi-steady-state photoluminescence," *Applied Physics Letters*, vol. 97, no. 9, p. 092109, 2010, doi: 10.1063/1.3485216.
[101] D. Chung, B. Mitchell, M. K. Juhl, M. Abbott, and T. Trupke, "Lifetime Imaging on Silicon Bricks Using the Ratio of Photoluminescence Images With Different Excitation Wavelengths," *IEEE Journal of Photovoltaics*, pp. 1-9, 2018, doi: 10.1109/jphotov.2018.2831449.
[102] A. Cuevas and D. Macdonald, "Measuring and interpreting the lifetime of silicon wafers," *Solar Energy*, vol. 76, no. 1-3, pp. 255-262, 2004, doi: 10.1016/j.solener.2003.07.033.
[103] S. Johnston, F. Yan, K. Zaunbrecher, M. Al-Jassim, O. Sidelkheir, and K. Ounadjela, "Quality characterization of silicon bricks using photoluminescence imaging and photoconductive decay," in *2012 38th IEEE Photovoltaic Specialists Conference*, 2012: IEEE, pp. 000406-000410.
[104] M. Goodarzi, R. Sinton, and D. Macdonald, "Quasi-steady-state photoconductance bulk lifetime measurements on silicon ingots with deeper photogeneration," *AIP Advances*, vol. 9, no. 1, p. 015128, 2019, doi: 10.1063/1.5086378.